VILNIUS UNIVERSITY
CENTER FOR PHYSICAL SCIENCES AND TECHNOLOGY

Andrius Žemaitis

Efficient Laser Ablation for Bio-inspired 3D Functional Surfaces

DOCTORAL DISSERTATION

Technological Sciences,
Material Engineering (T 008)

VILNIUS 2022

This dissertation was prepared between 2017 and 2021 in Center for Physical Sciences and Technology. The research was supported by Research Council of Lithuania.

Academic supervisor – Dr. Mindaugas Gedvilas (Center for Physical Sciences and Technology, Technological Sciences, Materials Engineering – T 008).

This doctoral dissertation will be defended in a public meeting of the Dissertation Defence Panel:

Chairman – Prof. Dr. Mangirdas Malinauskas (Vilnius University, Technological Sciences, Materials Engineering – T 008).
Members:
Dr. Domas Paipulas (Vilnius University, Technological Sciences, Materials Engineering – T 008),
Prof. Habil. Dr. Valdas Sirutkaitis (Vilnius University, Technological Sciences, Materials Engineering – T 008),
Dr. Evangelos Skoulas (Foundation for Research and Technology – Hellas, Technological Sciences, Materials Engineering – T 008),
Prof. Dr. Tomas Tamulevičius (Kaunas University of Technology, Technological Sciences, Materials Engineering – T 008).

The dissertation shall be defended at a public meeting of the Dissertation Defence Panel at 11:00 on 1st of July 2022 in the hall of FTMC Institute of Physics.
Address: Savanoriu Ave. 231, 02300 Vilnius, Lithuania
Tel. +370 5 264 884; e-mail: office@ftmc.lt
The text of this dissertation can be accessed at the libraries of Center for Physical Sciences and Technology and Vilnius University, as well as on the website of Vilnius University: www.vu.lt/lt/naujienos/ivykiu-kalendorius

VILNIAUS UNIVERSITETAS
FIZINIŲ IR TECHNOLOGIJOS MOKSLŲ CENTRAS

Andrius Žemaitis

Naši lazerinė abliacija bioinspiruotų trimačių funkcinių paviršių kūrimui

DAKTARO DISERTACIJA

Technologijos mokslai,
Medžiagų inžinerija (T 008)

VILNIUS 2022

Disertacija rengta 2017– 2021 metais Fizinių ir technologijos mokslų centre. Mokslinius tyrimus rėmė Lietuvos mokslo taryba.

Disertacija ginama viešame Gynimo tarybos posėdyje 2022 m. liepos mėn. 1 d. 11 val. FTMC Fizikos instituto salėje. Adresas: Savanorių pr. 231, 02300 Vilnius, Lietuva tel. +370 5 264 884; el. paštas office@ftmc.lt.

Disertaciją galima peržiūrėti Fizinių ir technologijos mokslų centro bei Vilniaus universiteto bibliotekose ir VU interneto svetainėje adresu: https://www.vu.lt/naujienos/ivykiu-kalendorius

TABLE OF CONTENTS

ABBREVIATIONS

2D	two-dimensional
2.5D	two-and-a-half dimensional
3D	three-dimensional
AFM	atomic force microscope
CA	contact angle
CAD	computer-aided design
CC	Creative Commons
CCD	charge-coupled device
CNC	computer numerical control
CW	continuous wave
DLIP	direct laser interference patterning
DLW	direct laser writing
DOE	diffractive optical element
EDS	X-ray energy dispersive spectroscopy
FORTH	Foundation for Research and Technology
FTMC	Center for Physical Sciences and Technology
HAZ	heat-affected zone
HSFL	high spatial frequency LIPSS
IESL	Institute of Electronic Structure and Laser
PZT	lead zirconate titanate
LIPSS	laser-induced periodic surface structures
LSFL	low spatial frequency LIPSS
LTS	Department of Laser Technologies
PRR	pulse repetition rate
PTFE	polytetrafluoroethylene
RR	radiation remnants
SEM	scanning electron microscope
SLM	spatial light modulator
SP	surface plasmons
SPP	surface plasmon polaritons
STL	standard triangle language
TTM	two-temperature model
UV	ultraviolet
WoS	Web of Science
XPS	X-ray photoelectron spectroscopy

INTRODUCTION

Laser micro processing is a technology that uses laser irradiation to form a desired structural change on the surface or inside the volume. This technology allows the creation of small structures in the range of several micrometres. Laser micro processing is a non-contact process, which has many advantages like high accuracy, repeatability, flexibility. Many engineering materials can be processed by laser radiation, especially by ultrashort pulses. Ultrashort light pulses have opened up a new field of science that deals with the interaction of light and matter on extremely short time scales ($10^{-15} - 10^{-12}$ s). Due to the ability to focus the laser beam to micrometric spot size and a very short light pulse reaching femtoseconds (10^{-15} s), the light intensity can exceed even terawatts (10^{12} W) per square centimetre. At such a high light intensity, an irreversible modification of the material occurs – disassemble (removal of the material from the surface) or damage. When a material is removed directly by evaporation, laser ablation of the matter takes place. Laser ablation is a threshold process that begins when the energy density of a laser pulse (fluence) exceeds a certain threshold value, called the ablation threshold. When a matter is exposed to multiple laser pulses, where each pulse has fluence lower than the ablation threshold, an accumulation of impact to the matter occurs. In this regime of laser-matter interaction, the formation of self-organised structures like laser-induced periodic surface structures (LIPSS) also called ripples and nanoparticles occurs.

Due to short laser-matter interaction time and confined micrometric area, ultrashort laser pulses allow precision processing with melt-free surface and minimal heat affected zone. In the theory, laser processed surface quality mainly depends on pulse duration. However, even femtosecond (fs) laser pulses can produce rough, spiky, or covered with melt film surfaces. Basically, the processed surface quality depends on heat generated during laser processing. The origin of heat in the sample comes from laser energy losses. Not all absorbed laser energy is used for the ablation, therefore part of the energy remains in the matter as residual heat. Since the ablation process has certain threshold, only energy density higher than the ablation threshold will be used for material removal. For the high pulse repetition rates starting from hundreds of kHz, the residual heat may not be removed fast enough via heat conduction from the interaction area. Therefore, heat accumulates, the quality of the processed surface and the surrounding area suffers. On the other hand, the heat accumulation can be beneficial for ablation efficiency. In the multi-pulse laser processing regime, the laser pulse meets the material preheated by

the previous pulses, therefore the energy required to reach the boiling temperature of the matter is lower. As a consequence, the residual energy from the previous pulses is not completely lost resulting in an increase of the ablation efficiency. Ultrashort pulse packages, so-called bursts, attracted a high interest in the scientific community due to the ejection of residual heat with high pulse repetition rate pulses resulting in the increased ablation efficiency [1]. Every year average power of ultrashort pulse lasers increases, now reaching kW level [2]. Indeed, the laser technology follows Moor's law: the average power of these lasers doubles every three years [3]. High-power lasers challenge the field of laser material processing. In the perfect scenario, full laser power should be used for the industrial application to increase the throughput. High-powers are achieved with mJ pulse energies and MHz or GHz pulse repetition rates, which result in heat management problems. Therefore, smart utilisation of laser energy methods and fast beam scanning systems are needed.

In recent years, ultrashort pulse lasers became a popular tool for high quality micro-machining of various materials in scientific, technological and medical applications. The process efficiency together with the throughput is crucial parameters for industrial applications. For ultrafast laser technology to be competitive in the industry, the high precision and fine quality achievable by fs pulses must go together with high efficiency and throughput. Modern femtosecond lasers are still expensive starting at hundreds kEUR and economical aspects must be considered before installing such an expensive tool in the production line. In the applications based on laser ablation such as drilling, cutting or milling, the process efficiency could be defined by the ablation efficiency as the volume of the material removed per laser pulse energy (e.g. $\mu m^3/\mu J$) while throughput – by ablation rate – a volume of the material removed per unit of time (e.g. mm^3/min). Similarly, in the applications based on surface change (functionalisation) such as laser structuring, texturing, colouring, cleaning and similar, the crucial parameter is the areal fabrication rate (e.g. mm^2/s).

One of the emerging areas where laser processing is utilised is the fabrication of bio-inspired (or biomimetic) functional surfaces. Functional surfaces in nature evolved over millions of years to let species survive, therefore the artificial fabrication and mimicking of these surfaces is highly desired by humankind. In nature, functional surfaces can be found on various animals, bugs and plants. Usually, surfaces are made of micro/nanoscale complex patterns, which enable advantageous properties like water repellence, drag friction reduction, adhesion, antireflection, structural colouration, self-cleaning and antibacterial. Laser processing is a perfect tool

for the creation of functional surfaces since it can be utilised for both micrometre and nanometre scales. Laser surface structuring in the micrometres scale can be achieved by direct laser writing (DLW) technique via material ablation. DLW resolution is determined by focusing optics, wavelength of irradiation, laser beam size and generally is limited by the light diffraction limit. Laser structuring beyond the light diffraction limit, in the nanoscale, is realised via beforehand mentioned self-organised structures. For example, multiple scan ultrashort pulse laser processing of stainless steel results in various nano or micro topographies like cones, bumps, columnar, melt-like and chaotic structures [4,5]. Laser-induced nano- and microstructures can be utilised for the formation of functional surfaces with altered wetting [6], optical [7,8], tribological [9,10] properties.

This dissertation was dedicated to the exploration of ultrashort pulse laser ablation efficiency, rate, quality and utilisation for microfabrication. In the first part of this dissertation experiments and semi-empirical modelling for ablation efficiency is presented. Methods of optimisation were developed for the comparison of laser ablation results. By using the beam spot size optimisation method, the influence of MHz, GHz bursts on ablation was investigated. At the time of published results, the record of highest ablation efficiency for copper was achieved. For the first time, state-of-the-art femtosecond laser, working in the biburst (burst in the burst) mode was tested by a previously developed optimisation method. To demonstrate the laser technology capabilities, the optimised laser ablation process for the highest efficiency was utilised for the fabrication of both-sided three-dimensional (3D) parts, bio-inspired fish scales, drag reducing riblet surfaces on flat and cylindrical surfaces. Lastly, ultrafast laser surface structuring by ripples and nanospikes was used for the wettability control of stainless steel.

THE AIM OF THE THESIS

The goal of the thesis was to investigate ultrashort pulse laser ablation for efficient utilisation of energy in precise and rapid high-quality microfabrication.

THE SCIENTIFIC TASKS OF THE THESIS

1. To develop laser ablation optimisation methodology experimentally and theoretically.
2. To find out the optimal conditions of high-power MHz burst of ultrashort pulses for efficient ablation process.

3. To investigate and compare conventional, MHz-, GHz-, and bi- burst processing modes for laser ablation-based drilling and milling.
4. To fabricate bio-inspired functional surfaces by efficient laser milling.

SCIENTIFIC NOVELTY

In this dissertation, beam size optimisation method for rectangular cavity ablation was introduced. In addition, numerical model of laser ablation incorporating ablation threshold decrease and the saturation of ablation depth, if many pulses are applied to a single spot, was proposed. The model predicted the beam size and the pitch distance influence on ablation rate. Beam size optimisation method was applied to characterise and compare the MHz-, GHz- and bi- burst drilling and milling approaches. Record high ultrashort pulse ablation efficiencies were reported. For the first time, both-sided 3D objects were fabricated by layer-by-layer processing technique. Bio-inspired functional surface with full wettability control on stainless steel was created by a simple, single-step procedure via femtosecond laser structuring. To the best of our knowledge, there was no research work found in scientific literature exploring a single-step technique with the ability of tuning wetting state of stainless steel from highly hydrophilic to superhydrophobic.

PRACTICAL VALUE

The introduced beam size optimisation method for rectangular cavity is a reliable tool to evaluate the performance of the industrial laser and compare with others. From an engineering point of view, presented ablation model is essential theoretical tool to find the most efficient ablation point. In-depth study and gathered numerous data of laser MHz-, GHz-, bi- burst-matter interaction helps in the theoretical modelling and understanding of ablation by bursts. Laser fabrication of functional surfaces (drag reducing and superhydrophobic) is directly pointed towards the applications, where energy savings and self-cleaning properties are desired.

STATEMENTS TO DEFEND

1. Ultrashort pulse laser ablation efficiency of rectangular cavity is influenced by the beam transverse and vertical inter-pulse distance (pitch and hatch). The optimal conditions (beam radius and inter-pulse distance) for maximal efficiency can be predicted by the numerical model, which

incorporates the ablation threshold and penetration depth decrease due to multiple laser pulses per spot.

2. Ablation efficiency of copper milling by ultrashort pulses of 10 ps pulse duration and 120 µJ pulse energy can be increased by 50% using the beam size optimization technique. Furthermore, 20% increase may be achieved if 3-pulse burst with 64.5 MHz intra-burst pulse repetition rate is applied instead of single-pulse processing.

3. Beam-size-optimised laser drilling of copper by 4.88 GHz bursts with pulses per burst up to $P = 25$ and pulse duration of 210 fs does not improve the ablation efficiency compared to the conventional single-pulse drilling. Nevertheless, the utilisation of 64.7 MHz- and bi-(4.88 GHz with 64.7 MHz) bursts in drilling increases the efficiency up to 14%.

4. Ultrashort pulse laser irradiation (210 fs – 10 ps) is a versatile tool for rapid high-quality fabrication of functional surfaces by milling and texturing. Laser milled riblet structures reduce air drag friction up to 6% and wetting state of laser textured stainless steel surface can be controlled from highly hydrophilic to superhydrophobic.

APPROBATION

Results of the research, presented in the thesis, were published in 7 scientific papers [A1-A7] and 2 conference proceedings [A8, A9] and together with co-authors the results were presented at 25 international conferences and schools [C1-C25], where 3 awards were won for the best presentations [C2, C15, C18]. In total, my publication list includes 13 scientific papers [A1-A13].

Scientific papers directly related to the thesis (peer-reviewed and indexed in Clarivate Web of Science (WoS)):

A1. **A. Žemaitis**, M. Gaidys, P. Gečys, M. Barkauskas, M. Gedvilas, "Femtosecond laser ablation by bibursts in the MHz and GHz pulse repetition rates," Opt. Express **29**, 7641–7653 (2021).

A2. **A. Žemaitis**, A. Mimidis, A. Papadopoulos, P. Gečys, G. Račiukaitis, E. Stratakis, M. Gedvilas, "Controlling the wettability of stainless steel from highly-hydrophilic to super-hydrophobic by femtosecond laser-induced ripples and nanospikes," RSC Adv. **10**, 37956-37961 (2020).

A3. **A. Žemaitis**, P. Gečys, M. Barkauskas, G. Račiukaitis, M. Gedvilas, "Highly-efficient laser ablation of copper by bursts of ultrashort tuneable (fs-ps) pulses,", Sci. Rep. **9**, 12280 (2019).

A4. M. Gaidys, **A. Žemaitis**, P. Gečys, M. Gedvilas, "Efficient picosecond laser ablation of copper cylinders," Appl. Sur. Sci. **483**, 962-966 (2019).

A5. **A. Žemaitis**, M. Gaidys, P. Gečys, G. Račiukaitis, M. Gedvilas, "Rapid high-quality 3D micro-machining by optimised efficient ultrashort laser ablation," Opt. Lasers Eng. **114**, 83-89 (2019).

A6. **A. Žemaitis**, J. Mikšys, M. Gaidys, P. Gečys, M. Gedvilas, "High-efficiency laser fabrication of drag reducing riblet surfaces on pre-heated Teflon," Mater. Res. Express **6**, 065309 (2019).

A7. **A. Žemaitis**, M. Gaidys, M. Brikas, P. Gečys, G. Račiukaitis, M. Gedvilas, "Advanced laser scanning for highly-efficient ablation and ultrafast surface structuring: experiment and model," Sci. Rep. **8**, 17376 (2018).

Scientific papers directly related to the thesis (conference proceedings):

A8. **A. Žemaitis**, P. Gečys, G. Račiukaitis, and M. Gedvilas, "Efficient ablation by ultra-short pulse lasers," Procedia CIRP **94**, 962–965 (2020).

A9. **A. Žemaitis**, M. Gaidys, J. Mikšys, P. Gečys, M. Gedvilas, "Functional surface formation by efficient laser ablation using single-pulse and burst-modes," Proc. SPIE **11673**, 116730S (2021).

Other scientific papers (peer-reviewed and indexed in Clarivate WoS):

A10. **A. Žemaitis**, M. Gaidys, P. Gečys, M. Gedvilas, "Influence of nonlinear and saturable absorption on laser lift-off threshold of an oxide/metal structure," Opt. Lett. **45**, 6166 – 6169 (2020).

A11. P. Gečys, E. Markauskas, **A. Žemaitis**, G. Račiukaitis, "Variation of P2 series interconnects electrical conductivity in the CIGS solar cells by picosecond laser induced modification," Sol. Energy **132**, 493–502 (2016).

A12. P. Gečys, E. Markauskas, **A. Žemaitis**, G. Račiukaitis, "Picosecond Laser Modification of CIGS Active Layer," J. Laser Micro Nanoen. **11**(2), 257–260 (2016).

A13. E. Markauskas, P. Gečys, **A. Žemaitis**, G. Račiukaitis, "Validation of monolithic interconnection conductivity in laser scribed CIGS thin-film solar cells," Sol. Energy **120**, 35-43 (2015).

Conferences directly related to the thesis (presenter underlined)

C1. <u>**A. Žemaitis,**</u> P. Gečys, M. Gedvilas, "Fabrication of steel moulds with functional surfaces based on efficient laser ablation, surface structuring, and GHz burst polishing," 4th International Conference on Optics, Photonics and Lasers (OPAL' 2021), Corfu, Greece (2021). Poster.

C2. <u>**A. Žemaitis**</u>, G. Merkininkaitė, S. Steponavičiūtė, P. Gečys, A. Mimidis, A. Papadopoulos, E. Stratakis, M. Gedvilas, "Ultrafast laser surface structuring for wettability control of stainless steel", 23rd International Conference – School Advanced Materials and Technologies 2021, Palanga, Lithuania (2021). Poster. **Young Scientist Award – in recognition of the best poster presented.**

C3. <u>**A. Žemaitis**</u>, M. Gaidys, P. Gečys, G. Račiukaitis, M. Gedvilas, "Ultrafast laser ablation by bi-bursts in MHz and GHz pulse repetition rate", Photonics West, Laser Applications in Microelectronic and Optoelectronic Manufacturing (LAMOM) XXVI, San Francisco, California, USA (2021). Virtual, oral.

C4. **A. Žemaitis**, M. Gaidys, J. Mikšys, P. Gečys, <u>M. Gedvilas,</u> "Functional surface formation by efficient laser ablation using single-pulse and burst-modes," Photonics West, Laser Applications in Microelectronic and Optoelectronic Manufacturing (LAMOM) XXVI, San Francisco, California, USA (2021). Virtual, oral.

C5. <u>M. Gaidys</u>, **A. Žemaitis**, P. Gečys, M. Gedvilas, "High-throughput laser ablation and polishing of copper cylinders," The 22nd International Symposium on Laser Precision Microfabrication (LPM 2021), Hirosaki, Aomori, Japan (2021). Virtual, oral.

C6. <u>M. Gaidys</u>, **A. Žemaitis**, P. Gečys, M. Gedvilas, "Influence of laser pulse repetition rate on the ablation efficiency and surface quality of copper," 17th International Conference of Young Scientists on Energy and Natural Sciences Issues (CYSENI 2021), Kaunas, Lithuania (2021). Virtual, oral.

C7. <u>M. Gaidys</u>, **A. Žemaitis**, P. Gečys, M. Gedvilas, "Efficient drilling, milling, and polishing on metals using ultrashort bursts and bibursts," The 2021 International High Power Laser Ablation Symposium (HPLA 2021), Santa Fe, New Mexico, USA (2021). Virtual, oral.

C8. U. Gudauskytė, **A. Žemaitis**, P. Gečys, M. Gedvilas, "Ultrashort laser ablation of metals: efficiency and quality," 10th International Summer School "Trends and new developments in Laser Technology", The Technische Universität Dresden and the Fraunhofer Institute for Material and Beam Technology (IWS), Dresden, Germany (2021). Virtual, oral.

C9. S. Steponavičiūtė, **A. Žemaitis**, G. Merkininkaitė, A. Selskis, P. Gečys, M. Gedvilas, "High rate fabrication of superhydrophobic stainless steel surface by ultrashort laser pulses," 10th International Summer School "Trends and new developments in Laser Technology", The Technische Universität Dresden and the Fraunhofer Institute for Material and Beam Technology (IWS), Dresden, Germany (2021). Virtual, oral.

C10. **A. Žemaitis**, M. Gaidys, P. Gečys, M. Gedvilas, "Novel biburst ultrafast laser ablation: burst-in-burst regime," The 21th International Symposium on Laser Precision Microfabrication (LPM 2020), Dresden, Germany (2020). Virtual, oral.

C11. **A. Žemaitis**, P. Gečys, G. Račiukaitis, M. Gedvilas, "High-efficiency laser milling by bursts of ultrashort (fs-ps) light pulses," Photonics West, Laser Applications in Microelectronic and Optoelectronic Manufacturing (LAMOM) XXV, San Francisco, California, USA (2020). Oral.

C12. **A. Žemaitis**, M. Gaidys, P. Gečys, M. Gedvilas, "Efficient laser milling technology for bio-inspired functional surface formation," 22nd International Conference – School Advanced Materials and Technologies 2020, Palanga, Lithuania (2020). Poster.

C13. **A. Žemaitis**, P. Gečys, M. Gedvilas, "Highly-efficient ultrashort pulse laser ablation by bursts of pulses," 15th International Conference on Laser Ablation (COLA 2019), Maui-Hawaii, USA (2019). Oral.

C14. **A. Žemaitis**, P. Gečys, G. Račiukaitis, M. Gedvilas, "Rapid 3D micro-machining by optimised bursts of ultrashort laser pulses – beyond the ablation-cooling," The 8th International Congress on Laser Advanced Materials Processing (LAMP 2019), The 20th International Symposium on Laser Precision Microfabrication (LPM 2019), Hiroshima, Japan (2019). Oral.

C15. **A. Žemaitis**, P. Gečys, M. Gedvilas, "Fabrication of 3D objects using efficient laser ablation", XXTH International Conference and School on Quantum Electronics Laser Physics and Applications (ICSQE 2018), Nessebar, Bulgaria (2018). Oral. **SPIE award: Certificate of Excellence for Second Place Student Presentation**).

C16. **A. Žemaitis**, P. Gečys, G. Račiukaitis, M. Gedvilas, "Efficient ultrafast laser ablation for 3D structuring and engraving," The 19th International Symposium on Laser Precision Microfabrication (LPM 2018), Edinburgh, UK (2018). Oral.

C17. **A. Žemaitis**, M. Gaidys, M. Gedvilas, "Efficient ultrashort pulsed laser ablation for 3D engraving," 61th International Conference for Students of Physics and Natural Sciences „Open Readings 2018", Vilnius, Lithuania (2018). Oral.

C18. **A. Žemaitis**, P. Gečys, G. Račiukaitis, M. Gedvilas, "Rapid and high-quality 3D fabrication by efficient ultrashort laser ablation," 11th International Conference on Photo-Excited Processes and Applications (ICPEPA 11), Vilnius, Lithuania (2018). Poster. **Outstanding Student Poster Award, III-rd place**.

C19. M. Gedvilas, **A. Žemaitis**, M. Gaidys, P. Gečys, G. Račiukaitis, "Efficient laser scanning ablation procedure for ultrafast surface structuring," 11th International Conference on Photo-Excited Processes and Applications (ICPEPA 11), Vilnius, Lithuania (2018). Oral.

C20. A. Skirsgilas, **A. Žemaitis**, P. Gečys, "Fabrication of scanned three-dimensional object by efficient laser ablation," 11th International Conference on Photo-Excited Processes and Applications (ICPEPA 11), Vilnius, Lithuania (2018). Poster.

C21. M. Gaidys, **A. Žemaitis**, P. Gečys, G. Račiukaitis, M. Gedvilas, "Efficient picosecond laser ablation on cylindrical surfaces," 11th International Conference on Photo-Excited Processes and Applications (ICPEPA 11), Vilnius, Lithuania (2018). Poster.

C22. M. Gaidys, **A. Žemaitis**, P. Gečys, M. Gedvilas, "Study of efficient copper laser ablation," 61th International Conference for Students of Physics and Natural Sciences "Open Readings 2018", Vilnius, Lithuania (2018). Poster.

C23. **A. Žemaitis**, P. Gečys, G. Račiukaitis, M. Gedvilas, "Efficient ultrafast laser ablation for 3D engraving," 6th International School on Lasers in Materials Science (SLIMS), S. Servolo Island, Venice, Italy (2018). Oral and poster.

C24. M. Gaidys, **A. Žemaitis**, P. Gečys, G. Račiukaitis, M. Gedvilas, "Efficient laser ablation on flat and cylindrical surfaces," 6th International School on Lasers in Materials Science (SLIMS), S. Servolo Island, Venice, Italy, (2018). Oral and poster.

C25. M. Gedvilas, **A. Žemaitis**, P. Gečys, G. Račiukaitis, Sub-ns Laser Effective Ablation of Metals, The 18th International Symposium on Laser Precision Microfabrication (LPM 2017), Toyama, Japan (2017). Oral.

AUTHOR'S CONTRIBUTION

All the research presented in this thesis was performed by the author except the work listed in co-author's contribution section. Author contributed to experimental design, execution of experiments, characterisation, measurements, data analysis, numerical simulation, and manuscript preparation of [A1-A3, A5, A8] scientific papers.

CO-AUTHOR'S CONTRIBUTION

Dr. Mindaugas Gedvilas – supervisor of the work, who led and consulted on PhD studies. Created the numerical model of laser ablation and wrote the [A7] manuscript. Analysed the data of drag-reducing experiments and wrote the [A6, A9] manuscripts.

Dr. Paulius Gečys – consulted on laser systems, measurements and experimental results.

Dr. Gediminas Račiukaitis – consulted on some of the experimental results.

Mantas Gaidys – under the author's supervision performed the experiments on cylindrical sample texturing and wrote the [A4] manuscript. Performed some of the stylus profiler and 3D optical profiler measurements for biburst experiments.

Dr. Martynas Barkauskas – supported with state-of-the-art lasers.

Justinas Mikšys – performed some of the laser texturing experiments on Teflon.

Dr. Emmanuel Stratakis – consulted on laser texturing experiments for wettability control.

Antonis Papadopoulas – consulted on laser system and experimental results of laser texturing experiments for wettability control.

Alexandros Mimidis – performed some of the contact angle measurements.

Greta Merkininkaitė – performed some of the contact angle measurements and consulted on surface chemistry of laser irradiated stainless steel.

Dr. Lina Grinevičiūtė – performed AFM measurements.

Saulė Steponavičiūtė – prepared some of the illustrations.

1. LITERATURE OVERVIEW

1.1 Ablation by ultrashort laser pulses

Laser ablation is a material removal from a surface under direct absorption of laser radiation [11]. The light absorption can be linear or non-linear, depending on the intensity applied to the material. The physics of the laser ablation process combines the interaction of laser radiation with matter, the formation and growth of vapor and plasma, and the interaction of laser radiation with vapor and plasma [12].

When material is under laser irradiation, part of the radiation can be scattered, reflected, absorbed or transmitted. According to Beer-Lambert law, the light intensity in the material will drop exponentially with the depth z, described by the absorption coefficient of the material α:

$$I(z) = (1 - R)I_0 e^{-\alpha z}, \tag{1}$$

where $I(z)$ is the light intensity in the depth z, I_0 is the initial light intensity, R is the reflection coefficient [12]. Absorption coefficient α is related to attenuation coefficient κ_0 and light wavelength λ:

$$\alpha = \frac{4\pi n \kappa_0}{\lambda}, \tag{2}$$

where n is the refractive index of the material. Instead of α sometimes optical penetration depth $l_\alpha = \alpha^{-1}$ is used [12].

The mechanisms of interaction between laser radiation and matter depend on the parameters of the radiation, physical, and chemical properties of the material. In metals, almost all of the incident light is absorbed by the electrons of the conduction band in the skin layer, which is typically 10 nm thick. The typical duration of the electron-electron collision for metals is from 10 fs to 1 ps. Hot electrons transfer energy to the material by the interactions with ions in lattice. Due to the large difference between the masses of the electron and the ion, the electron-phonon relaxation time is significantly longer. Depending on the electron-phonon coupling, relaxation takes from 1 ps to 10 ns [11]. Temperature difference and variation between the two subsystems (electrons and lattice) is described by the two-temperature model (TTM) [13]. In TTM evolution of electronic and lattice temperatures, T_e and T_l, is described by two coupled heat equations:

$$C_e \frac{\partial T_e}{\partial t} = \nabla \cdot \{\kappa_e \nabla T_e\} - \Gamma\{T_e - T_l\} + Q(\mathbf{r}, t), \tag{3}$$

$$C_l \frac{\partial T_l}{\partial t} = \nabla \cdot \{\kappa_l \nabla T_l\} + \Gamma\{T_e - T_l\}, \tag{4}$$

where C_e and C_l are the specific heat capacities, and κ_e and κ_l are the heat conductivities of the electron and lattice subsystems, respectively. The first terms on the right-hand sides of both equations' accounts for the heat diffusion in the two subsystems. The second term $\Gamma\{T_e - T_l\}$ is the rate of the heat transferred from hot electrons to the cooler lattice. Γ is the electron-lattice coupling term. $Q(\mathbf{r}, t)$ is the laser source term, t is time, and $\mathbf{r}$ coordinate vector [14].

In the short pulse regime (nanosecond or longer), electrons and lattice have sufficient time reach thermal equilibrium ($T_e = T_l = T$) during a single pulse excitation. Therefore, TTM equations are reduced to a traditional heat diffusion equation:

$$\rho c_p \frac{\partial T}{\partial t} - \kappa \nabla^2 T = Q(\mathbf{r}, t), \tag{5}$$

where ρ is the mass density and c_p is the specific heat at a constant pressure. Therefore, thermal ablation models are used to describe ablation by nanosecond (and longer) pulse ablation. In these models, material irradiated by laser pulse undergoes heating, melting, boiling and evaporation. In this case, thermal processes make the largest influence, especially in metals with high specific thermal conductivity [15]. The resolution of nanosecond (ns) laser pulse processing is limited by the heat diffusion length l_T:

$$l_T \approx 2\sqrt{D_T \tau_l}, \tag{6}$$

where $D_T = \kappa(\rho c_p)^{-1}$ is the heat diffusivity, τ_l is the laser pulse duration [11]. For a material with a high heat diffusivity like metals, the precision microfabrication must be performed by ultrashort pulses. The nanosecond pulse processing relates to the heat-affected zone (HAZ) that is present around the ablated crater (Fig. 1). In the HAZ zone, the temperature rises to the melting point but does not reach the boiling point. This is valid only till laser pulse duration is longer than electron-phonon relaxation time, $\tau_l \gg \tau_{e\text{-ph}}$. Of course, HAZ depends not only on material properties and pulse duration. Laser fluence, pulse repetition rate and for thin-films – layer thickness plays a crucial role too. On the other hand, if laser pulse duration is shorter than electron-phonon relaxation time, $\tau_l \ll \tau_{e\text{-ph}}$, the HAZ is no more related to the pulse duration, but depends on material properties and related relaxation times. In the simplest approximation HAZ can be estimated by $l_e \approx 2(D_e \tau_{e\text{-ph}})^{1/2}$, where $D_e = \kappa_e / C_e$ is the electron diffusivity, C_e is the

17

electronic heat capacity. Therefore, laser pulses with pulse duration τ_l shorter than electron-phonon relaxation time $\tau_{e\text{-}ph}$ is called ultrashort. Typically, laser pulses equal or shorter than 10 ps are named ultrashort [11]. This coincides well with $\tau_{e\text{-}ph}$ of metals, which is in the range of ps, e.g. for copper $\tau_{e\text{-}ph} = 10$ ps [16].
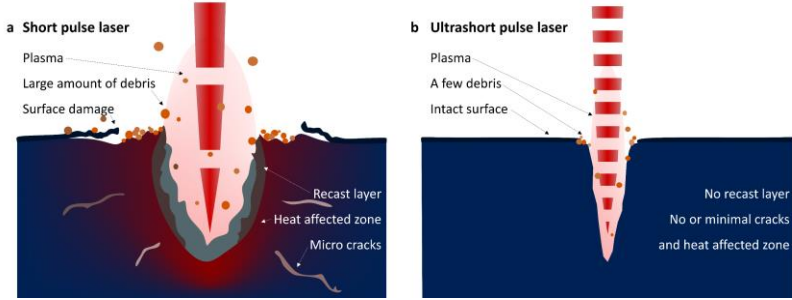
Fig. 1 Schematic representation of laser-matter interaction and related phenomena during irradiation by (a) short laser pulses and (b) ultrashort laser pulses. Adapted by permission from Springer Nature Customer Service Centre GmbH [17], Copyright © 2020, Springer Nature Switzerland AG.

By solving TTM model with accounted electron heat diffusion driven by temperature gradient, it was shown that electron-phonon relaxation time depends on pulse duration and laser fluence [18]. For the same laser fluence, the peak pulse intensity is higher for the shorter pulses, meaning matter absorbing much more energy per unit time. Therefore, the electron temperature will be higher and corresponding kinetic energy higher as well. It follows, that the electron-phonon collision frequency will be higher too, meaning faster electron-phonon thermalisation and shorter $\tau_{e\text{-}ph}$. Similarly, for higher laser fluence, the electrons get higher temperature and kinetic energy, meaning shorter $\tau_{e\text{-}ph}$. It should be noted that higher fluence does not mean reduced HAZ as could be understood from previous assumptions of shorter $\tau_{e\text{-}ph}$. Quite contrary, the higher the fluence the bigger the HAZ. The reason is that electron heat conductivity κ_e, electron-ion coupling factor Γ and electronic heat capacity C_e highly depend on electronic temperature, which increases for higher fluences.

The physics of femtosecond pulse ablation is very different compared to nanosecond pulses. To understand the process, it is necessary to include not only the processing conditions, but also the properties of the material, such as absorption, thermal conductivity, and plasma formation. These properties are in most cases not given by their equilibrium values or cannot be described by equations at local thermal equilibrium. Temperature-dependent parameters such as absorption or electron thermal conductivity cause strong nonlinear

processes that also complicate the description of the interaction. An interesting phenomenon is observed for radiation intensities up to $I = 10^{14}$ Wcm^{-2}. In a very small volume, calculated as the product of the spot size and skin depth, electrons can reach tens of thousands of Kelvins during the pulse and the lattice remains thermally undisturbed. At the end of the laser pulse and during the electron thermalization, the phonon temperature can rise close to or even above the critical temperature at which the phonon emission begins. The metal is then in an unstable nonequilibrium state leading to the ejection of the material due to high critical pressure. Therefore, large portion of the absorbed laser energy can be removed with the material during the ablation process. This is the nature of one of the biggest advantages of femtosecond laser applications over nanosecond lasers, as energy dissipation due to thermal conduction has little effect [19].

Two main mechanisms responsible for material ejection due to ultrashort pulse excitation are spallation and phase explosion (explosive boiling). The high intensity laser pulses lead to high heating rates. The heating is almost isochoric (material volume is constant), faster than thermal expansion of the lattice. Laser pulse length and electron-phonon relaxation time is shorter than the time required for mechanical relaxation (expansion) of the interaction volume, which leads to stress confinement. Within the interaction volume high thermoelastic pressures builds. Stress relaxation results in void formation [11]. Growth and percolation of these subsurface voids leads to the separation and ejection of the top layer from the surface – thermomechanical ablation (spallation) [20].

By using atomistic simulation of femtosecond laser interaction with aluminium target, it was shown that transition from spallation to the phase explosion regime, happens when laser fluence is increased several times (Fig. 2) [21]. The phase explosion regime asserts under conditions when the normal boiling is kinetically limited – the molten material can be heated far beyond its boiling point. In the volume of strongly superheated liquid, homogenous nucleation occurs at a high rate, leading to a rapid phase transition to a vapor phase, which is similar to explosion and is called explosive boiling in the field of thermodynamics [22]. This explosion leads to the ejection of the material in the mixture of vapor-phase atoms and clusters/droplets of different sizes [21], which in the laser-matter field is called phase explosion [23–25].
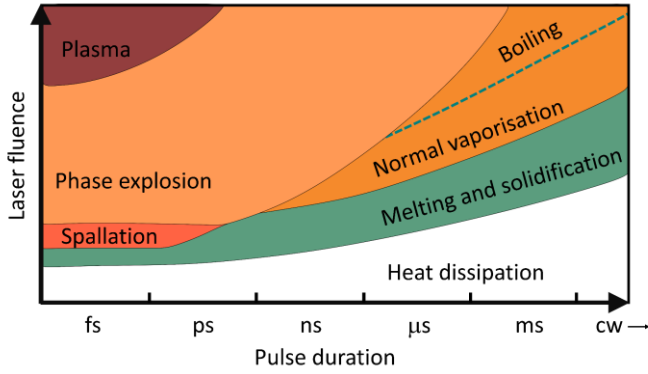
Fig. 2 Schematic diagram of thermal processes initiated by laser irradiation with certain fluence and pulse duration. Adapted by permission from Springer Nature Customer Service Centre GmbH [22], Copyright © 2020, Springer Nature Switzerland AG.

1.2 Efficient laser ablation

When laser fluence (laser energy density) exceeds particular fluence value the ablation of the material starts. This particular fluence is called the ablation threshold F_{th}. To measure the ablation threshold two main methods are used. First one, so called D-squared (D^2), originates from beam spot size measurement procedure, first proposed by Liu [26]. Craters are ablated by laser pulses with different pulse energies E_p. For the pulsed beam with Gaussian spatial distribution, laser fluence $F(r)$ is:

$$F(r) = F_0 e^{-2r^2/w_0^2},\tag{7}$$

where F_0 is the peak fluence in the centre of the beam, r is the distance from the centre of the beam:

$$F_0 = \frac{2E_p}{\pi w_0^2},\tag{8}$$

where w_0 – is the beam radius in the waist, the diameters of craters D scales with laser peak fluence F_0 as:

$$D^2 = 2w_0^2 \ln\left(\frac{F_0}{F_{th}(N)}\right).\tag{9}$$

where N is the number of laser pulses per irradiation spot. When experimental data is plotted (D^2 versus $\ln E_p$) the beam radius w_0 is extracted from the slope of the linear fit, also threshold energy E_{th} is equal to the value where linear fit crosses the abscise axis. Threshold fluence can be calculated by using (8) formula. This method is mostly suited for the ablation by ultrashort pulses and

20

for low pulse energies, since radial heat flow can compromise the assumptions behind the scaling law [14]. However, due to the incubation phenomena different ablation thresholds are observed for various laser pulses irradiated. The incubation model describes the relation between the single-pulse ablation threshold $F_{th}(1)$ and the multi-pulse ablation threshold $F_{th}(N)$ in the form [27]:

$$F_{th}(N) = F_{th}(1) \cdot N^{S-1}, \tag{10}$$

where S is a material-dependent incubation parameter. In real life homogenous material is rarely processed by laser, various defects, like inclusions and voids, might alter the ablation threshold. Defects initiate the ablation due to higher absorptance and lower threshold. Extended defect model predicts F_{th} increase for a smaller beam radius due to a lower possibility for the laser pulse to hit a defect within a smaller radius [28,29]:

$$F_{th}(w) = F_d + (F_i - F_a)\left(\frac{F_i}{F_d}\right)^{-\frac{1}{2}w^2\pi\sigma}, \tag{11}$$

where F_d and F_i – low density defect mediated and intrinsic threshold fluencies, respectively and σ – real density of the optically active defects. Also, this model assumes that after a certain beam width w, the ablation threshold F_{th} is constant.

The second method to determine the ablation threshold is crater depth versus fluence measurement procedure. Due to exponential decay of laser energy in the material and with some assumptions in two-temperature model it is shown that for femtosecond pulse ablation the ablated depth Δh scales with fluence F_0 as [11]:

$$\Delta h = \frac{1}{\alpha}\ln\left(\frac{F_0}{F_{th}}\right). \tag{12}$$

The ablation threshold is the intercept of $\Delta h(F_0)$. For Eq. (12) to be valid the approximation has to be made that final energy distribution is deposited in depth solely according to the optical penetration depth $l_\alpha = \alpha^{-1}$. It is rough assumption since electron diffusion length l_e, which depend on the electron temperature [16], plays an important role in the ultrashort pulse excitation, and could exceed optical penetration depth l_α several times. Nevertheless, the logarithmic scaling law was extensively used to describe the laser fluence dependence on ablated depth for various length laser pulses and different kind of materials [30–32]. It corresponds to experimental findings well despite the mismatch of fit parameter δ value to the optical penetration depth l_α (calculated from absorption coefficient). Therefore, fit parameter δ is simply

called the effective energy penetration depth, despite the mechanism behind the interaction.

If we consider Gaussian laser beam with spatial energy distribution in (7), the Eq. (12) can be rewritten in the form of:

$$\Delta h(r) = \delta \ln\left(\frac{F(r)}{F_{\text{th}}}\right). \tag{13}$$

It can be seen form (13) that depth of the ablated dimple depends on the radial distance r from the centre and has form of a paraboloid [33,34]. To calculate the volume V of the parabolic dimple ablated by laser pulse, we need to integrate the crater profile:

$$V = \frac{\pi \delta w_0^2}{4} \ln^2\left(\frac{F_0}{F_{\text{th}}}\right). \tag{14}$$

To calculate the ablation efficiency η_E (volume of the material removed per unit energy, for example $\mu m^3/\mu J$), the volume V has to be divided by pulse energy E_p to obtain:

$$\eta_E = \frac{\delta}{2F_0} \ln^2\left(\frac{F_0}{F_{\text{th}}}\right), \tag{15}$$

where (8) was used to simplify the equation. This equation has been widely used to fit the experimental data obtained by various cases of laser-matter interaction not only in ablation of dimple by single pulse but also ablation of cavities with multiple pulses and multiple scans [35–40]. This is simple model, which does not take into account many aspects occurring in ultrashort laser-matter interaction as heat accumulation [41], plasma/particle shielding [42], ablation threshold dynamics due to incubation [43] and similar. Nevertheless, it is a convenient base to explain the laser ablation efficiency originating from ablation geometric shape.

Similarly, to calculate ablation rate R_t (the volume of the material removed per time, for example mm^3/min) with multiple pulses, Eq. (14) has to be multiplied by laser pulse repetition rate f:

$$R_t = \frac{P\delta}{2F_0} \ln^2\left(\frac{F_0}{F_{\text{th}}}\right), \tag{16}$$

where $P = E_p f$ is the average optical power. It is worth to mention that term "ablation rate" in literature is often used to describe the depth ablated per laser pulse. In this dissertation ablation rate will be used to describe volume removal per time. To understand the influence of laser peak fluence on ablation, let's make simple graphs to explore equations (13)-(16).

Firstly, let's see how the ablated depth in the middle of the dimple and volume depends on laser fluence, when fluence F_0 is varied by pulse energy E_p (Fig. 3 a). Both, depth Δh and volume V nonlinearly increase with higher fluence. The logical conclusion to obtain a higher removed volume of the material would be to increase the pulse energy to the maximum available from the laser source. Indeed, the ablation rate R_t would be highest as can be seen in Fig. 3 b. Completely different scenario happens for the ablation efficiency, which has the maximum at certain fluence F_0, so called optimum fluence F_{opt}. Therefore, to have the highest efficiency η_E we are forced to reduce the pulse energy, also sacrifice the ablation rate.
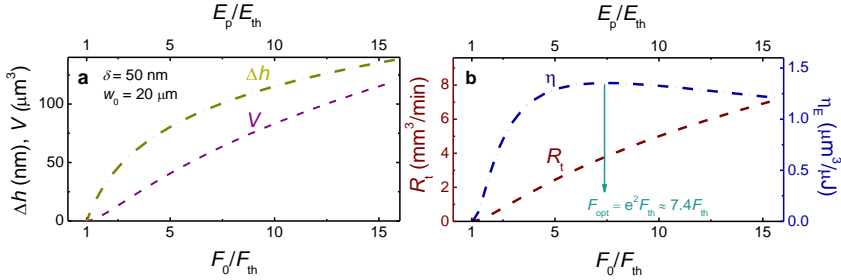

Fig. 3 Numerical representation of (13)-(16) equations, when effective penetration depth $\delta = 50$ nm and laser beam radius $w_0 = 20$ µm. (a) The depth Δh and the volume V of the crater and (b) ablation efficiency η_E and rate R_t dependence on laser peak fluence F_0 normalised to threshold fluence F_{th} when pulse energy is increased.

From (15) the ablation efficiency η_E reach maximum at $F_{opt} = e^2 F_{th} \approx 7.4 F_{th}$ (Fig. 3 b) [34]. It should be noted that straightforward calculation of ablation efficiency from ablation threshold F_{th} measurement (D-squared or depth methods) cannot be applied for multiple shot or multiple scan ablation procedure as milling due to complexity of laser-matter-plume interaction including heat accumulation [44] and plasma/particle shielding [42]. Also, threshold fluence itself depend on various laser processing parameters as laser wavelength (absorption) [45], pulse duration (interaction mechanism) [46], number of pulses applied per spot (incubation) [47,48], beam spot size (probability to hit a defect) [28,29].

If one would like to use maximum average optical power ($P = E_p f$), but also preserve maximum ablation efficiency, there are several strategies which could be used: laser beam splitting (to divide pulse energy E_p and also fluence F_0), laser beam size enlargement (to reduce laser fluence F_0) and if laser provide similar average power for various repetition rates, increase pulse repetition rate (to reduce pulse energy E_p and also fluence F_0) (Fig. 4). All these methods have their own advantages and drawbacks. The beam splitting strategy relies on optical elements, which must be introduced in the setup to

split the laser beam. The spatial light modulator (SLM) was utilised to divide a laser beam into 7 beam pattern, which was used for efficient lead zirconate titanate (PZT) ceramic cutting by translating the sample [49]. Also, the material processing could be realised with parallel beams produced by diffractive optical elements (DOE) or SLM coupled to galvanometer scanner [50–52]. The parallel beam processing is limited to the symmetrical patterns which can be created.
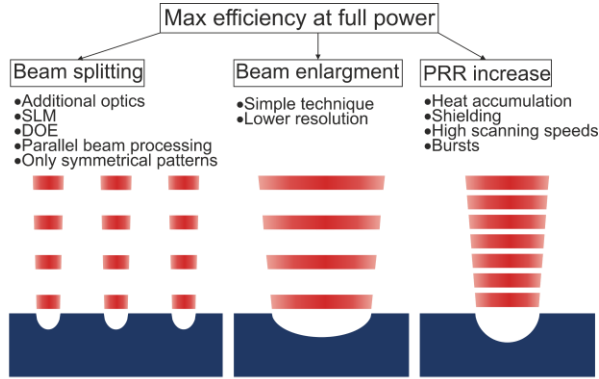

Fig. 4 Three methods to achieve maximum ablation efficiency while using full optical average power of laser source. PRR – pulse repetition rate.

To explore the laser beam enlargement strategy, let's investigate graphs similar to the ones in Fig. 3 a and b, but now instead of pulse energy E_p lets vary the beam radius w_0 to control the laser fluence F_0. The depth Δh of the crater increases the same as in the case of pulse energy variation, but the volume V behaves differently and has optimum fluence point (Fig. 5 a). Let's consider two limiting cases: at the very tight beam focusing the ablated crater would have a small width and therefore a small volume, on the other side – too loosely focused laser beam would not reach the fluence required for the ablation, and volume of the crater would be zero. These simple assumptions lead to the conclusion that there must be an optimum beam radius for the highest volume at a given pulse energy. Also, the ablation efficiency η_E and rate R_t follows the same form as the volume V (Fig. 5 b). For a given pulse energy E_p, the optimum beam radius w_{opt} could be calculated by $w_{opt} = e^{-1}w_{th}$, where $w_{th} = (2E_p/(F_{th}\pi))^{1/2}$ is threshold beam radius. The strategy of beam enlargement to reach the optimum fluence in this dissertation is called beam size optimisation method. The main advantage of this method is simultaneous optimisation of ablation efficiency and ablation rate, while keeping the optical power at its maximum. The main drawback is the bigger beam spot size, which results in the lower processing resolution.
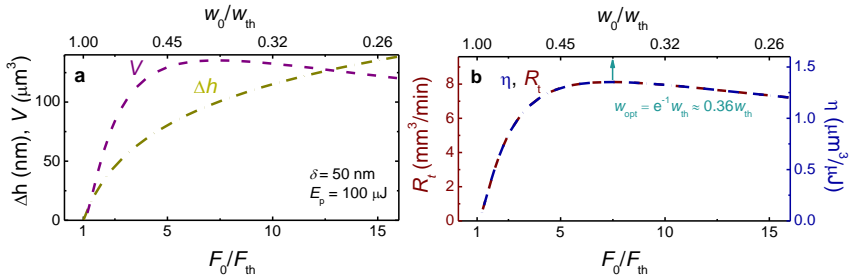
Fig. 5 Numerical representation of (13)-(16) equations, when effective penetration depth $\delta = 50$ nm and pulse energy $E_p = 100$ μJ. (a) The depth Δh and the volume V of the crater and (b) ablation efficiency and rate dependence on laser peak fluence F_0 normalised to threshold fluence F_{th} when beam size is reduced.

For modern ultrashort pulse lasers, which preserve similar average power over wide pulse repetition rates range, another optimisation strategy is possible. The increase in pulse repetition rate results in lower pulse energy, which brings fluence closer to the optimum [53–55]. It was shown than optimisation of pulse repetition rate in the range of $0.2 - 20$ MHz for machining of steel while keeping constant average power of 19 W leads not only to the high ablation efficiency but also surface roughness [55]. Nevertheless, typical industrial grade ultrafast lasers with average powers in the range of ~100 W usually can work in the highest pulse repetition rate of several MHz [56]. With F-theta lens of focal distance of ~100 – 160 mm, which focuses beam to a spot of $2w_0 = 40$ μm, we get a peak fluence F_0 of around $50 - 100$ J/cm^2, which is still very far away from an optimum fluence. Typical optimum fluence values are ~ $0.5 - 1$ J/cm^2 for steel [38,57,58] and silicon [40], ~ 2.5 J/cm^2 for copper [38,57,58], 2 J/cm^2 for aluminium [39]. To further reduce the pulse energy and fluence, burst lasers were utilised [59]. In addition, heat accumulation and plasma/particle shielding in hundreds of kHz range highly influences the ablation process [60]. While the influence of shielding on ablation efficiency is mostly negative [38], due to energy scattering and absorption in the plume, the influence of the heat accumulation can be both positive and negative [61]. The residual heat induced by previous pulses may not be removed fast enough via heat conduction from the interaction area. Therefore, heat accumulates, the quality of the processed surface and surrounding area suffers, the large heat affected zone and melt can be formed [41]. Therefore, fast scanning systems as polygon scanners are needed to scan laser beam in the range of hundreds of m/s and ensure low pulse overlap [62]. On the other hand, the heat accumulation can be beneficial for the ablation efficiency: in the multi-pulse laser processing, the laser pulse meets the material preheated by the previous pulses, therefore energy required to reach the boiling temperature of the matter is lower [42]. As a consequence,

the residual energy from the previous pulses is not completely lost in the surrounding, resulting in the increase of the ablation efficiency. Due to forementioned reasons burst lasers were widely investigated in the pursuit of material removal efficiency.

1.3 Bursts of pulses

Burst lasers instead of single pulse produce burst of pulses with intra-burst repetition rates of tens of MHz or several GHz, while typically burst repetition rate is in the range of hundreds of kHz (Fig. 6).
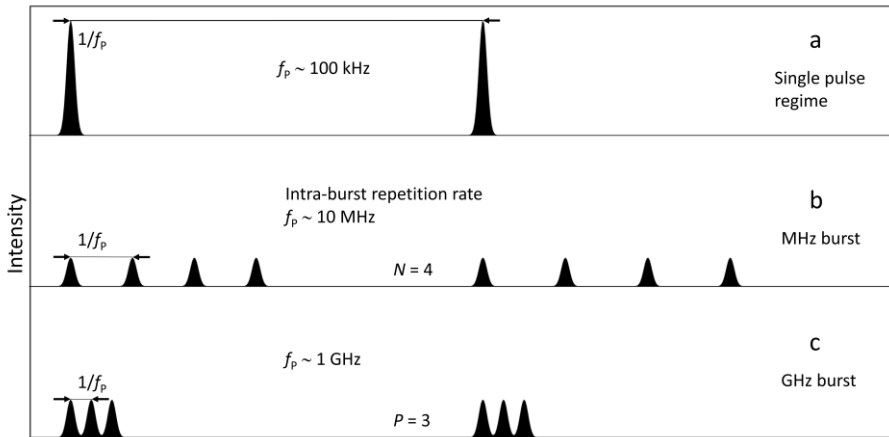

Fig. 6 Ultrashort pulse laser operation modes: (a) conventional, single-pulse, (b) MHz burst with $N = 4$ intra-burst pulses, (c) GHz burst with $P = 3$ intra-burst pulses.

Compared to conventional pulsed laser, the individual energy of one pulse within burst is lower as many times as there are intra-burst pulses and could be used to bring the pulse fluence closer to the optimum [59,63]. Therefore, the usage of bursts has to be beneficial in the context of utilisation of high-power for simultaneous high ablation efficiency and ablation rate processing. In the case of low repetition rate processing, the generated thermal energy has enough time between pulses to spread over the target and surrounding environment. Therefore, heat induced by every previous laser pulse is lost and not beneficial for the ablation process. For GHz burst processing the mechanism of material removal via ablation-cooled process was discussed, which claimed ablation efficiency increase due to the removal of excess thermal energy from the interaction zone with the successive pulses [1]. In addition, due to removal of thermal energy with ablated material, it was stated that ablation-cooling enables thermal damage-free laser processing. The

ablation-cooled material removal process is still highly debatable in the scientific community [64,65]. Nevertheless, the publication in the most recognized scientific multidisciplinary journal in the world *Nature* made a huge impact to the topic on laser burst material processing and was a motivation for other research groups. It seems that many laser processing parameters as intra-burst pulse repetition rate, total burst energy, individual pulse energy, number of pulses within burst determine the ablation results. Compared with conventional single-pulse processing, low ablation efficiency [66,67] and melt formation with burr and droplets was also reported for burst processing [68]. Due to thermal interaction and formation of remelt layer, laser polishing/smoothing of rough surface was realised by GHz burst pulses [67,69,70]. Also, the detailed comparison of 28-pulse 154 MHz burst with 175 nanosecond pulses revealed that in the case of silicon, stainless steel and copper the ablation mechanism is similar to the one of ns pulses [68]. The thermal origin of the GHz processing seems to be unquestionable. Another explanation of high ablation efficiency of GHz burst with hundreds of intra-burst pulses introduce heat accumulation model, where first part of pulses in the burst heat the target up to the high temperature and all following pulses introduce small amount of energy required to remove the material in the form of vapours [71,72] (Fig. 7). Therefore, the heat does not dissipate into the material and is used for ablation.
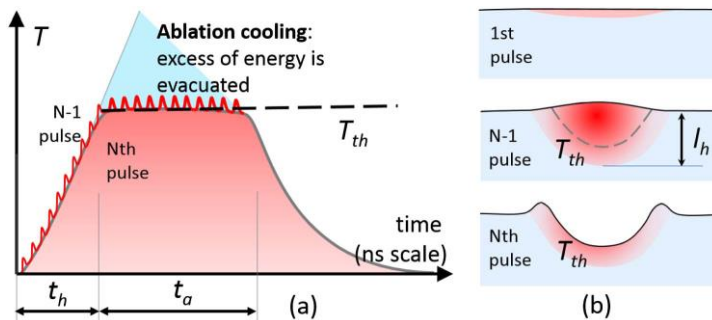
Fig. 7 Two-stage mechanism for GHz ablation. (a) Heating by accumulation effects during t_h, followed by efficient ablation of hot surface layer during t_a. (b) Crater generation mechanism: local temperature increase by heat accumulation and dissipation triggers a massive material ejection when achieving the critical temperature T_{th}; l_h – heat diffusion length within t_h. Reprinted with permission from [72] © The Optical Society.

In addition to the processing parameters, the processing approach has a huge impact on the ablation efficiency. It was shown, that copper ablation by 160-pulses 864 MHz burst in the drilling approach was about 10 times more efficient than milling [73]. This was explained by the different melt flow

during laser processing. In the case of drilling, in addition to evaporation the material removal takes place in the form of liquid, which is expelled from the crater due to high pressure. During milling the liquid flows back on the previously ablated surface and does not contribute to the material removal. Therefore, it is important to use the same processing approach and optimise the fluence before comparison of single-pulse and burst processing efficiencies.

In the case of MHz burst processing of copper, interesting phenomena are observed. It was shown that two pulses in the burst reduce the ablation efficiency approximately by 50% compared to single pulses. But adding the third pulse in the burst the efficiency strongly increases again and may even exceed the value of single pulses by ~15% [37,59]. The time duration after the first pulse hit the target is 12 ns for the intra-burst repetition rate of 83 MHz. This time is too short for the ablation cloud to dissipate, therefore the second pulse is shielded [74,75]. The evolving ablation cloud is heated, reignition of plasma starts, due to the second pulse–ablation cloud interaction-induced pressure, part of the material from the ablation cloud might be forced to redeposit back on the target, as a consequence the shielding plume is dispersed [74]. The redeposition of material is also confirmed by atomistic simulation [76]. The experimental work with high-precision balances shows thrust enhancement for two pulses burst with delay time of 12.2 ns, suggesting the redeposition of material [77]. For 3 pulses burst, the third pulse does not suffer the attenuation by the ablation plume, and energy is coupled to the target, therefore the ablation efficiency is high again. In addition, redeposited hot material enhances the absorption of the target and higher amount of energy is absorbed [78]. The calorimetric measurement for copper showed that absorptance for 3 pulses per burst is almost twice as high as one for the single pulse regime [40]. Also, the redeposited material pre-heats the interaction area for the third pulse, thus energy required to lift the temperature to the boiling point is smaller. For silver, gold [37], and aluminium [79] strong shielding of the second pulse with strong increase in ablation efficiency for the third pulse was also registered but the efficiency for 3 pulse burst was not higher than the one measured for single pulses as was for the copper case.

1.4 Laser-induced periodic surface structures (LIPSS)

Laser ablation is a perfect tool for micro-machining, where certain patterns are needed to be inscribed via material removal from a surface of a substrate. To initiate the material removal, the laser peak fluence must overcome the ablation threshold. If laser fluence is lower than the threshold, different phenomena of laser-matter interaction are observed, and so-called self-organised structures are formed. In simple words, self-organised means that the resulting surface topography after the laser irradiation does not correspond to the spatial intensity profile of the laser beam. The self-organised surface structures may consist of periodic or quasi-periodic microstructures, nanostructures, or hybrid micro/nanostructures. From the ablation efficiency point of view, the self-organised surface structures are highly inefficient, because in this regime the removal of the material is either minimal or none at all. Nevertheless, if functional properties of the surface can be reached without material removal, the process itself is highly efficient due to the savings of energy required for material evaporation. The utislisation of LIPSS in functional surface formation is wide and includes optical, surface wetting, biological, tribological and other applications [80]. The periodic self-organised surface structures are usually classified as nanometric laser-induced periodic surface structures (LIPSS) also called ripples or nanoripples, micrometric grooves, and nanospikes [81].

Shortly after the invention of the laser, in 1965, the formation of laser-induced periodic surface structures on semiconductors was demonstrated utilising a ruby laser [82]. Since then, researchers have been looking for an explanation of the LIPSS formation mechanism. It is generally known that the formation of LIPSS is universal and occurs on the surfaces of various types of materials like dielectrics, semiconductors, and conductors [83]. LIPSS usually emerge as a surface relief composed of periodic or quasi-periodic lines, which exhibit a clear correlation to the wavelength and polarization of the radiation [84]. LIPSS can be formed under various types of laser irradiation starting from continuous wave (CW) [85] to pulsed femtoseconds [86]. There are two categories of LIPSS that can be distinguished by the spatial period (Fig. 8 a). *Low spatial frequency* LIPSS (LSFL) exhibits spatial periods close to the laser wavelength ($\lambda/2 \leq \Lambda_{LSFL} \leq \lambda$) (Fig. 8 b), while *high spatial frequency* LIPSS (HSFL) typically have spatial periods much smaller than the laser beam wavelength ($\lambda/2 \leq \Lambda_{HSFL}$) (Fig. 8 c) [84]. Both LSFL and HSFL can be subdivided into two types. Ripples with $\Lambda_{LSFL} \sim \lambda$ and perpendicular to the laser beam polarization occurs on metals and semiconductors and are called LSFL type one (LSFL-I). The mostly accepted generation mechanism

of these ripples is explained by the interaction of laser beam with a secondary surface electromagnetic wave scattered at the rough surface [87,88] and may involve the excitation of surface plasmon polaritons (SPP) (Fig. 8 d) [88,89]. Surface plasmons are collective longitudinal oscillations of electrons propagating along a metal-dielectric interface at optical frequencies [90]. This field can interfere with the incident laser beam and then can lead to a modulated energy deposition, forming ripples at the surface [91]. Experimentally LSFL-I exhibit spatial periods lower than laser wavelength, therefore classical optical interference between incident laser light and scattered surface-electromagnetic wave does not fully explain the origin of ripples. The Drude-Lorentz model for surface plasmons shows that metal surface irradiated by ultrashort pulses can lead to a reduction of the surface plasmon wavelength (subsequently the ripples period) compared to its room-temperature value for particular conditions of plasma frequencies and varying electronic density [91]. Also, an experimental and theoretical work proposes that laser-induced surface plasmons (SP) are responsible for the formation of LSFL, through the initial SP-laser interference and the subsequent grating-assisted SP-laser coupling [92]. It is important to mention that LSFL-I can form also in the non-ablative regime via local melting and rapid solidification, especially for longer pulse durations or a high number of pulses, which induce melt film [84]. Also, there are other types of ripples, which are formed on dielectrics parallel to the laser beam polarisation and are called LSFL type two (LSFL-II). The mechanism of the LSFL-II is related to the so-called radiation remnants (RR) and their spatial period is $\Lambda_{LSFL} = \lambda/n$, where n is the refraction index of the dielectric material. The RR represent a specific non-propagating electromagnetic mode close to the rough surface, which is capable of extracting energy from the incident radiation and transferring it to the material at the associated spatial frequencies [84]. The second category of LIPSS, HSFL is observed on materials irradiated by ultrashort laser pulses and are either parallel or perpendicular to the laser beam polarization depending on the material. On dielectrics and semiconductors, HSFL-I consist of very narrow periodic grooves (few tens of nanometres) with depths of hundreds of nanometres. Shallow ripples forms on metals (HSFL-II) with depths of few tens of nanometres and their period is in the sub-100 nm range. Currently, these two types of HSFL are not distinguished in the scientific literature and the origin of HSFL is controversially discussed [84,93–95]. Even though the LIPSS is being investigated for more than a half of century there are still open questions about the specific characteristics and related applications [96].
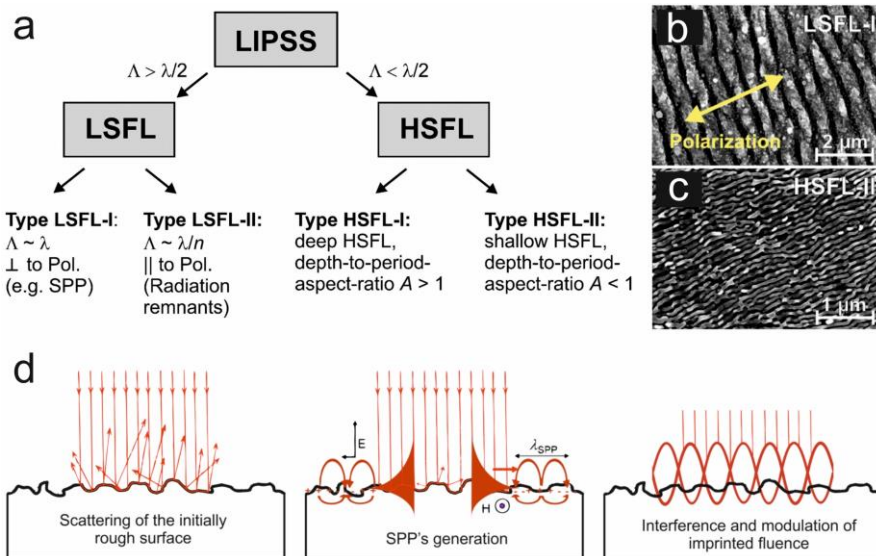
Fig. 8 (a) Classification scheme of fs-laser induced periodic surface structures. SEM micrographs of two distinct types of LIPSS on titanium surface after irradiation by fs-laser multiple pulses (b) LSFL-I and (c) HSFL-II. (d) Scheme of the mostly accepted electromagnetic formation mechanism of LSFL-I. The laser radiation impacts the sample surface from the top. Its initial surface roughness results in optical scattering (left) that may lead to the excitation of surface plasmon polaritons (middle) that interfere with the incident light and modulate the finally absorbed fluence "imprinted" in the material and selectively ablate the parallel periodic structures (right). (a) Reprinted with permission from [84], Copyright © 2016, IEEE. (b) and (c) Reprinted from [97], with the permission of AIP Publishing. (d) Reprinted with permission from [80]. Copyright 2020, Laser Institute of America.

1.5 Bio-inspired functional surfaces via laser structuring

The high demand and importance of biomimetic functional surfaces in daily lives are proven by numerous researches employing various fabrication techniques like 3D printing [98–104] (fused deposition modelling, direct ink writing, selective laser sintering, stereolithography, multijet printing, selective laser melting, electron beam melting), microcasting and subsequent nanospraying [105], nanoimprinting [106], photolithography [107], laser micro-machining [108,109], mechanical micro-machining and chemical etching [110], chemical film formation [111] and micro-embossing [112]. Laser micro-machining technology is attractive due to some specific features like: simple equipment – there is no need for vacuum of clean room; single step processing of micro and nanostructures, making the process efficient; contactless; possibility to process surface of 3D object; control of various processing parameters resulting in a great variety of possible structures;

possibility to process in different environments, such as gases, liquids and vacuum resulting in control of surface chemistry or contamination [113].

There is a great deal of interest of laser technology for the use of self-organised surface structures and directly written structures for creation of functional surfaces that have a specific optical, mechanical, or chemical property. In the case of ripples, due to the periodicity they are similar to the patterns of naturally occurring surfaces possessed by various plants and animals: the self-cleaning lotus leaf, the six-legged arthropod collembola, the Namib Desert beetle, snakes etc. For this reason, laser-induced self-organised surface structures are often referred to as bio-inspired or nature-inspired surfaces [81]. In the scientific literature there are examples of laser irradiated surfaces exhibiting anti-reflective, wetting, tribological, anti-bacterial, anti-corrosion, and anti-icing properties. In this chapter the wettability control and reduction of friction of a liquid or gas with the material will be briefly discussed.

1.5.1   Wettability

The wettability of a solid surface depends on the fluid surface energy γ of the liquid, the energy of the interface between the solid and the vapor γ_{sv}, and the energy of the interface between the solid and the liquid γ_{sl}. The internal contact angle θ between a liquid and a solid can be described by the Young's formula:

$$\cos\theta = \frac{\gamma_{sv} - \gamma_{sl}}{\gamma}. \tag{17}$$

Surfaces with a contact angle $\theta < 90°$ are called wetting and surfaces with $\theta > 90°$ are called non-wetting. When the liquid on solid is water, the wetting and non-wetting surfaces are referred to as hydrophilic and hydrophobic, respectively. When the angle θ exceeds 150°, the surfaces are called superhydrophobic (Fig. 9). The water that is on the superhydrophobic surface forms droplets that can easily roll on the surface at low inclination angles. Along the way, the droplets wet the contamination particles present on the surface and carry them away [114]. This property of a self-cleaning hydrophobic surface is also called the Lotus effect [115].
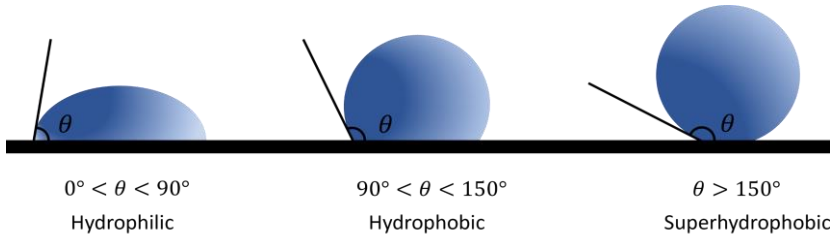
0° < θ < 90°   90° < θ < 150°   θ > 150°
Hydrophilic   Hydrophobic   Superhydrophobic

Fig. 9 The standard surface wettability classification: hydrophilic surface with contact angle lower than $\theta < 90°$, hydrophobic surface – $\theta > 90°$, and superhydrophobic surface – $\theta > 150°$.

Wettability is divided into three types of states according to surface geometry. Young type – when the surface is smooth (Fig. 10 a), Wenzel type – when the surface is rough (Fig. 10 b). For this reason, a surface roughness ratio r was introduced, defined as the ratio between the actual and projected solid surface area, for a smooth surface $r = 1$ and for a rough surface $r > 1$, which explains why the contact angle of the hydrophilic surface decreases with increasing surface roughness and why for the hydrophobic surface contact angle oppositely – increases. For rough surface contact angle is described by the formula:

$$\cos\theta^W = r \cdot \cos\theta. \tag{18}$$

The Cassie – Baxter type explains contact angles greater than 150°: in the presence of a hydrophobic surface, water tension is dominant in the system and for the fluid it is more energetically favourable to form a droplet resting on the tops of tips, while air fills the gaps underneath the droplet (Fig. 10 c). As a result, only a small portion of the surface is in the contact with the liquid.
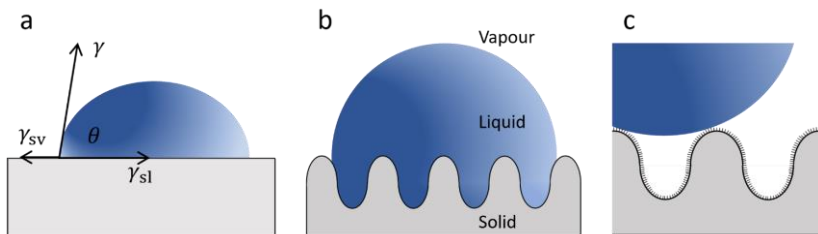

Fig. 10 Wettability types: (a) Young, (b) Wenzel, (c) Cassie – Baxter. Adapted from [114].

1.5.2   Friction drag

Any object moving relative to the flow of a gas, a liquid, or in touch with another moving solid surface is subjected to a force that operates in the opposite direction of its relative motion. This force is known as drag force F_D

in the case of a fluid and depends on the density of the fluid ρ, velocity of the object v, cross sectional area A of the object, and drag coefficient c_D [114]:

$$F_D = \frac{\rho v^2 c_D A}{2}. \tag{19}$$

The interactions between the fluid and a surface parallel to the flow, as well as the attraction between the fluid's molecules, generate friction (viscous) drag. Each fluid layer has a higher velocity as it moves away from the surface of an object until it reaches a layer where the fluid has the same velocity as the mean flow. Fluids with a higher viscosity (higher molecular attraction) have higher friction between fluid layers, resulting in a thicker fluid layer distorted by an object in a fluid flow. As a result, viscous fluids have a larger drag coefficient than less viscous fluids. Therefore, drag increases when fluid velocity increases. The increase in fluid velocity causes an increase in drag. The drag on an object is a measure of the energy required to transfer momentum between the fluid and the object to create a velocity gradient in the fluid layer between the object and undisturbed fluid away from the object's surface [116]. In turbulent flow molecules move not in the same relative direction, but in swirling and cross-stream motions, which dramatically increases the momentum transfer. In turbulent flow drag increases due to generation of vortexes.

1.5.3   Functional surfaces in nature

In the nature, there are examples of plants, beetles the evolution of which has led to the development of surfaces with superhydrophobic properties by combining hydrophobic substances (long chain fatty acids, waxes) with hierarchical surface structures consisting of waviness in the microscale and roughness in the nanoscale. The purpose of such structures is to keep the surface dry and clean to prevent the growth of unwanted microorganisms which are harmful to the plant. A typical example of such a plant is a lotus leaf with the surface of a hierarchical structure (Fig. 11 a – c) [117]. The surface of the springtail cuticle with a specific periodic structure has superhydrophobic properties (Fig. 11 d – f) [118]. There are examples in the nature of surfaces consisting of both hydrophilic and hydrophobic regions, such as the Namib Desert beetle. The tops of the hydrophilic bumps facilitate water condensation from the fog, while the superhydrophobic troughs form tracks for water droplets to roll to the mouth of the beetle (Fig. 11 g – i) [114].
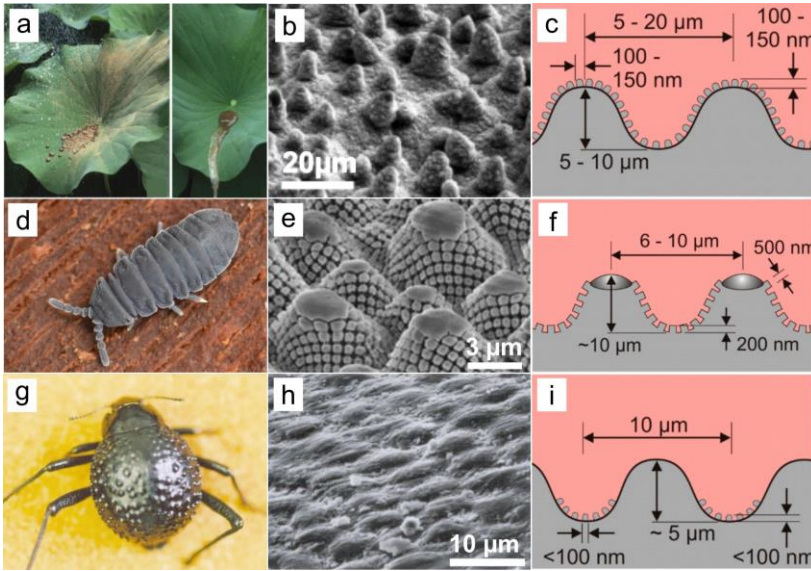
Fig. 11 Examples of superhydrophobic surfaces in nature: photograph, SEM micrograph and schematic picture of surface structure: (a – c) leaves of lotus water plant *Nelumbo nucifera* with self-cleaning ability, (d – f) Springtail cuticle *Tetrodontophora bielanensis* and (g – i) Namib dessert beetle *Stenocara gracilipes*. (a, b) Reprinted from [119], Copyright (2009), with permission from Elsevier. (d) Photo by Ryszard Orzechowski from insectarium.net, (e) Image was adopted from [118], Copyright © 2013, René Hensel et al, Under CC BY-NC-ND 4.0 (https://creativecommons.org/licenses/by-nc-nd/4.0/). (g, h) Reprinted by permission from Springer Nature Customer Service Centre GmbH [120], Copyright © 2013. (c, f, i) Images were adopted from [114] Under CC BY 4.0 (https://creativecommons.org/licenses/by/4.0/).

Many aquatic animals can move in water at high speeds, with a low energy input [121]. In fact, there is a paradox named after zoologist J. Gray, which assumed that the skin of dolphins should have some special drag reducing properties, that allow the animal to swim and accelerate faster than physiology would allow [122]. Fast-swimming sharks' skin protects them from biofouling and lessens the drag they experience as they travel through water. Dermal denticles, the microscopic scales that coat the skin of fast-swimming sharks, are formed like little riblets and aligned in the direction of fluid movement, are known to reduce the skin friction drag in the turbulent flow regime [116]. The use of shark-skin-inspired riblets has been demonstrated to reduce drag by up to 9.9% [123]. One of these fast-swimming sharks is Great white shark with scales present almost all over its body (Fig. 12). The riblets are V-shaped, about 200 – 500 µm in height, and regularly spaced with period of about 100 – 300 µm [121]. The small riblets that cover the skin of fast-swimming sharks work by impeding the cross-stream

translation of the streamwise vortices in the viscous sublayer [116]. This minimizes the occurrence of vortex ejection into the outer layer, as well as the associated momentum transfer. Vortices form above the riblet surface and remain restricted there in the turbulent flow regime. As a result, they only interact with the tips of the riblets and rarely cause any high-velocity flow in the valleys of the riblets. Since vortices only interact with the tips of the riblets, the surface area in contact with vortices are minimised, therefore the high-shear stresses are also minimised. In the valleys of the riblets low-velocity fluid flows which generates smaller shear stresses [81]. There is a huge interest of artificial fabrication of bio-inspired drag reducing surfaces employing various techniques [124].
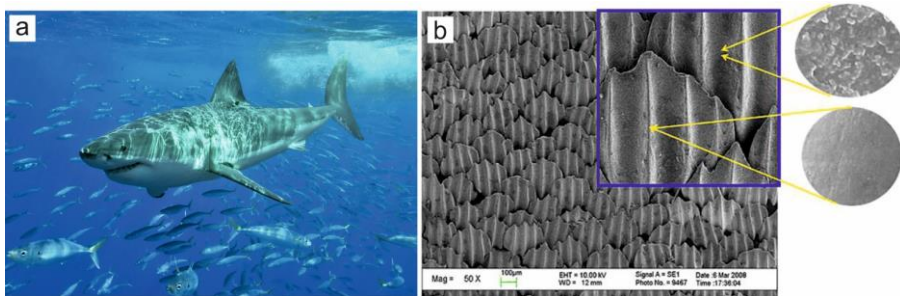

Fig. 12 (a) Photo of Great white shark (*Carcharodon carcharias*). (b) SEM image of the riblet structures of the Great white shark's skin. Image (a) by Terry Goss, CC BY 2.5, https://commons.wikimedia.org/w/index.php?curid=1561215. Image (b) was adopted from [125] Under CC BY 4.0 (https://creativecommons.org/licenses/by/4.0/).

1.5.4   Wettability control by LIPSS

Laser processing technique is simple, low cost, chemicals free, and it can be easily scaled up using commercially available industrial laser processing systems. Therefore, wettability control and creation of surface superhydrophobic surfaces are widely investigated in scientific community. Functional surfaces are investigated for various applications like self-cleaning [121], anti-fingerprint [126], anti-corrosion coatings [127], water-repellent textile [128], anti-bacterial surfaces [129] and fog harvesting [130]. The resistance to corrosion, contamination and bacteria are well desired properties, which can be achieved by laser micro-nano structuring and control of the wettability.

It is known that metallic surfaces after laser processing immediately exhibit hydrophilic properties and with time surfaces evolve to the superhydrophobic state [131]. It is related to the post-irradiation adsorption of airborne hydrocarbons or dissociative adsorption of CO_2 from the air forming hydrophobic carbonaceous compounds [131,132]. The interplay of periodic

pattern topography and surface chemistry is widely investigated [96,133]. Usually steady-state of wettability on metals is achieved after $10 - 20$ days [131,134]. Stainless steel (304L) irradiated by infrared 150 fs laser pulses with peak fluences of 0.78 J/cm^2, 2.83 J/cm^2, and 5.16 J/cm^2 in overlapped scanned beam strategy exhibited different topologies (Fig. 13 a). Utilisation of lowest fluence resulted in sample coverage by LIPSS, while increased fluence initiated formation of dual scale surface roughness with micro bumps and sub-micron ripples. Sample textured by LIPSS resulted in highest contact angle (CA) close to the 150°, while samples with dual scale roughness had CA of about 130° (Fig. 13 b). X-ray photoelectron spectroscopy (XPS) analysis revealed good positive correlation of carbon content with steady state contact angle (Fig. 13 b inset).
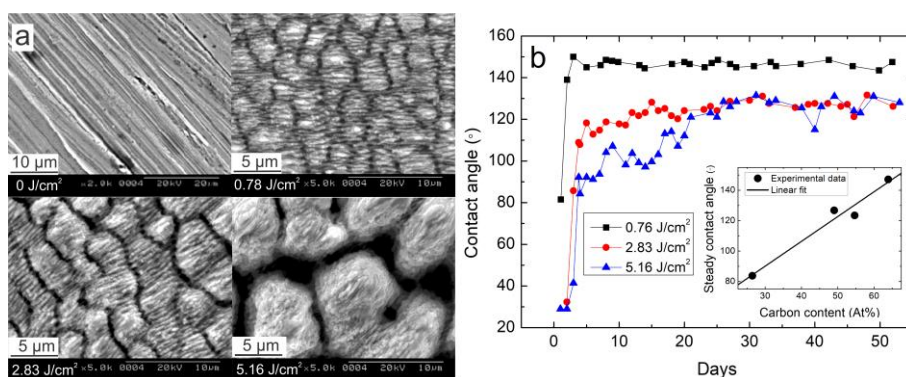

Fig. 13 (a) Stainless steel surface covered by LIPSS due to irradiation by 150 fs laser pulses with fluences of 0 J/cm^2, 0.78 J/cm^2, 2.83 J/cm^2, 5.16 J/cm^2. (b) Contact angle evolution over time. Inset: steady state contact angle correlation with carbon content on the irradiated stainless steel surface. Figures and experimental data adapted with permission from [131], Copyright 2009 American Chemical Society.

Ablation of trenches and formation of LIPSS were used to examine laser-based techniques for stainless steel surface wettability control [6,135]. For the production of superhydrophobic surfaces, laser processing parameters such as interline spacing for grid patterning and polarisation control for LIPSS creation have been proved to be critical. The static contact angle coverage for steel via laser structuring is between ~90°and 150° [6,135–137]. Dual scale patterning was realised by fs laser ablation of trenches and matrix (micro) and formation of LIPSS (nano) [135]. It was shown that dual scale patterning results in slightly higher contact angle values than single scale micro or nano patterning (Fig. 14).
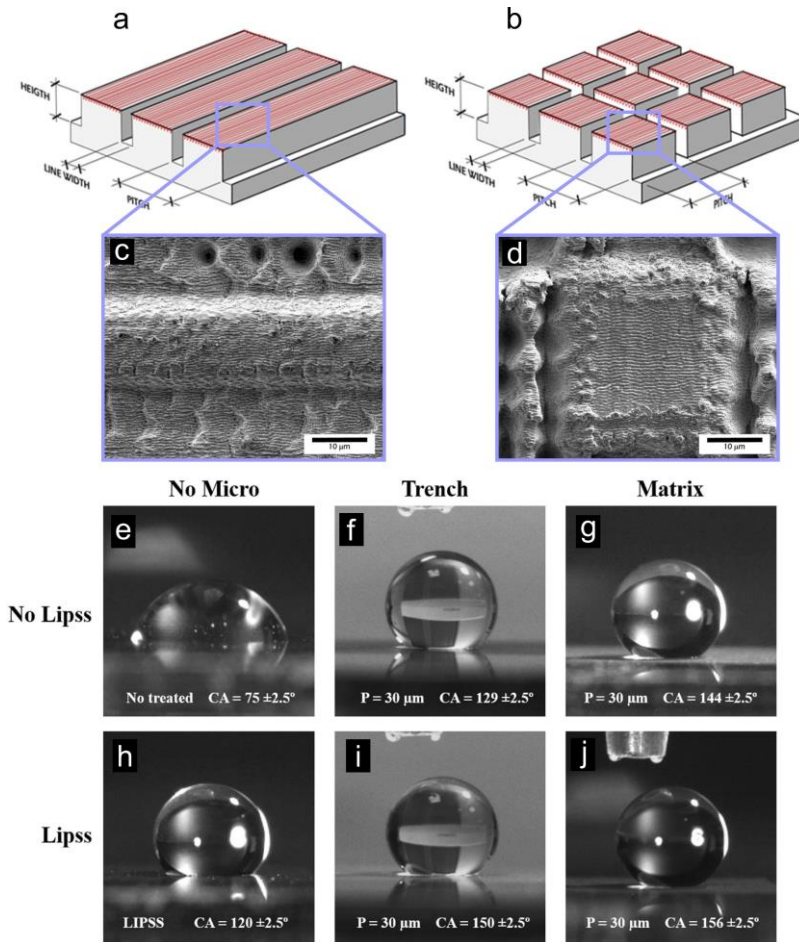
Fig. 14 Schematic representation of dual scale laser patterning by (a) ablation of trenches and (b) ablation of grid (matrix) covered by LIPSS. (c, d) SEM images of laser processed surfaces. (e-j) optical images of water droplet on laser processed surfaces. (e) no laser treatment, (f) ablation of trenches, (g) ablation of matrix, (h) formation of LIPSS, (i) trenches covered by LIPSS, (j) matrix covered by LIPSS. P – interline distance, CA – contact angle. Reprinted from [135], Copyright (2016), with permission from Elsevier.

1.5.5   Laser fabrication of drag reducing surfaces

There are various laser based techniques like laser interference lithography [138], laser-induced periodic surface structuring [139], direct laser structuring [108,109,140] employed for fabrication of bio-inspired tribological (drag force or dry friction reducing) surfaces. The direct laser structuring is based on laser ablation; therefore, it is capable to mimic a various microstructures found in nature. To perform a controllable laser ablation, programable galvanometer scanners or linear stages are needed to guide a laser beam over the sample surface in the predefined trajectory.

Usually, the movement control of laser beam is performed by specialised computer software, which generates a G-code from computer-aided design (CAD) files or simple built-in commands. Therefore, various patterns made of dimples, grooves and cavities can be easily inscribed into the surface (Fig. 15). To create a designed 3D surface topography, the subtractive micromachining is realised in layer-by-layer processing technique [141]. For this purpose, 3D model is sliced over vertical coordinate, resulting in numerous two-dimensional (2D) patterns scanned one after another starting from the top (top-down approach) (Fig. 16). If resulting surface has to be direct copy of 3D model, the model has to be inverted (combined with the defined size frame), otherwise negative cavity is milled – the technique used for mould fabrication.
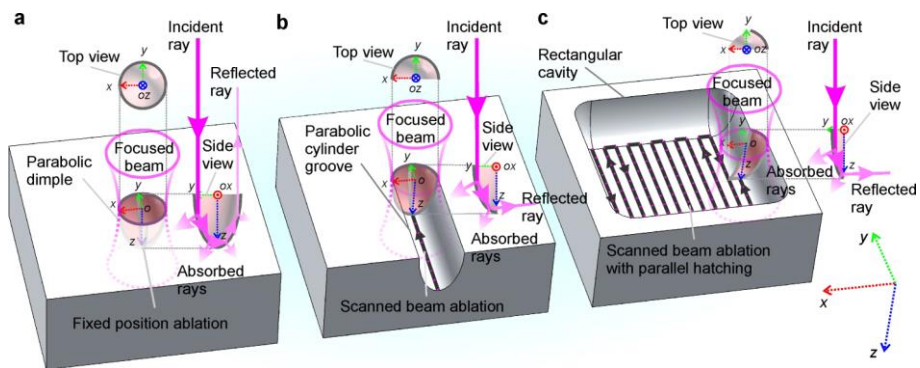
Fig. 15 Schematic illustration of laser structuring with (a) static beam – dimple ablation, (b) scanned beam – groove ablation (line scan trajectory) and (c) scanned beam with parallel hatching – rectangular cavity ablation (bidirectional snake scan trajectory). Image reprinted from [142]. Under CC BY 4.0 (https://creativecommons.org/licenses/by/4.0/).

Fig. 16 Visual example of 3D laser micro-machining realisation via top-down approach: 3D model is combined with frame and sliced over z coordinate into numerous 2D patterns later scanned by laser beam. On the right vertical lines represent hatching – area scanned by laser beam, white area – unprocessed part. Process is similar to sculpting, when unwanted material is removed from the bulk until desired surface is formed.

Usually, the design of shark skin is simplified to the fabrication of riblets utilised by the laser ablation of parallel grooves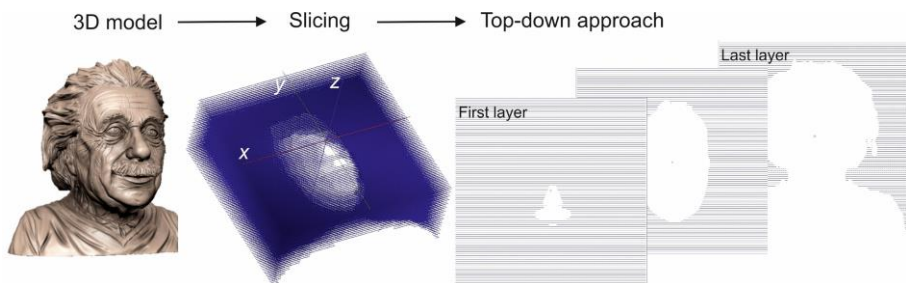. The extended investigation by Bixler *et al.* studied the influence of laser microstructured riblet geometry, fluid velocity (laminar and turbulent flow), fluid viscosity, riblet combinations to the drag reduction via pressure drop in the testing channel [143]. In this study the pressure drop reduction for laser fabricated segmented riblets of 19% in water and 13% in air was achieved. Continuous riblets shown better performance with air flow as compared to water flow. The continuous riblets may reduce cross stream movement with air more efficiently than with segmented riblets. The reasons are not completely known, but it was postulated that while lower viscosity air vortices rotate in the channel, the gap area between segmented riblets disrupts and unpins the vortices [143]. Laser engraving machine was used for fabrication of continuous riblets on the surface of organic glass plate. The maximum drag reduction of 8% was achieved for water flow [144]. Trapezoidal riblets with period of 60 µm and height of 30 µm was fabricated on Ti64 substrate by ultrashort laser pulses (Fig. 17) [145].
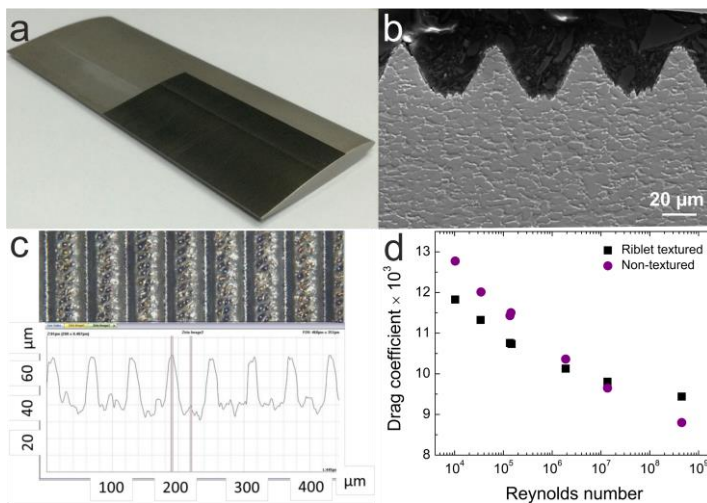
Fig. 17 Example of laser texturing by riblets: (a) photograph of partially (black area) textured aerofoil; (b) SEM image of microstructure; (c) 3D optical profilometer image and corresponding profile; (d) drag coefficient for non-textured and riblet textured samples versus Reynolds number. Reproduced from Ref. [145] with permission from Japan Laser Processing Society.

Compared with non-structured area, the riblets induce maximum of 10% reduction in wind test tunnel drag. In Fig. 17 d measured drag coefficient for laser textured and non-textured surfaces are shown versus Reynolds number, which is proportional to the mean flow velocity of wind. The riblet texturing

rate of 4.22 mm^2/min, material removal rate of 0.08 mm^3/min and ablation efficiency of 1.06 µm^3/µJ was achieved with average power of 1.32 W. In the meantime, a low production rate does not look highly attractive for direct laser texturing of large-area aerofoils of airplanes or blades of wind turbines (Fig. 18 a, c), the structuring of embossing drums for large-volume fabrication of riblet films [146,147] via roll-to-roll process could be a solution. Indeed, in the late 1990s polymeric riblet films produced by 3M Company were used on Airbus A340–300 (Fig. 18 b) aircraft by Cathay Pacific commercial flights, which observed the reduction of skin-drag up to 8% [148,149]. The usage of films was suspended due to various reasons like added weight, difficulties in shaping and long-time (one week per aircraft) of gluing, dirt attachment, non-attractive plastic marketing and similar. Nevertheless, the constantly increasing price of fuel, renews interest of shark skin technology. In 2019 4JET microtech GmbH and paint company Mankiewicz declared 1 m^2/min riblet texturing rate by direct laser interference patterning (DLIP) [150] technology directly on the outermost paint layer of the aircraft (Fig. 18 d), which according to the manufacturers meets the speed requirements for industry [151]. According to press release Lufthansa Cargo's entire Boeing 777 freighter fleet should be using film that mimics shark skin in the year of 2022 (Fig. 18 e, f) [152]. While exact fabrication process of riblet film is undisclosed, the film produced by Lufthansa Technik and BASF has been already tested in laboratory and real flight conditions for climate, ultraviolet (UV), fluid (water, oil) exposure, adhesion and functionality [153]. Another application were laser structuring could be directly applied to the metal surface involve fabrication of riblets on compressor blades [140]. It was shown experimentally that laser generated riblets on compressor blade reduce wall shear-stress up to 4% in the oil channel with optimal aspect ratio of riblet height to spacing being 0.5 and theoretically that ideal riblet geometry is trapezoidal. Recently it was successfully demonstrated that laser ablation could be used for fabrication of bio-inspired drag reducing fish scales [109,154]. In one of the studies, pulsed laser was used to create the inclined superhydrophobic, up to 4.8% in water drag reducing fish-scale like aluminium surface [109]. Compared to shark skin (simplified to riblets) the fish-scale like structure is more complex, thus 3D layer-by-layer micro-machining is more suitable than 2D pattern repeated multiple times, usually applied for riblet fabrication.

Fig. 18 Industrial applications of shark skin riblets for drag reduction. (a) Wind turbine (author Patrickmak, GNU Free Documentation License); (b) Airbus A340–300 aircraft with riblet film covered area [149]; (c) Riblet film produced by 3M Renewable Energy Division Laboratory tested on aerofoils for wind turbines [146] (reprinted with permission from ASME); (d) Riblets formed by DLIP method on outermost paint layer of aircraft (image rights: 4JET microtech GmbH) [151], (e-f) Lufthansa Cargo's Boeing 777 should be using riblet film by the year of 2022 (© Copyright Lufthansa Technik) [153].

2. EXPERIMENTAL SETUPS AND CHARACTERISATION

In the experiments various industrial ultrashort pulse lasers were utilised. Typical optical scheme consisted of laser source, mirrors to guide the beam, beam expander, galvanometer scanner, *XYZ* linear stages and in the case of cylindrical part processing – two rotary axes (Fig. 19 a, b). The variety of lasers and their main characteristics are listed in Table 1. The details of technical part of each experiment are reported in papers [A1-A7].

Table 1. Laser micro processing setups used in the experiments. See Fig. 19 b for burst and biburst operation mode illustration.

Laser model, manufacturer	Atlantic, Ekspla		Atlantic, Ekspla	Carbide, Light Conversion	Pharos, Light Conversion	Pharos, Light Conversion
Pulse duration	10 ps		10 ps	210 fs – 10 ps	210 fs	170 fs
Wavelength	1064 nm	355 nm	1064 nm	1030 nm	1030 nm	1026 nm
Average power	13 W	4.5 W	40 W	36 W	7.3 W	3.3 W
Repetition rate	100 – 500 kHz		1138 kHz	300 kHz	100 kHz	100 kHz
Irradiation mode	Pulsed		Pulsed	Burst, 64.5 MHz	Biburst, 64.7 MHz, 4.9 GHz	Pulsed
Scanner	Scangine 14, Scanlab	Scancube 10, Scanlab	Intelliscan 14, Scanlab	Intelliscan 14, Scanlab	Intelliscan 14, Scanlab	Brand not specified
F-theta lens	+80 mm	+176 mm	+100 mm, +160 mm	+100 mm	+100 mm	+290 mm
Experiment	Efficient ablation	Drag reducing riblets	3D micro-machining, cylindrical parts	High-power MHz burst	GHz, Biburst	Wettability
Paper	[A5, A7]	[A6]	[A4, A5]	[A3]	[A1]	[A2]

In this dissertation the methodology to accurately measure the ablation efficient was created. To calculate laser milling efficiency rectangular cavities with top dimensions in *XY* plane of 2×1 mm^2 and depth h in *Z* direction were engraved into the samples (Fig. 19 c). Rectangles were scanned multiple times to be measurable in depth by stylus profiler (Dektak 150, Veeco) and to have situation closer to the real-life application, where multiple scans are needed to reach the engineered depth. The bidirectional scanning of parallel lines separated by hatch distance Δy was used. In most of the cases hatch distance was kept constant of 10 µm. This value was chosen to be close to the focused beam radius, to have no less than 50% overlapped scanned lines forming uniform cavity. The depth and surface roughness R_a of the milled cavities were measured by the stylus profiler. Ablation efficiency η_E for every set of processing parameters was calculated by:

$$\eta_E = \frac{\Delta y v h}{P_{\text{ave}} n},\tag{20}$$

where v is the beam scanning speed, h is the cavity depth, P_{ave} is the average optical power and n – number of scans. In the case of laser drilling efficiency calculation, 10 irradiation events (pulses or bursts) were shot into the one spot to have a situation closer to real percussion drilling. Volume of the removed material was measured by 3D optical profiler (S neox, Sensofar) (Fig. 19 d). The ablation efficiency was calculated dividing the measured volume by the total accumulated energy on one spot.
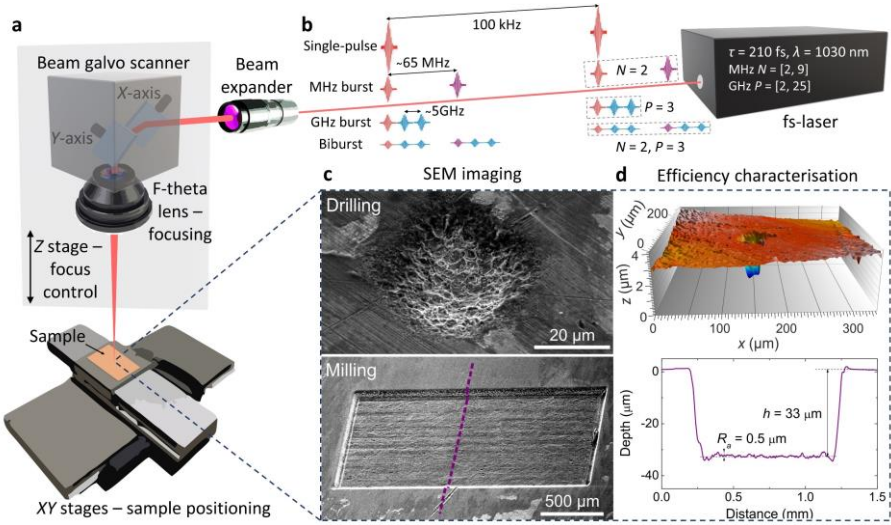

Fig. 19 (a) Typical scheme of laser processing setup consisting of ultrashort pulse laser, beam expander, galvanometer scanner, F-theta lens and XYZ linear stages. (b) Illustration of laser Pharos (Light Conversion) four operation modes: single-pulse, MHz burst, GHz burst and biburst. (c) SEM micrographs illustrating laser drilling and milling of copper and (d) corresponding graphs for efficiency calculation: map of laser drilled crater measured by 3D optical profiler and profile of laser milled cavity measured by stylus profiler.

According to the Eq. (15) the ablation efficiency is a function of peak fluence F_0, therefore to find maximum efficiency for each set of processing parameters the dependence of η_E versus F_0 had to be plotted. Afterwards maximum η_E value was extracted from $\eta_E(F_0)$ graphs. Peak laser fluence (Eq. (8)) can be changed by varying pulse energy or beam radius. In the case of pulse energy optimisation experiments, laser power was reduced by internal laser attenuator. While for beam radius optimisation, sample surface was positioned below focal plane by Z linear stage. Gaussian laser beam has

smallest radius w_0 in the waist position z_0, further from the waist expands according to [155]:

$$w(z) = w_0 \sqrt{1 + \left(\frac{(z - z_0)\lambda M^2}{\pi w_0^2} \right)^2} , \qquad (21)$$

where λ is the laser wavelength, M^2 is the beam quality factor. To measure beam radius $w(z)$ along z vertical position D-squared [26] method was used (more details about the procedure in can be found 1.2 Efficient laser ablation section).
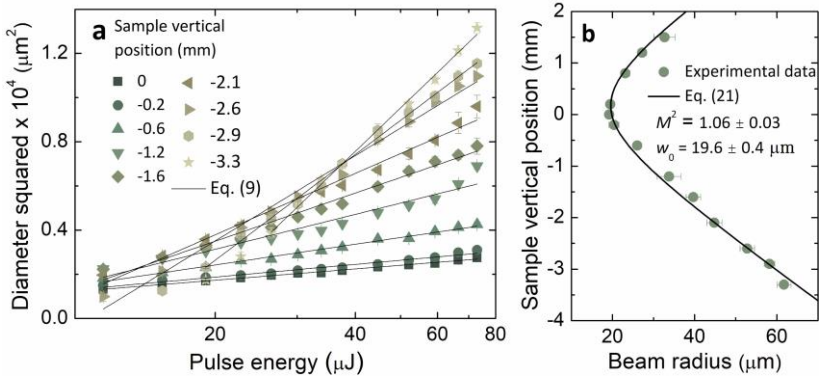

Fig. 20 Characterization of Gaussian laser beam. (a) D-squared method was used to measure beam radius at different z sample vertical positions. Experimental data fitted by laser damage diameter – pulse energy Eq. (9). (b) Gaussian beam propagation along z axis. Beam radius extracted from the D-squared method and fitted by the Gaussian beam divergence Eq. (21).

For the targets of laser ablation two metals and polytetrafluoroethylene (PTFE) commonly known brand name Teflon were used. Copper (CW004A, Ekstremalė) and stainless steel (1.4301, Ekstremalė) plates with dimensions of $50 \times 50 \times 5$ mm^3 were used for characterisation of ablation efficiency. These metals were selected due to the popularity in the industrial applications. Also, these metals are popular in the theoretical and experimental studies of laser ablation process, which allows easier comparison of the results. Copper had a purity of 99.9% and surface roughness of $R_a < 0.1$ µm, while stainless steel surface roughness was $R_a < 0.5$ µm. Copper cylinders with a diameter of 2 mm and length of 20 mm were used for the shark-skin-like texturing experiments in the rotary axes. Stainless steel samples were used in laser texturing experiments for wettability control. For the chemical element analysis scanning electron microscope (SEM) (JSM-6490LV, JEOL) equipped with the X-ray energy dispersive spectroscopy (EDS) (X-Max, Oxford Instruments) were used. The elemental analysis was carried out with

the 20 kV accelerating voltage and 50 nm electron beam spot size, limiting spatial resolution of the EDS spectrometer to 10 µm. The atomic chemical composition of the stainless steel at laser-untreated area measured by the EDS spectrometer was 35.9 at% C, 8.2 at% O, 11.0 at% Cr, 0.8 at% Mn, 39.8 at% Fe, 4.3 at% Ni. Atomic force microscope (AFM) (Dimension Edge, Bruker) was utilised for measurements of nano-scale laser-induced ripples. Height distribution measurements of $10 \times 10 \ \mu m^2$ surface areas were performed in tapping mode and ambient conditions. A commercial silicon probe with a tip diameter of < 10 nm (force constant – 40 N/m) was used. The PTFE (Virgin PTFE, Heliopolis) targets with the thickness of 0.5 mm were used in the laser texturing by shark-skin-like riblets for drag-reduction experiments. For sample visualisation, scanning electron microscope (SEM) (JSM-6490LV, JEOL) was used. The contact angle characterisation was performed by using the optical contact angle measuring and contour analysis system (OCA 15EC, Data-Physics Instruments GmbH) equipped with a charge-coupled device (CCD) camera to capture lateral images of water droplets applied on laser-structured and untreated steel. A droplet of deionised water with the volume of 3 µL was deposited by using a pipette (1 - 10 µJ Transferpette®, Brand). All contact angle measurements were done 15 days after the laser structuring, therefore, preventing the instabilities of contact angle change during the first 10 days after laser irradiation [131].

3. OPTIMISATION OF LASER ABLATION

3.1 Two methods for optimisation

The results published in paper [A5] are presented in this section. For the first time beam size optimisation method was applied for the rectangular cavity ablation. The experiments were carried out to learn more and validate the methodology for this optimisation method. Side tasks like influence of pulse repetition rate and pitch distance were investigated.

3.1.1   Pulse energy optimisation

Experiments of laser ablation of copper sample were carried out by ultrashort pulse laser (Atlantic, Ekspla) to find the optimal processing parameters for the highest ablation efficiency. The influence of beam scanning speed and pulse repetition rate on the ablation efficiency was studied as well. For the pulse energy optimisation method, the beam spot size was fixed to $2w_0 = 40$ μm. The pulse energy E_p was varied from 2.6 μJ to 26.2 μJ to change the laser peak fluence F_0 (Eq. (8)). In Fig. 21 a, the ablation rate dependence on the peak fluence is shown for various repetition rates and scanning speeds. The ablation rate was measured for five different pulse repetition rates from 10 kHz to 500 kHz. For each frequency, five different beam scanning speeds were investigated. One should note that the distance between laser beam spots (inter-line distance or pitch) on the sample surface was preserved the same, when the pulse repetition rate changed. The pitch $\Delta x = v/f$ was calculated as a ratio of the scanning speed v and pulse repetition rate f. Therefore, the space distance (Δx) effects were completely disregarded and time distance (1/f) influence to the ablation process could be better understood. Eq. (16) was used to fit the experimental data given in Fig. 21 a. The maximum ablation rates for all investigated frequencies were at a pitch of 0.1 μm and, as expected, at the highest possible peak fluence. By increasing pulse energy, the ablation rate is increased as well, but the dependence is not linear, which suggest, that there should be an optimum value of the pulse energy for a certain beam radius to reach maximum efficiency. In Fig. 21 b copper ablation efficiency versus laser fluence is plotted. The data are shown for the 100 kHz pulse repetition rate and scanning speeds of 5 mm/s, 10 mm/s, and 200 mm/s. The ablation efficiency had a maximum value at the optimum fluence point F_{opt}. Optimum point in this study varied between 1.5 J/cm^2 and 3.3 J/cm^2 depending on the scanning speed and pulse repetition rate.
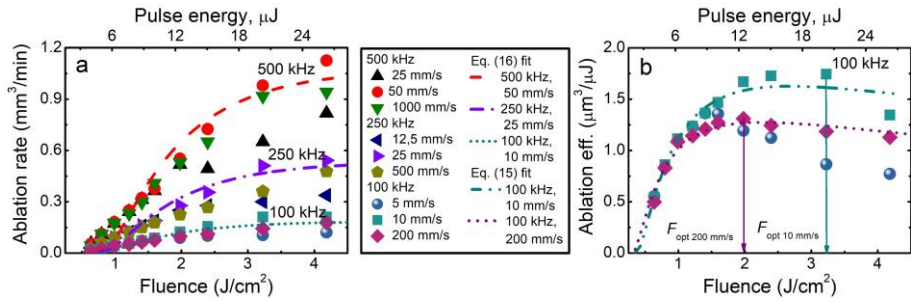
Fig. 21 Ablation rate and efficiency for copper milling, pulse energy optimisation. (a) Ablation rate versus fluence for 100 kHz, 250 kHz, and 500 kHz pulse repetition rates. For each repetition rate five different beam scanning speeds (two not showed) was used. (b) Ablation efficiency versus fluence for the 100 kHz pulse repetition rate and 5 mm/s, 10 mm/s, and 200 mm/s beam scanning speeds. An optimum fluence point slightly differs for different beam scanning speeds. Solid dots – experimental data, dashed and dotted lines – fit by Eq. (16) and Eq. (15). Pulse duration $\tau = 10$ ps, laser wavelength $\lambda = 1064$ nm, Gaussian beam radius $w_0 = 20$ µm on the target material, hatch $\Delta y = 10$ µm.

Processed surface was evaluated by measuring surface roughness R_a. The surface roughness of the bottoms of the cavities increased steadily with the peak fluence (Fig. 22 a). The ratio of the surface roughness with the depth of the cavity was calculated to validate the surface quality. The valley of the moderate quality in the fluence range of approximately $1 - 3$ J/cm^2 existed for the scanning speeds higher than $v > 5$ mm/s at the pulse repetition rate of 100 kHz (Fig. 22 b). Also, it is worth to mention that the maximum of ablation efficiency in this moderate quality fluence range was found. This means that energy excess, which was not used to remove the material, dissipated in the form of heat and deteriorated the surface quality. Cavities representing a typical quality of different fluence regions with corresponding profiles are shown in Fig. 22 c, d. All cavities were micro-machined with the hatch distance of 10 µm.
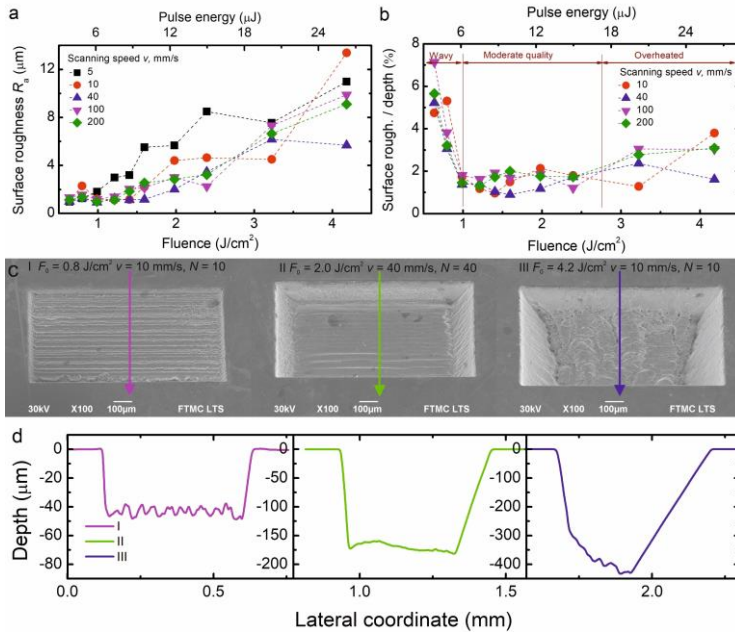
Fig. 22 Processed surface quality. The surface roughness (a) and the ratio of surface roughness with the cavity depth (b) versus fluence at various beam scanning speeds. Fluence range was divided into 3 regions, which represent wavy, moderate quality and overheated surface morphology. (c) Images and (d) profiles of cavities engraved into copper with a different set of laser processing parameters. Each SEM photo represents the typical quality for different fluence regions. Arrows represent profile measurement direction. Pulse duration $\tau = 10$ ps, laser wavelength $\lambda = 1064$ nm, pulse repetition rate $f = 100$ kHz, hatch $\Delta y = 10$ µm.

3.1.2   Beam size optimisation

For the beam size optimisation method, the pulse energy was fixed at $E_p = 26.2$ µJ, and the beam radius w_0 was varied from 20 µm to 65 µm by lowering sample up to 2.7 mm from focus plane. The optimisation was done for the same pulse repetition rates and scanning speeds as in pulse energy optimisation method. The results are shown in Fig. 23. The average laser power was always kept at maximum of 13 W. Therefore, ablation rate and efficiency were optimised simultaneously. The optimal pitch was at 0.1 µm for all investigated scanning speeds. The sudden drop of ablation rate for $v = 25$ mm/s at $f = 250$ kHz and $v = 50$ mm/s at $f = 500$ kHz was observed for the peak fluences higher than $F_0 = 2.3$ J/cm^2 (Fig. 23 c, d). This behaviour was not seen for the pulse repetition rates until 100 kHz (Fig. 23 a, b). Similarly, for the slowest scanning speed (the pitch of 0.05 µm), the drop was seen after 1.5 J/cm^2 for all pulse repetition rates. This means that slow scanning speed and specific critical fluence reduces the ablation efficiency. The reduction can be explained by the heat accumulation and the formation of the oxidised

bumpy surface. The bumps reduced the measured volume of the cavity (Fig. 23 e). The change of surface quality, followed by the drop of the ablation efficiency, is explained by the model of heat accumulation by Bauer *et al.* [41]. Each laser pulse raises the temperature of the sample by the particular value until the temperature saturates. The saturation temperature depends on the initial sample temperature, pulse repetition rate, scanning speed and laser fluence. It is shown that while other parameters remain constant and the scanning speed is increased, the transition from a low-quality to high-quality processed surface happens at the critical scanning speed v_{crit}. The transition can be associated with a decrease of ablation efficiency after fluence of 1.5 J/cm^2 for the pitch of 0.05 μm for all tested repetition rates. While for the pitch of 0.1 μm, this transition is only seen for $v = 25$ mm/s at $f = 250$ kHz and $v = 50$ mm/s at $f = 500$ kHz repetition rates after the peak fluence of 2.3 J/cm^2 (Fig. 23). All other scanning speeds were higher than v_{crit}, and a decrease in efficiency was not observed.
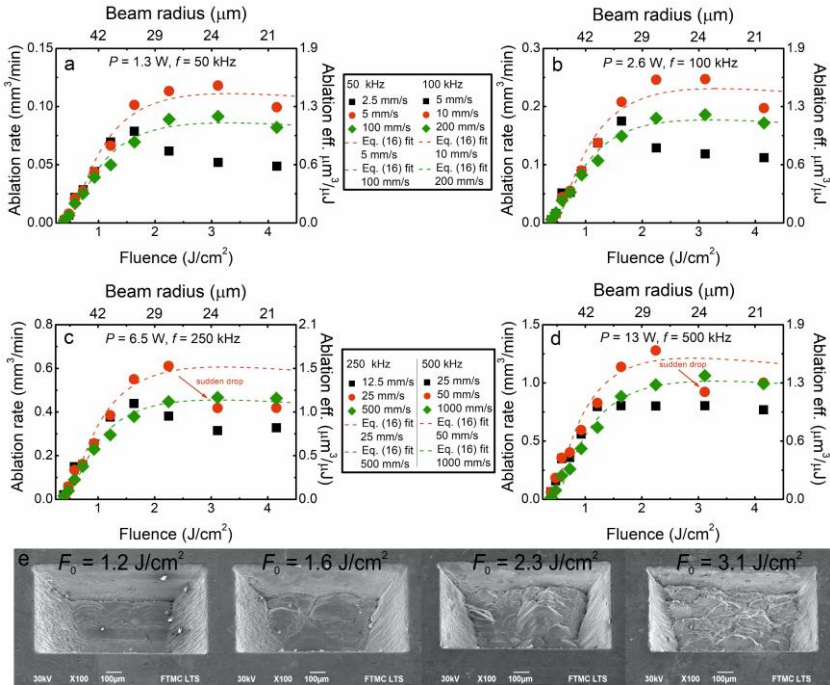
Fig. 23 Ablation rate, efficiency (a – d) and SEM images (e) of copper milling, beam size optimisation. (a) Laser average power $P = 1.3$ W, pulse repetition rate $f = 50$ kHz; (b) $P = 2.6$ W, $f = 100$ kHz; (c) $P = 6.5$ W, $f = 250$ kHz; (d) $P = 13$ W, $f = 500$ kHz. Solid dots – experimental data, dashed and dotted lines – fit by Eq. (16); (e) Cavities engraved into copper, which show a sudden drop in the ablation rate due to the formation of the bumps; beam scanning speed $v = 25$ mm/s, a number of scans $N = 10$, pulse repetition rate $f = 250$ kHz. Pulse duration $\tau = 10$ ps, laser wavelength $\lambda = 1064$ nm, hatch $\Delta y = 10$ μm.

To conclude, we state that a low scanning speed increases heat accumulation which helps to fasten the ablation. On the other hand, this scanning speed has to be used only for low repetition rates. While going to the higher repetition rates, a faster scanning speed has to be used, which does not cause ablation efficiency decrease due to heat accumulation at fluences lower than optimal.

3.1.3   Pitch distance

The overall maximum ablation efficiencies versus pitch for different repetition rates extracted from the pulse energy and beams size optimisation methods are shown in Fig. 24. The highest efficiency at the pitch of 0.1 μm was for both optimisation methods. The drop in efficiency at 0.05 μm could be explained by taking into account the geometry of the process. It is harder to remove the same amount of material from the deep hole (or groove) than from a surface that is almost flat. Firstly, a laser beam suffers multiple reflections from the sides of the cavity, meaning that less energy is used for the bottom ablation. Secondly, if multiple pulses ablate the cavity, the effective laser fluence drops down due to parabolic profile of the dimple and inclined walls. Thirdly, the evaporated material must leave the cavity. While leaving the deep cavity, the material has a chance to be redeposited on the sidewalls and block the path for the incoming pulsed beam [156]. From the other side, the drop of efficiency at the pitch higher than 0.1 μm can be explained by a higher ablation threshold for the lower number of pulses per spot. The ablation threshold depends on the number of pulses N per spot and decreases with increasing N (Eq. (10)) [47]. For example, at the pitch of 0.1 μm, the number of pulses per spot was 400 while for the 1 μm – only 40. Therefore, for fast scanning speed, the number of pulses per spot is reduced, and the ablation threshold remains high, meaning more energy is needed to remove the material.
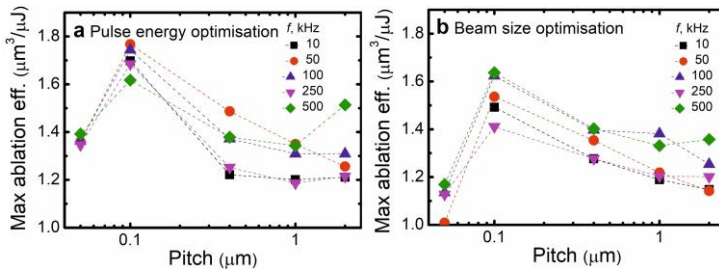

Fig. 24 Maximum ablation efficiency versus pitch distance for copper milling. Data from the (a) pulse energy optimisation method; (b) beam size optimisation. The peaks in the maximum ablation efficiencies were at the pitch of 0.1 μm. Pulse duration $\tau = 10$ ps, laser wavelength $\lambda = 1064$ nm, hatch $\Delta y = 10$ μm.

3.2 Model of advanced laser scanning

The results published in paper [A7] are presented in this section. During the previous experiments (Section 3.1) the clear influence of pitch distance for ablation efficiency was observed. Nevertheless, there was no theoretical model, which could be applied to explain the experimental results. Therefore, a semi-empirical model incorporating the ablation threshold incubation and depth saturation of the dimple was created.

3.2.1 Ablation model of rectangular-shaped cavity

The laser ablation model of rectangular-shaped cavity including the incubation phenomenon and the saturated ablation depth for multi-pulse processing has been proposed in this work. The graphical representation of a theoretical model in the case of rectangular-shaped cavity ablation is given in Fig. 25.
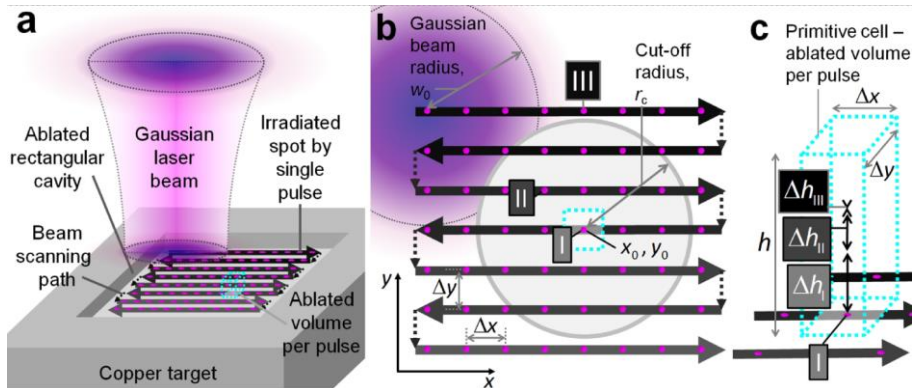

Fig. 25 Graphical representation of the laser ablation model. (a) 3D scheme of the laser ablation model of a rectangular cavity by parallel lines. Solid circles represent the array of spots irradiated by single laser pulses. The black line with arrows represents the beam scanning path. The cube in the centre by a dashed cyan line represents the primitive cell – volume ablated by a single pulse. (b) View from the top. The beam is scanned from left to right and from top to bottom leaving a quadratic array of spots. Δx and Δy represent the lateral distances between adjacent laser pulses (pitch) and scanned lines (hatch), respectively. The single laser pulse ablates the area marked by the cyan dashed line rectangle with the lateral dimensions of $\Delta x \cdot \Delta y$ in the position (x_0, y_0) marked by (I). Grey circle with the centre coordinates (x_0, y_0) represents the active ablation area with the cut-off radius r_c. The non-zero ablation depth is achieved from the pulses within an active circle (II). All the laser pulses in position (III) outside the cut-off area have zero ablation depth in position (I). (c) 3D representation of the ablated volume per pulse. The maximum ablated depth in the active area from the central pulse (I) is given by h_I. The non-zero ablated depth by pulse (II) in the active area is given by h_{II}. The zero-ablation depth from pulses outside the active (III) area is given by h_{III}.

The laser beam is scanned at a certain speed in parallel lines over the copper target, and the rectangular shape cavity is ablated (Fig. 25 a). It can be assumed that a single laser pulse ablates the primitive cell marked in a cyan dashed line with the volume lateral dimensions of Δx and Δy and height of h:

$$dV = h\Delta x\Delta y. \tag{22}$$

The primitive cell is an imaginative concept of the laser ablation volume per single pulse. The volume of the primitive cell is equal to the volume of the rectangular cavity divided by the total number of pulses applied. However, the depth of the primitive cell is influenced by many surrounding pulses within the cut-off radius. The beam scanning path consisting of the parallel scanned lines of the laser beam is shown (Fig. 25 b). Three main areas are marked by Roman numerals, and they represent the irradiation points of a different origin: (I) is a selected central point where ablation volume per single pulse is calculated; (II) is any point in the active area pulses influence the ablation depth at the (I) position with a non-zero ablation depth; (III) the irradiation points outside the active area laser pulses have zero influence in the ablation depth at the selected point of interest (I). The 3D representation of a primitive cell of ablated volume per pulse is shown in (Fig. 25 c). The symbols Δh_I, Δh_{II} and Δh_{III} represent the ablated depths of three points of interest in Fig. 25 b (I), (II) and (III), respectively. The overall ablated depth consists of the ablated depths from pulses from the active area. The total ablation depth per pulse is evaluated by summing all the ablation depths of surrounding irradiated spots in x and y directions which are in the range of a critical radius r_c:

$$h = \sum_{x,y}^{(x-x_0)^2+(y-y_0)^2\le r_c^2} \Delta h_{x,y} \tag{23}$$

the coordinates $x = \Delta x \cdot i$ and $y = \Delta y \cdot j$, where i and j are integer numbers. The coordinates of the transverse pulse positions on the sample are indicated by solid magenta dots (Fig. 25). The ablation rate can be assumed as:

$$\frac{dV}{dt} = f_p h\Delta x\Delta y, \tag{24}$$

where f_p = 100 kHz is the laser pulse repetition rate. The main purpose of the proposed model is to calculate the ablated volume per pulse of the scanned laser beam by taking into account the incubation phenomenon and saturation of ablation depth for increasing number of pulses per spot. The results of ablation using picosecond laser treatment at different numbers of pulses per spot (N = 1, 10, 100, and 1000) for copper are presented in Fig. 26 a.
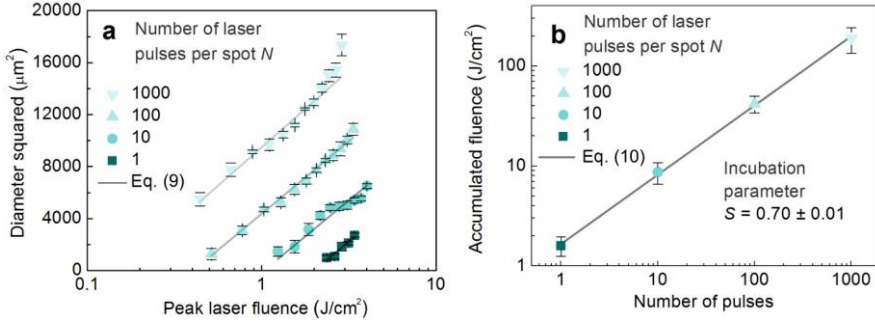
Fig. 26 Multi-pulse incubation behaviour of copper after a picosecond laser treatment. (a) Squared diameters D^2 of the ablated areas of copper in dependence on the peak laser fluence F_0 at a different number of pulses per spot N. Solid dots - experimental data points, solid line - fit by Eq. (9). (b) Accumulated laser fluence $N \times F_{th}(N)$ versus a number of laser pulses per spot N. Solid dots - experimental data points, solid line - fit by Eq. (10). Pulse duration $\tau = 10$ ps, laser wavelength $\lambda = 1064$ nm, repetition rate $f_p = 100$ kHz.

The slope of the straight lines provides information about the Gaussian beam radius $w_0 = 41.8 \pm 2.1$ µm on the target material from Eq. (9). The parallel lines represent the fixed slopes because of the same spot size on the sample. The extrapolation of lines at $D^2 = 0$ µm gives the copper ablation threshold fluences for various number of pulses per spot: $F_{th}(1) = 2.0 \pm 0.35$ J/cm^2; $F_{th}(10) = 0.87 \pm 0.21$ J/cm^2; $F_{th}(100) = 0.42 \pm 0.08$ J/cm^2; $F_{th}(1000) = 0.19 \pm 0.01$ J/cm^2. The accumulated laser fluence $N \times F_{th}(N)$ versus a number of pulses N for copper are given in Fig. 26 b. A calculation by Eq. (10) yields the accumulation coefficient $S = 0.70 \pm 0.01$.

A relation of the ablation depth per pulse can be described by Eq. (12). If many pulses N are applied per single spot, ablation depth $h(N)$ increases up to a material and laser dependent pulse number N_0 and then reaches saturation [27,157–160]. However, an analytical expression is not found in the scientific literature for a prediction of ablation depth growth and saturation with increasing number of pulses per spot. In this work, the analytical function of ablated dimple depth for multi-pulse irradiation has been empirically constructed:

$$h(N) = \delta(1) \ln \left(\frac{F_0}{F_{th}} \right) \left[N - \Delta N \ln \left(1 + e^{\frac{N - N_0}{\Delta N}} \right) \right], \qquad (25)$$

where $\delta(1)$ is the energy penetration depth for a single laser pulse, ΔN is saturation softness. We have chosen the soft saturation function with linear rise in the initial laser pulses $N < N_0 - 3\Delta N$, rise and saturation settling in the range $N_0 - 3\Delta N \leq N \leq N_0 + 3\Delta N$, and saturation after $N > N_0 + 3\Delta N$. This function is known as softplus function [161] and is becoming a saturation or

ramp-saturation function with $\Delta N = 0$. The parameters N_0 and ΔN have the physical meaning of pulse number required for saturation to begin and pulse number required for saturation settling, respectively. The selected Eq. (25) has an advantage of having two parameters with defined physical meanings required to describe the saturation phenomenon. The function with initial linear increase has been chosen because straight-line increase in ablation depth versus number of pulses has been experimentally observed in numerous scientific works [162–167]. The saturation after certain number of laser pulses has been also observed experimentally [158,160,168]. Therefore, the empirically selected function Eq. (25) fulfilled our needs of a fully analytical expression to be later used for approximation of experimental data, derivation of saturation parameters, and calculation of ablation rates in our numerical modelling.

The dimples on a copper target were ablated by using a Gaussian beam by controlling the number of incident pulses per spot. The dimple depth has been experimentally measured by using an optical microscope and the focus knob technique described in [169]. The method is based by the position difference measurement of the top and bottom of the object, using the markings on the fine-focus knob of the microscope. The optical microscope was equipped with XYZ stage and a 100X microscope objective with NA = 0.9 and depth of field of 0.19 µm have been used. The z accuracy of the fine-focus knob was 1 µm. The depth of field of the objective was much smaller than the accuracy of the fine-focus knob. The depth of ablated dimple dependence on the laser pulses per spot is given in Fig. 27 a.
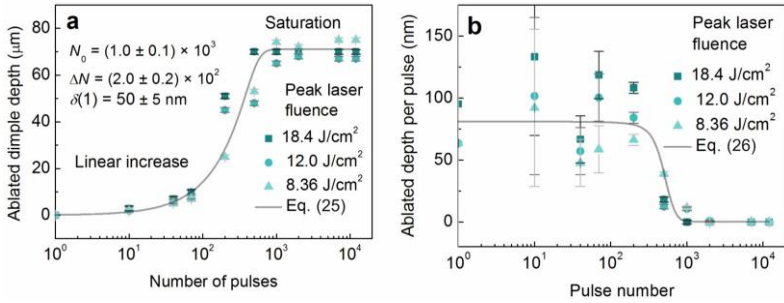
Fig. 27 Multi-pulse saturation behaviour of an ablated dimple. (a) The ablated depth of dimple dependence on a number of pulses per spot. Solid dots - experimental data points at different peak laser fluence values, solid line - fit by Eq. (25) with $N_0 = (1.0 \pm 0.1) \times 10^3$, $\Delta N = (2.0 \pm 0.2) \times 10^2$ and $\delta(1) \approx 50 \pm 5$ nm. (b) Ablation depth per pulse dependence on pulse number at different peak laser fluence values. Solid dots - experimental data points, solid line - fit by Eq. (26). Pulse duration $\tau = 10$ ps, laser wavelength $\lambda = 1064$ nm, repetition rate $f_p = 100$ kHz, peak laser fluences used $F_0 = 18.4$ J/cm^2 ($w_0 = 21.2$ µm), $F_0 = 12.0$ J/cm^2 ($w_0 = 31.5$ µm), and $F_0 = 8.36$ J/cm^2 ($w_0 = 41.8$ µm).

The ablated dimple depth increases with the number of pulses applied have been tested using three values of peak laser fluences and similar saturation behaviour has been observed for all fluences (Fig. 27 a). The fit of experimental data points by Eq. (25) provides: saturation value of $N_0 \approx (1.0 \pm 0.1) \times 10^3$, the saturation softness of $\varDelta N \approx (2.0 \pm 0.2) \times 10^2$ pulses, and penetration depth for single pulse irradiation of $\delta(1) \approx 50 \pm 5$ nm. The fit has a good agreement with the experimental data. For small irradiation doses $< 10^4$ J/cm^2, the depth of the dimple increases linearly with an increasing number of laser pulses. However, after reaching the saturation value of $> 10^3$ pulses, the depth of the dimples stops growing and saturates. By differentiating the Eq. (25) for a given laser fluence by the number of pulses, the ablated depth per pulse dependence on pulse number is achieved:

$$\Delta h(N) = \frac{\partial h(N)}{\partial N} = \frac{\delta(1)}{1+\exp\left(\frac{N-N_0}{\Delta N}\right)} \ln\left(\frac{F_0}{F_{\text{th}}}\right). \tag{26}$$

The function Eq. (26) has constant value for the initial laser pulses $N < N_0$ - $3\Delta N$, followed by the decrease to zero in the range N_0 - $3\Delta N \leq N \leq N_0 + 3\Delta N$, and a zero value for the pulse number exceeding $N > N_0 + 3\Delta N_0$. By calculating the first derivative of data points of Fig. 27 a, the depth per pulse dependence on the pulse number can be achieved (Fig. 27 b). For a large number of laser pulses $> 10^3$, the ablated depth per pulse has a value close to zero. The data points are scattered from ~ 50 to ~ 125 nm. However, its average value stays constant at around $\Delta h(N < 300) \approx 60$ nm. The reason for the high scattering of the data points is the large relative errors of the focus-knob method for small depths of $< 20 \, \mu$m [170] (Fig. 27 a, $N < 300$) and consequently amplified scattering of its first derivative (Fig. 27 b, $N < 300$). However, despite a large scattering of the experimental data points and large measurement errors, the fit of experimental data points by Eq. (26) has a good agreement (Fig. 27 b).

The depth reduction and saturation behaviour with an increase of number of laser pulses is mostly related to two physical aspects in the keyhole evolution: recast layer formation and multiple reflections. The redeposition of the ablated material and recast layer formation in laser drilling has already been explained in great detail in ref [171]. Geometrical aspects of deep dimple ablation and multiple reflections influence in keyhole evolution has already been investigated in refs [172,173] and refs [174–177], respectively. Therefore, we did not want to go into the physics of already well-known aspects of multi-pulse ablation. Our main goal of this research was to show the responsible combination of physical effects related to the laser ablation and their influence on the material removal rate of the rectangular shape cavity

formation. Our approach was to directly compare experimental data with simulation results of the proposed model.

The model incorporated a numerical calculation of an equation system with the input of the copper ablation parameters. All laser ablation parameters required for the proposed ablation model of the rectangular shape cavity are given in Table 2.

Table 2 Irradiation parameters used for numerical simulation of the ablation model.

Parameter	Symbol	Value	Unit
Saturation value	N_0	$(1.0 \pm 0.1) \times 10^3$	pulses
Saturation softness	ΔN	$(2.0 \pm 0.2) \times 10^2$	pulses
Incubation parameter	S	0.70 ± 0.01	a.u.
Ablation threshold for one pulse	$F_{th}(1)$	2.0 ± 0.35	J/cm^2
Penetration depth for one pulse	$\delta(1)$	50 ± 5	nm

For the selected point of interest (I) (Fig. 25 b) the active circle area πr_c^2 with the cut-off radius r_c. All the laser pulses within this radius have non-zero ablation depths in position (I). Ablation will not be possible by the laser pulses, which centre positions x and y are outside of cut-off radius as $(x - x_0)^2 + (y - y_0)^2 > r_c^2$, because laser fluence from the Gaussian wings will be below the threshold for multi-pulse ablation. The number of all those pulses N within the cut-off radius can be evaluated as a ratio between the active circle area and the primitive cell base area:

$$N \approx \frac{\pi r_c^2}{\Delta x \Delta y}, \tag{27}$$

where Δx and Δy are the distance of the irradiation spots (pitch and hatch) in the transverse directions x and y, respectively. On the other hand, the cut-off r_c of the ablated area evaluated by taking into account that in the processed area N pulses are absorbed, and the ablation threshold is decreased. From Eq. (9) and (10):

$$r_c = w_0 \sqrt{\frac{1}{2} \ln \left(\frac{F_0}{F_{th}(1) \cdot N^{S-1}} \right)}. \tag{28}$$

By numerically solving Eq. (27) and (28) the cut-off radius and the number of laser pulses per spot can be evaluated. The inter-pulse distance Δx and the distance between scanned lines Δy have been chosen with equal values in order to reduce the number of laser processing parameters. Moreover, they can be replaced by an experimentally controllable processing parameter – a beam scanning speed v on the sample:

$$\Delta x = \Delta y = \frac{v}{f}, \tag{29}$$

where f is the pulse repetition rate. Therefore, the main well known equations, defining the laser ablation by a Gaussian laser beam were included into this model: diameter squared of the ablated crater dependence on the peak laser fluence by Eq. (9); incubation behaviour for multi-pulse treatment by Eq. (10); ablation depth dependence on the laser fluence by Eq. (12); saturation of ablation depth by Eq. (25).

3.2.2   Experimental and modelling results of rectangular cavity ablation

The ablation rate has been tested experimentally and theoretically at various beam scanning speeds (inter-pulse distances) and spot radiuses on the sample (peak laser fluences). The ultrashort pulse laser (Atlantic, Ekspla) with pulse duration of 10 ps, irradiation wavelength of 1064 nm, pulse energy of 130 μJ, and pulse repetition rate of 100 kHz was used to ablate an array of rectangular areas in the copper plate, and ablation rate was measured (Fig. 28 a). Eqs. (10), (23), (24), (26)-(28) have been solved numerically by using the measured ablation characteristics of copper from Table 2 and symbolic/numeric computing software (Maple, Maplesoft). The calculated ablation rate versus laser processing parameters is given in Fig. 28 b. The series of cross sections from the experiment and model with variable peak laser fluence (from 1.20 J/cm^2 to 18.4 J/cm^2) and laser spot radius (from 21.2 μm to 83.0 μm) are shown as a function of inter-pulse distance. Our simulation results at each value of the laser fluence were in good agreement with the ablation rate measurements. The experimental data points can be well described by the modelling curves that take into account the incubation effect and saturation of ablation depth for multi-pulse irradiation. At a low scan speed $v < 100$ mm/s, a high number of pulses per spot is achieved because of the high pulse overlap. Therefore, the ablation threshold decreases drastically, and its related total ablated depth increases. However, the saturation of ablation depth is achieved, and the ablated depth is not increased any more. The ablation rate reaches moderate values and decreases even more by reducing the scanning speed. Meanwhile, with high scanning speed $v > 280$ mm/s, the number of laser pulses per spot becomes small because of the low pulse overlap. Therefore, the ablation threshold increases due to the minor accumulation effect and it causes a small ablation depth. Contrary, the large ablated transverse area for a single pulse is caused by a large inter-pulse distance. The product of a small total ablation depth and large transverse area gives only moderate ablation rate.

For a small laser spot sizes $w_0 < 40$ μm, the laser fluence high above the ablation threshold is achieved, which should result in large ablation depths. However, low numbers of pulses per spot are achieved even for small inter-

pulse distances. Therefore, low ablation rates are achieved because of high ablation thresholds. For high laser spot sizes $w_0 > 75$ μm, it is difficult to reach fluence above the ablation threshold, so low ablation depths are achieved, as well. However, the number of laser pulses is sufficiently high even for large scanning speed because of the high pulse overlap. Thus, low and moderate ablation rates are achieved.

The optimal laser parameter set exists for maximum available ablation rate: scanning speed 180 mm/s $< v < 220$ mm/s and beam spot radius 60 μm $< w_0 < 70$ μm (Fig. 28). In the optimal set up the maximal ablated volume per pulse is reached because of a combination of all the factors influencing material removal rate. The moderate scanning speeds and its related distance between adjacent pulses give sufficiently large transverse ablation area for a single pulse. Also, the moderated spot size gives the sufficiently high number of laser pulses and its related appreciable decrease of ablation threshold due to the accumulation effects. Volume pulses per unit point are less, so the result is a high ablation threshold, which decreases increasing the number of pulses. The saturation depth is just reached in this processing region. Therefore, the ablation rate has a maximum at scanning speed of $v_{max} \approx 200$ mm/s and a laser spot radius of $w_{0\,max} \approx 62.4$ μm (Fig. 28). The experiment data results have a good agreement with the numerical calculation results of the proposed model.

By having laser pulse energy $E_p = 130$ μJ and spot radius $w_0 = 62.4$ μm the calculated peak laser fluence is $F_0 = 2.13$ J/cm^2. By solving Eq. (27) and (28) using optimal inter-pulse distances between scanned spots and scanned lines of $\Delta x = \Delta y = 2.0$ μm, one can calculate the cut-off radius $r_c \approx 62.7$ μm and a number of pulses per spot $N \approx 2500$ pulses. The threshold for that number of pulses by Eq. (10) and accumulation coefficient of $S = 0.70$ is $F_{th}(2500) = 0.28$ J/cm^2. The ratio between the optimal laser fluence and the threshold is 7.6. This number is close to $e^2 \approx 7.4$ which is theoretically predicted [33,34].
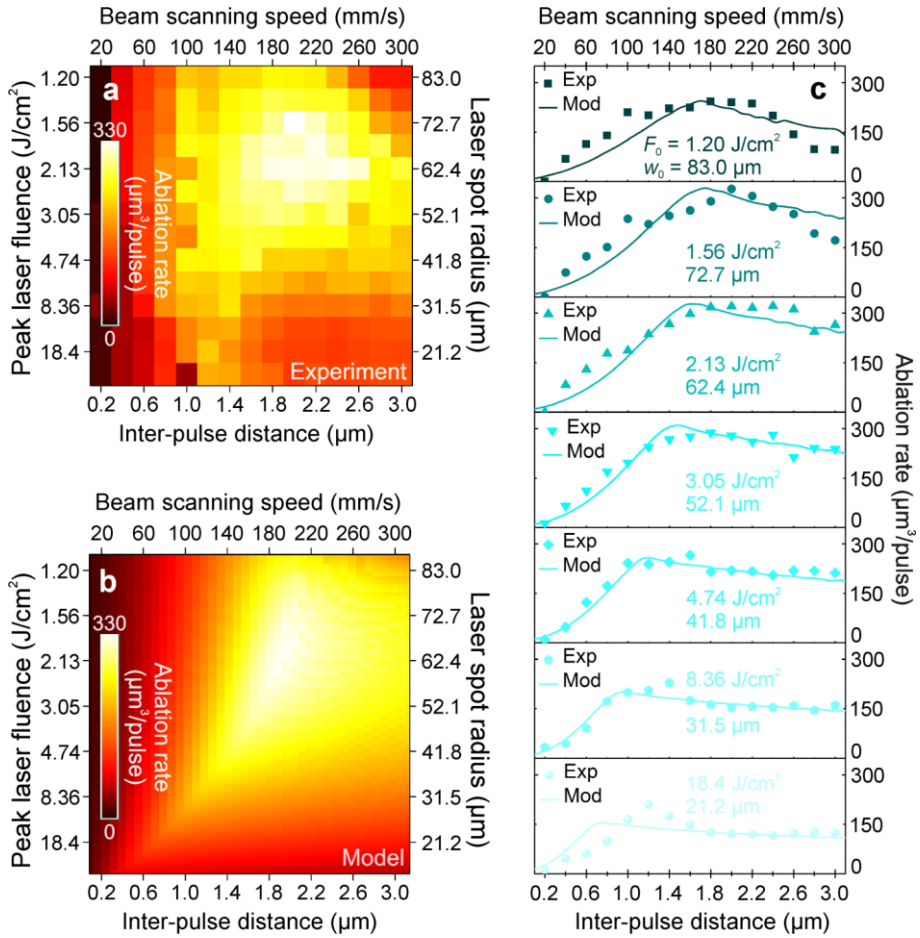
Fig. 28 Comparison of the experimental data to the theoretical model. Laser ablation rate (colour scale) of the copper dependence on the peak laser fluence (left axis), laser spot radius (right axis), inter-pulse distance (bottom axis), and the beam scanning speed (top axis): (a) data from the experiment; (b) results from the proposed rectangular-shaped cavity ablation model; (c) the ablation rate dependence on the inter-pulse distance (bottom axis) and the beam scanning speed (top axis) at different peak laser fluences ranging from 1.20 J/cm² (top) to 18.4 J/cm² (bottom) and laser spot radiuses ranging from 21.2 μm to 83.0 μm. Experimental data points (solid dots) are quantitatively compared with the predictions of our theoretical model (solid lines). Laser parameters: pulse duration 10 ps; wavelength 1064 nm; pulse energy 130 μJ; pulse repetition rate 100 kHz; average laser power 13.0 W.

3.3 Summary

We have demonstrated that the optimum fluence point for the highest ablation efficiency of the picosecond laser could be found by two introduced methods. Fluence optimisation by pulse energy variation showed that laser power has to be limited if the highest ablation efficiency is desired. To

overcome the limitations of the laser power, beam size optimisation should be used. In this case, the ablation rate and efficiency are enhanced simultaneously. It was shown that optimisation of ablation efficiency automatically optimises the quality of the processed surface. This is very important since both of the most crucial technological characteristics are enhanced together. The maximum ablation efficiency depended on pitch distance with the clear peak at $\Delta x = 0.1$ µm.

In this research, the complete model of laser ablation incorporating the accumulation effect and the saturation of ablation depth, if many pulses are applied to a single spot, was presented. The processing parameters: scanning speed (inter-pulse distance), distance between scanned lines and spot size on the sample (peak laser fluence) has been varied in order to reach maximum removal rate. The model assumes that laser beam has a Gaussian intensity profile, the ablation depth per pulse is proportional to the logarithm of fluence applied with a certain ablation threshold, the beam is scanned on a flat target material surface by parallel overlapping lines, the inter-pulse distance is equal to the distance between scanned lines, and the ablation volume per pulse is calculated by summing ablated depths from surrounding pulses within cut-off radius. The experiments have been conducted for the ablation rate measurements and confirmation of modelling results. The experimental evidence of the model is clearly seen in Fig. 28 as the numerical simulation of the model equations is in good agreement with experimental results. Thus, the modelling results are confirmed by the experimental data. The maximum removal rate of 2.0 mm^3/min (330 µm^3/pulse) and maximum ablation efficiency of 2.5 µm^3/µJ has been achieved for the copper target by using the laser processing parameters: wavelength of irradiation 1064 nm; average optical power 13.0 W; pulse repetition rate 100 kHz; pulse duration 10 ps; inter-pulse distance 2.0 µm (scanning speed 200 mm/s); peak laser fluence 2.13 J/cm^2 (spot radius $w_0 = 62.4$ µm). From a scientific point of view, it is worth mentioning that the incorporation of the accumulation effect and saturation of ablation depth for multi-pulse ablation to laser ablation model has been demonstrated for the first time. Comparing our model to previous attempts at predicting the efficient ablation point, where only logarithm dependence on the fluence of ablation depth and diameter squared for ablation by Gaussian beam has been included, our model is much more complete. From an engineering point of view, it is essential to have a theoretical tool and laser scanning procedure to find the most efficient ablation spot. In this work, theoretical model and laser scanning procedure are presented enabling high texturing speed.

4. BURSTS FOR EFFICIENT ABLATION

4.1 High-power MHz burst ablation

The results published in papers [A3] and [A8] are presented in this section. The high scientific interest in the laser pulses in bursts encouraged us to investigate the possible benefits of bursts for ablation efficiency. Previously accumulated knowledge of beam size optimisation method led us to the objective comparison of MHz burst with single-pulse processing and record high ablation efficiencies at the time of paper [A3] release.

4.1.1   Optimisation by temporal pulse division

A solid-state laser (Carbide, Light Conversion) with a variable pulse duration in the range of 210 fs – 10 ps and radiating at the light wavelength of $\lambda = 1030$ nm was used in the experiments. The laser had a possibility to emit a burst of a certain number of pulses from 1 (single pulse regime) to 40. The intra-burst pulse repetition rate was 64.5 MHz, corresponding to the time distance between sequential pulses of 15.5 ns (Fig. 29 a). The burst repetition rate was always fixed at 300 kHz. Maximum average optical power on the sample surface was 36 W and was always fixed during experiments. Rectangular cavities with dimensions of 2×1 mm^2 were engraved into a copper target. Multiple layer scanning was applied to increase the depth and measurement accuracy of cavities profiles. The largest cavity depth reached < 80 µm. Cavity depth never exceeded the Rayleigh length of the laser beam. A linear dependence of the cavity depth versus the number of pulses applied was maintained during the experiment. Therefore, the ablation saturation effects were completely avoided, and reliable data were collected for all investigated regimes. The beam scanning speed of 1 m/s and the distance between scanned lines (hatch) of 10 µm were always constant.

To find the real advantage of the burst regime, the beam size optimisation was introduced for each experiment with various numbers of pulses per burst. The ablation efficiency has maxima at specific peak pulse fluence values. Experimentally it was found that the fluence values were dependent on the pulse number in the burst, but the pulse duration effect was less pronounced (Fig. 29 b, c). In the case of 10 ps pulse duration and single-pulse processing, beam radius enlargement from 26 µm to 35 µm (fluence reduction from 11.2 J/cm^2 to 6.3 J/cm^2) resulted in ablation rate and ablation efficiency increase by 50% (Fig. 29 c). The highest efficiency was measured for 3 pulses in the burst for all pulse durations. The increase in ablation efficiency

compared with the single-pulse regime was from 11% to 20%, depending on the laser pulse duration used in the experiments.
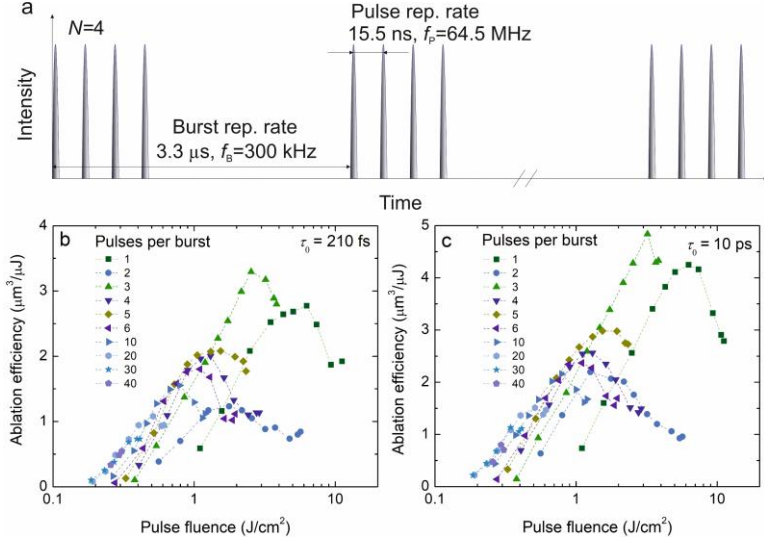

Fig. 29 (a) Schematic example of laser burst regime with 4 pulses per burst, the burst repetition rate of 300 kHz and intra-burst (pulse) repetition rate of 64.5 MHz. Ablation efficiency versus peak pulse fluence for a different number of pulses per burst and two pulse durations of (b) 210 fs and (c) 10 ps. Pulse fluence was varied by increasing the beam size. The laser wavelength $\lambda = 1030$ nm, burst repetition rate $f_B = 300$ kHz, intra-burst repetition rate $f_P = 64.5$ MHz, beam scanning speed $v = 1$ m/s, hatch $\Delta y = 10\ \mu$m.

The maximum ablation efficiencies at the optimum fluences were extracted from Fig. 29 and plotted versus the number of pulses in the burst (Fig. 30). The maximum ablation efficiency decreased sharply when 2 pulses in the burst were used, then suddenly grown up and exceeded the value of the single-pulse regime for 3 pulses per burst (Fig. 30 a). For 4 pulses per burst, the maximum efficiency decreased again, for 5 pulses – marginally increased, later it decreased gradually. This behaviour was observed for all tested pulse durations. The explanation of the efficiency decrease for 2 pulses per burst and increase for 3 pulses per burst is discussed in [37]. The time interval after the first pulse hit the target material is as long as 15.5 ns and is not sufficient for ejected particles to fly away from the interaction area. As shown by the molecular dynamics simulation, particles ejected during laser ablation can move at ~2 km/s speed [21], which results in a 31 μm distance after 15.5 ns. Therefore, the second pulse is attenuated by particle plume. Also, ablation products made by the first pulse are forced by the second pulse to be redeposited back on substrate [74], which could lead to low ablation efficiency by the second laser pulse. Redeposited hot particles contribute to the ablation

efficiency increase as hot material has a higher absorptance [78]. The calorimetric measurement for copper showed that absorptance for 3 pulses per burst is almost twice as high as a one for the single pulse regime [40]. Also, the higher temperature of the interaction area might improve the ablation efficiency as the energy required to evaporate the material by the third pulse is lower. The advantage of using the burst regime in the case of ablation efficiency was only visible for the regime with 3 pulses in the burst. For all other pulse numbers in the burst, the efficiency was lower compared to the single-pulse regime. The highest efficiency for 3 pulses burst and single-pulse regime was at beam radius of $w = 28.3\ \mu m$ and $w = 34.5\ \mu m$, respectively. Therefore, 3 pulse burst regime in addition to the increased efficiency enhanced the laser processing resolution, which is defined by spot size.

The increase in the maximum ablation efficiency at longer pulse durations was observed for all number of pulses in the burst (Fig. 30 b). For 3 pulses per burst, the maximum ablation efficiency was 32% higher at the 10 ps pulse duration compared to 210 fs.
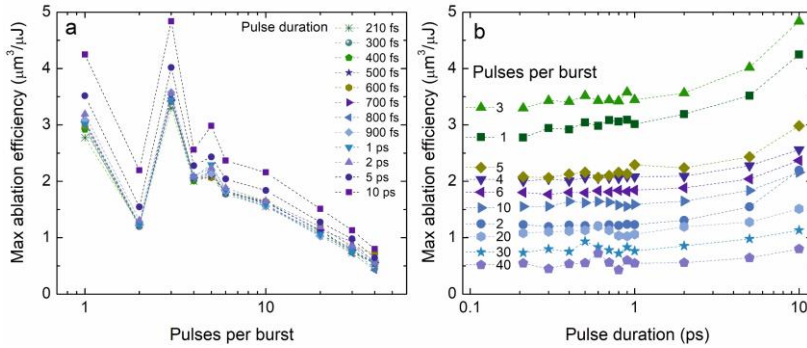

Fig. 30 (a) Maximum ablation efficiency versus the pulse number in the burst for different pulse durations. (b) The maximum ablation efficiency for different numbers of pulses per burst versus pulse duration. Data are extracted from the beam size optimisation experiments (Fig. 29) The laser wavelength $\lambda = 1030$ nm, burst repetition rate $f_B = 300$ kHz, intra-burst repetition rate $f_P = 64.5$ MHz, beam scanning speed $v = 1$ m/s, hatch $\Delta y = 10\ \mu m$.

The highest ablation efficiency of $4.8\ \mu m^3/\mu J$ and ablation rate of $10.5\ mm^3/min$ was reached in this work for 3 pulses per burst and 10 ps pulse duration regime at the 120 µJ burst energy. To our best knowledge, this was the highest laser milling ablation efficiency obtained for copper material by ultrashort pulse lasers emitting at ~1 µm optical wavelength at the time of paper [A3] publication. The higher ablation efficiency of ~7.6 $\mu m^3/\mu J$ was demonstrated only by punching (ablation of a crater) with the ablation-cooled material removal (burst of pulses $N = 800$, intra-burst repetition rate of

$f_P = 3456$ MHz, burst repetition rate $f_B = 1$ kHz, laser wavelength $\lambda = 1040$ nm, pulse duration of $\tau = 1$ ps [1]. Due to the low burst repetition rate of $f_B = 1$ kHz, the ablation rate was only 0.03 mm³/min. As discussed in [73], the laser milling has lower ablation efficiency compared to the laser punching efficiency of ~10 times due to differences in heat accumulation and melt flow in two machining approaches. The ablation-cooling regime was also investigated for copper with a high-power laser (burst repetition rate of $f_B = 200$ kHz, burst energy $E_B = 93$ µJ). In this case, the ablation rate as high as 6 mm³/min was reached for punching with $N = 560$ pulses in the burst, with $f_P = 1600$ MHz intra-burst repetition rate [178]. However, it was still 40% lower than the ablation rate for laser milling achieved in our study. In paper [179], the punching-mode processing in the burst regime was utilised for copper and efficiency reached ~3.2 µm³/µJ by $N = 5$, $f_B = 50$ MHz, $\lambda = 1064$ nm, $\tau = 10$ ps. A lot of work in the pulse energy optimisation for bursts was done by Neuenschwander *et al.*, who found the maximum milling ablation efficiency for copper of 2.6 µm³/µJ [37,39,59] or 2.9 µm³/µJ [38] for $\lambda = 1064$ nm and $\lambda = 1030$ nm which is more than 40% lower than the ablation efficiency achieved in our study.

4.1.2 Surface roughness

The lowest surface roughness of the cavity was measured in the same range of pulse fluences (1 – 3 J/cm²) as the highest ablation efficiency (Fig. 31). This means that two highly important micro-machining characteristics: the ablation efficiency and surface quality can be optimised simultaneously. In addition, for the single-pulse regime, the surface roughness was always higher compared to the burst mode – another advantage of the burst regime.
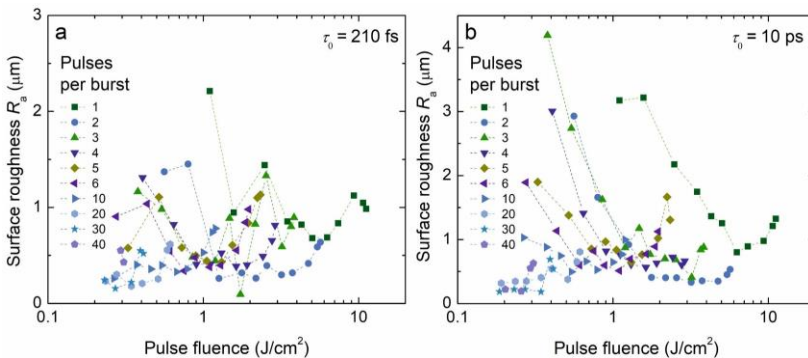

Fig. 31 The surface roughness of the bottom of the laser-ablated cavity versus peak pulse fluence for a various number of pulses per burst and two pulse durations: (a) 210 fs and (b) 10 ps. The laser wavelength $\lambda = 1030$ nm, burst repetition rate $f_B = 300$ kHz, intra-burst repetition rate $f_P = 64.5$ MHz, beam scanning speed $v = 1$ m/s, hatch $\Delta y = 10$ µm.

The surface roughness at the optimum laser fluence F_{opt} for the highest ablation efficiency was extracted from Fig. 31 and plotted versus the number of pulses per burst (Fig. 32). The low surface roughness for even number of pulses per burst could be explained by the redeposition of molten material back on the ablated surface creating a smoothing effect.
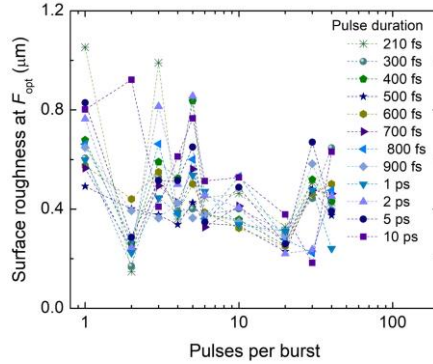

Fig. 32 Surface roughness at the optimum fluence for the highest ablation efficiency versus the number of pulses per burst and various pulse durations. The laser wavelength $\lambda = 1030$ nm, burst repetition rate $f_B = 300$ kHz, intra-burst repetition rate $f_P = 64.5$ MHz, beam scanning speed $v = 1$ m/s, hatch $\Delta y = 10$ μm.

Experiments to see how the surface roughness depends on beam scanning speed were carried out. Five scanning speeds from 1 m/s to 5 m/s were tested for two burst fluences of 7.6 J/cm^2 ($w_0 = 28.3$ μm) and 9.6 J/cm^2 ($w_0 = 31.8$ μm) (Fig. 33). These fluences yielded the highest ablation efficiency for 3 pulses per burst processing. The number of scans was varied to maintain the same accumulated energy per rectangular cavity. For scanning speed of 1 m/s, the scanning repetitions were 2, for 5 m/s – 10 scans and so on. The depths of the cavities were in the range of from 20 μm to 25 μm, highest for the lowest scanning speed and vice versa. The crucial parameter for surface roughness revealed to be the depth removed per one scan. For the highest scanning speed, the depth per layer was lowest. Therefore, it can be assumed that the surface roughness is highly dependent on depth removed per one layer scan.
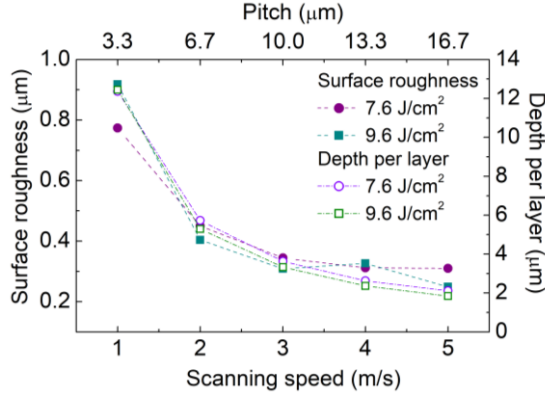
Fig. 33 The surface roughness of the bottom of the ablated cavities versus scanning speed for two burst fluences of $F_B = 7.6$ J/cm^2 ($w_0 = 28.3$ µm) and $F_B = 9.6$ J/cm^2 ($w_0 = 31.8$ µm). The burst fluence corresponds to the total laser energy within burst per area. Burst energy $E_B = 120$ µJ, burst repetition rate $f_B = 300$ kHz, intra-burst repetition rate $f_P = 64.5$ MHz, wavelength $\lambda = 1030$ nm, 3 pulse burst, pulse duration $\tau = 210$ fs, hatch $\Delta y = 10$ µm.

4.2 Ablation by bibursts in the MHz and GHz repetition rates

The results published in paper [A1] are presented in this section. The open questions about GHz burst processing, impact of processing approach (drilling and milling) led us to the investigation in which newly build state-of-the-art laser technology from Light Conversion, capable to produce MHz and GHz bursts in the so called biburst mode, was utilised. Our paper was a pioneering work for biburst efficient ablation.

4.2.1   Single-pulse and MHz burst

A solid-state laser (Pharos, Light Conversion) capable of producing light pulses of $\tau = 210$ fs duration at $\lambda = 1030$ nm wavelength was used in the experiments. The cutting edge laser had 4 working regimes (Fig. 19 b):

1) The conventional single-pulse regime – emitting one pulse every $\Delta t_P = 10$ µs which corresponds to a pulse repetition rate of $f_P = 100$ kHz;

2) MHz burst – emitting burst of pulses with an intra-burst repetition rate of $f_{MHz} = 64.68$ MHz (intra-burst delay time $\Delta t_P = 15.45$ ns) with the number of pulses within the burst ranging from $N = 2$ to $N = 9$ with an inter-burst repetition rate of $f_B = 100$ kHz (inter-burst delay time $\Delta t_B = 10$ µs);

3) GHz burst – emitting burst of pulses with an intra-burst repetition rate of $f_{GHz} = 4.88$ GHz (intra-burst delay time $\Delta t_P = 205$ ps) with the number of pulses within the burst ranging from $P = 2$ to $P = 25$ with an inter-burst repetition rate of $f_B = 100$ kHz (inter-burst delay time $\Delta t_B = 10$ µs);

4) Biburst – tuneable GHz and MHz burst with burst-in-burst regime, where a sequence of P burst pulses at 4.88 GHz is repeated for N times at 64.5 MHz. All combinations of $N = (2, 3, 4, …, 9)$ and $P = (2, 3, 4, …, 25)$ values were possible. In total 192 combinations were theoretically possible for biburst irradiation mode.

Beam size optimisation method was applied for various pulse numbers per burst for drilling of craters and milling of rectangular cavities. All the ablation efficiency versus pulse fluence graphs were either fitted by Eq. (15) coupled with Eq. (11) and depicted by solid lines or data points connected by straight dashed lines for eye guiding purposes (Fig. 34). The Eq. (15) does not take into account heat accumulation or plasma shielding which is usually present during high pulse repetition rate processing. Also, Eq. (15) is considered to be for the ideal case of laser processing, where every laser pulse removes the same amount of material without any perturbations. Laser milling due to the multi-pulse (hundreds and thousands of irradiation events per spot size) ablation statistically is more similar to the ideal laser processing than laser drilling (10 irradiation events on one spot). That is why not all experimental data was successfully fitted by Eq. (15) in Fig. 34 a, b.
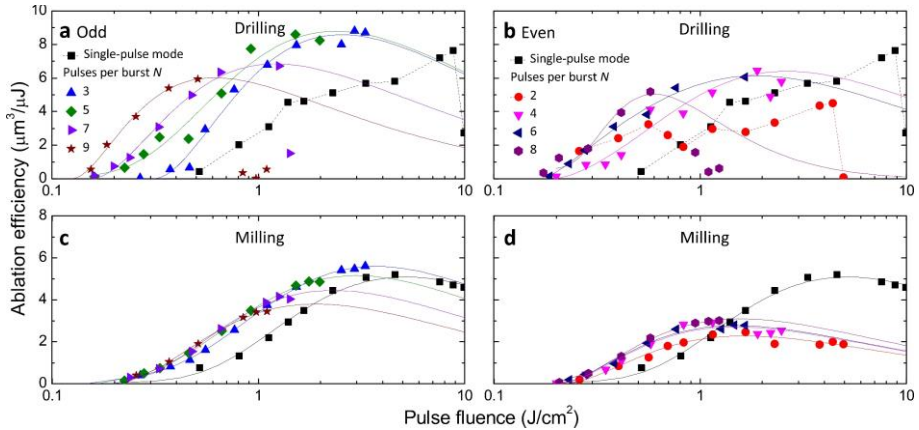
Fig. 34 Crater drilling and cavity milling efficiencies by MHz bursts for copper sample. (a, b) Crater drilling, (c, d) cavity milling. (a) and (c) data for odd number of pulses per burst N, (b) and (d) – even N values. Black squares are efficiencies for conventional single-pulse laser processing with pulse repetition rate of $f_P = 100$ kHz. The laser wavelength was $\lambda = 1030$ nm, burst repetition rate $f_B = 100$ kHz, intra-burst repetition rate $f_{MHz} = 64.68$ MHz, average optical power $P_{ave} = 7.3$ W.

In the case of MHz burst processing of copper, the strong dependence of odd and even number of pulses per burst was clearly visible for both crater drilling and cavity milling (Fig. 34). By using MHz burst the highest ablation efficiency for crater drilling was 8.8 $\mu m^3/\mu J$ for $N = 3$ pulses per burst and was

higher than single-pulse regime efficiency by 15%. Also, $N = 5$ pulses per burst had a higher crater ablation efficiency by 12.5% compared to single-pulse regime. All other N values were less efficient than the conventional single-pulse regime. For cavity milling, the highest ablation efficiency was 5.6 $\mu m^3/\mu J$ for $N = 3$ pulses per burst and was higher than single-pulse regime efficiency by 8%. Similarly, the 3-pulses MHz burst processing was the most efficient regime for pulse-energy-optimisation [78] and beam-size-optimisation [A3] (Section 4.1 High-power MHz burst ablation) for milling, but was never reported for drilling.

The clear ablation efficiency dependence on number of pulses per burst and processing approach is shown in Fig. 35 c. For both crater drilling and cavity milling two laser-initiated processes interchangeably play an important role: one responsible for the reduction of the ablation efficiency at even-pulses burst and the second – for the increase at odd-pulses burst. The process responsible for the reduction of the ablation efficiency is shielding of the second pulse by the plume of ablated particles [74] and plasma [75] produced by the first pulse. Depending on the laser fluence the plume consists of fast atoms and slower nanoparticles [180]. The theoretical studies showed that the depth of the ablated crater by double-pulse configuration is lower than the one for single-pulse ablation [181,182]. This is the consequence of the absorption of the second pulse in the nascent ablation plume, which results in the reheating of ablated material and acceleration of outward part of the plume and deceleration of the inner part of the plume. The similar findings were observed by optical shadowgraphy experiments [74]. The second pulse hits the ablation cloud, the vaporisation of droplets and re-ignition of plasma starts. Due to the second pulse-ablation cloud interaction-induced pressure, part of the material from the ablation cloud might be forced to redeposit back on the target, as a consequence the shielding plume is dispersed [74]. The atomistic simulation of double-pulse ablation confirms the redeposition of material [76]. Also, the measurements by high-precision balances show thrust enhancement for double-pulses with a delay time of 12.2 ns, suggesting the redeposition of material [77].

The third pulse interacts with the target material pre-heated by the redeposited material and does not suffer the plume attenuation. Therefore, the ablation efficiency is increased as hot material has a higher absorptance [78] and the energy required to raise the temperature to the boiling point of the pre-heated material is lower. The higher volume of the material is ejected by the third pulse, which again creates the ablation plume and all the processes repeat again, resulting in periodical decrease-and-increase in ablation efficiency for the odd and even number of pulses per burst (Fig. 35 c). This triangle-wave-

type dependency was material and intra-burst repetition rate dependent, since it was measured only for copper at MHz burst and biburst, but not for GHz burst (Fig. 36 a and Fig. 38 a). Triangle-wave-type dependencies versus number of pulses per burst for copper drilling and milling measured by two completely different processing approaches coincide perfectly, proving that the efficiency measurements are accurate and reliable. The curve of maximum efficiency for drilling was shifted upwards by ~1.5 – 2 times depending on the number of pulses per burst. Similar ~1.5 times more efficient drilling than milling was registered in ref [64]. During burst processing part of the irradiated matter is melted [68]. In the case of crater ablation, some of the matter is removed in liquid form and is seen as burr around the hole. In addition, it is commonly known that after fs laser ablation the condensed particles are found on the workpiece around the processed area as debris. In the case of milling, scanned laser beam interacts multiple time with this burr and debris, therefore energy is consumed to re-heat and evaporate the previously effected matter, that is why the measured efficiency of crater drilling is higher than efficiency of milling [64].

For the steel sample the influence of odd-pulses and even-pulses bursts on ablation efficiency was not observed (Fig. 35 a, b). The highest ablation efficiency was measured for the single-pulse processing mode and was 6.9 $\mu m^3/\mu J$. The MHz burst was more efficient than the single-pulse regime only for pulse fluence values higher than ~2 J/cm^2. This can be explained by dense plasma/particle generation at high fluencies. Also, at higher fluence the beam spot size is smaller, as a result the shielding effect is stronger. Therefore, the ablation efficiency close to ~0 $\mu m^3/\mu J$ was measured for single-pulse mode and pulse fluence near ~10 J/cm^2. The maximum ablation efficiency of steel dropped down by 35% for 2-pulses burst and 56% for 3-pulses burst compared with single-pulse processing (Fig. 35 d). For 4-pulses burst efficiency increased and stabilised at 5-pulses burst, but was still about 28% lower than single-pulse efficiency.
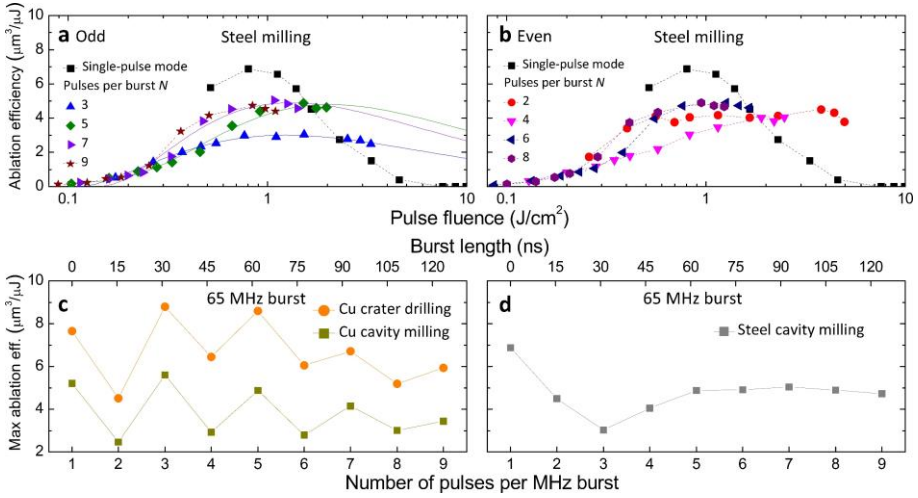
Fig. 35 Cavity milling efficiencies of MHz bursts for steel sample for (a) odd and (b) even number of pulses per MHz burst. Black squares are efficiencies for conventional single-pulse laser processing with pulse repetition rate of f_P = 100 kHz. (c) Maximum ablation efficiencies extracted from Fig. 34 versus number of pulses per MHz burst for drilling and milling of copper. (d) Maximum ablation efficiencies extracted from (a) and (b) versus number of pulses per MHz burst for milling of stainless steel. The laser wavelength was λ = 1030 nm, burst repetition rate f_B = 100 kHz, intra-burst repetition rate f_{MHz} = 64.68 MHz, average optical power P_{ave} = 7.3 W.

4.2.2   GHz burst

The beam-size-optimisation was applied for GHz burst processing (Fig. 36). The ablation efficiency for copper milling decreased by 78% for P = 2 pulses burst and ~90% for P = 3 and up to P = 25 number of pulses per burst compared to single-pulse milling (5.2 µm³/µJ) regime (Fig. 36 a). The similar ablation efficiency decrease was measured for steel milling: for P = 2-pulses burst efficiency decreased by 78%, for P = 3 and more pulses per burst – by 88% – 94% compared to single-pulse milling (6.9 µm³/µJ) regime (Fig. 36 c). For GHz burst copper drilling the efficiency was also significantly reduced by 79% – 86% depending on the number of pulses per burst compared to the single-pulse drilling (7.7 µm³/µJ) (Fig. 36 b). The maximum efficiency values were extracted from Fig. 36 a – c and plotted in Fig. 36 d. The difference between copper drilling and milling was similar to the one measured for MHz burst – depending on the number of pulses per burst drilling was ~1.4 – 2.9 times more efficient than milling. The milling of copper and milling of steel had similar maximum ablation efficiency values versus number of pulses per GHz burst. The high efficiency decrease for GHz burst compared with single-pulse processing was due to the ultrafast laser-matter interaction induced plasma and particle shielding, which partially blocked the incoming laser

71

pulses. In the case of 2-pulses burst processing, 205 ps distance between two pulses was not short enough to prevent attenuation of the second pulse by plasma/particles generated by the first pulse [183].
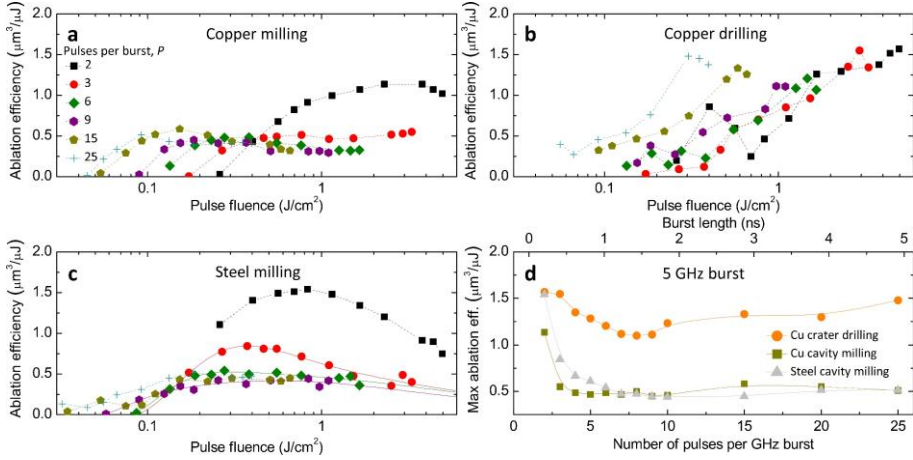

Fig. 36 Ablation efficiencies of GHz bursts for (a) copper cavity milling, (b) copper crater drilling and (c) steel cavity milling. (d) Maximum ablation efficiencies extracted from (a), (b), (c) versus number of pulses per MHz burst for milling and drilling of copper and milling of steel. The laser wavelength was $\lambda = 1030$ nm, burst repetition rate $f_B = 100$ kHz, intra-burst repetition rate $f_{GHz} = 4.88$ GHz, average optical power $P_{ave} = 7.3$ W.

4.2.3 Biburst

The beam-size-optimisation was applied for biburst processing. Some of the measurement data are presented in Fig. 37, the rest of the data can be found in the supplementary material of [A1] paper. In the case of copper and steel biburst milling, the ablation efficiency values were not much different from the GHz burst milling being, at the best, about three times less efficient than single-pulse milling. The unexpected high ablation efficiency values were measured for copper biburst drilling, which at the certain number of pulses per burst combination, exceeded the value of the single-pulse drilling. Nevertheless, the MHz burst drilling was still more efficient than biburst drilling. The difference of biburst drilling and milling efficiencies was huge: for example, for the processing regime $N = 5$, $P = 25$, copper drilling had the efficiency more than 12 times higher than milling (Fig. 37 a, b). Similarly, the high difference between the efficiencies of milling and drilling of ~10 times was measured for 160-pulse 864 MHz burst and was explained by the different melt flow [73]. In the drilling procedure heat accumulation-induced melt is ejected out of the crater due to the recoil vapour pressure, while during the

milling procedure, melt flows back on the previously processed area and does not contribute to the material removal.
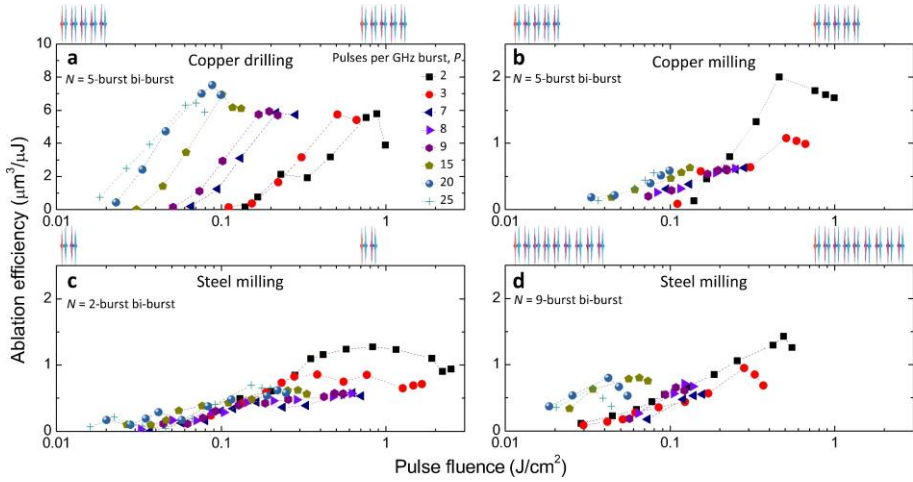
Fig. 37 Ablation efficiencies of bibursts for (a) copper crater drilling by $N = 5$ bursts per biburst, (b) copper cavity milling by $N = 5$ bursts per biburst, (c) steel cavity milling by $N = 2$ bursts per biburst and (d) steel cavity milling by $N = 9$ bursts per biburst. Above each of the graphs, the schemes of biburst configuration depicted with $P = 2$ and corresponding N. The laser wavelength was $\lambda = 1030$ nm, biburst repetition rate $f_B = 100$ kHz, burst repetition rate $f_{MHz} = 64.68$ MHz, pulse repetition rate $f_{GHz} = 4.88$ GHz, average optical power $P_{ave} = 7.3$ W.

The maximum ablation efficiency values were extracted from all the measured ablation efficiency versus pulse fluence graphs (Fig. 38). In the case of copper milling by bibursts, the influence of odd and even number of bursts per biburst N was evident only for $P = 2$ pulses per GHz burst (Fig. 38 a). This triangle-type-wave dependence was similar to the one measured for the MHz burst processing (Fig. 35 c). Contrary, the biburst copper drilling did not have the same shape as MHz burst drilling (Fig. 38 b). The drop of ablation efficiency was not measured for $N = 4$ bursts per biburst, ruining the triangle-type-wave graph as was the case for MHz burst processing. For steel biburst milling the small influence of number of bursts per biburst N for maximum ablation efficiency was measured (Fig. 38 c). The highest ablation efficiencies achieved in this work for each of the processing mode and approach are summarised in Fig. 38 d.
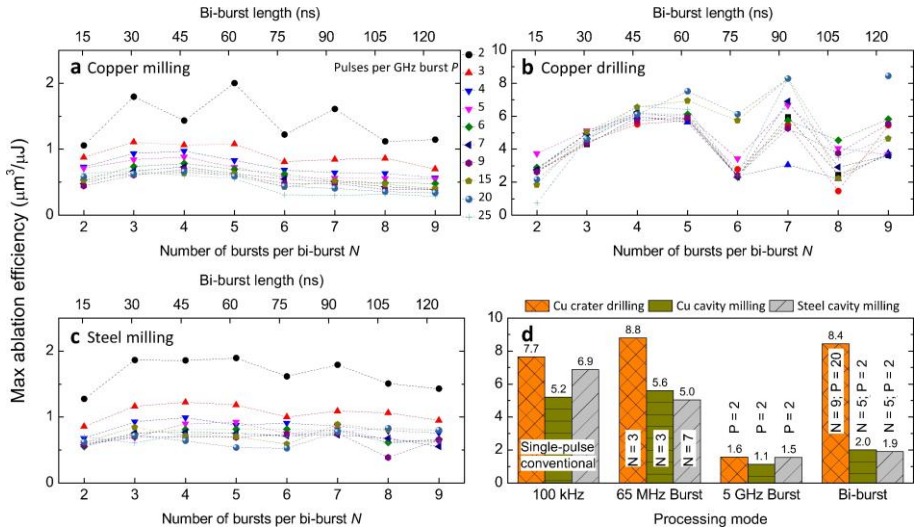
Fig. 38 Maximum ablation efficiencies for biburst (a) copper milling, (b) copper drilling and (c) steel milling. (d) The highest ablation efficiencies of drilling and milling measured for four different processing modes. The laser wavelength was $\lambda = 1030$ nm, burst repetition rate $f_{MHz} = 64.68$ MHz, pulse repetition rate $f_{GHz} = 4.88$ GHz, average optical power $P_{ave} = 7.3$ W.

SEM images and profiles of the most efficient drilling and milling regimes together with surface roughness are presented in Fig. 39. As shown in previous sections (3.1, 4.1) of this dissertation, the ablation efficiency optimisation via beam size also results in high-quality. The smallest surface roughness achieved in this work for cavity milling was as low as $R_a = 0.1$ µm showing the promising utilisation of ultrafast bursts in the polishing [184] and high-quality surface treatment [67] applications.
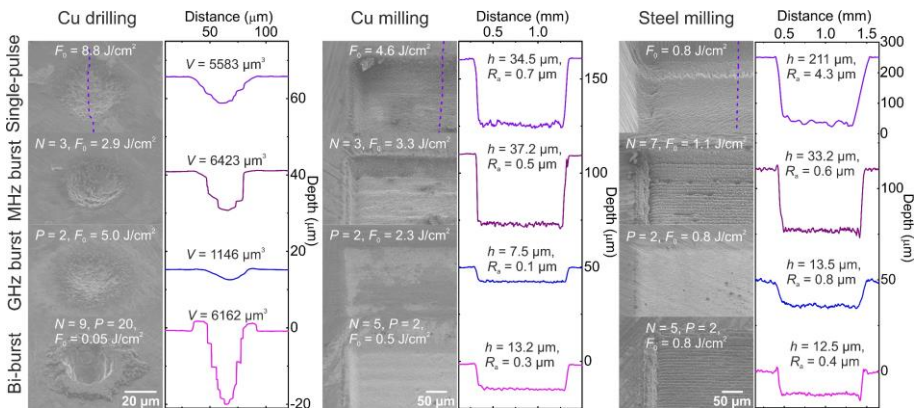
Fig. 39 SEM images and profiles of the most efficient drilling and milling regimes for various processing modes. V – volume of the crater, h – depth of the cavity, R_a – surface roughness, F_0 – pulse fluence, N and P – number of pulses per MHz and GHz burst, respectively.

Overall, the highest ablation efficiency values for copper were measured for MHz burst processing and $N =3$ pulses per burst and was 8.8 µm^3/µJ for drilling and 5.6 µm^3/µJ for milling, while the steel milling efficiency was highest for a conventional single-pulse regime with 6.9 µm^3/µJ. At the time of paper [A1] release these ablation efficiency values were highest for ultrashort pulses at ~1 µm wavelength. The previous highest ablation efficiency values were 7.6 µm^3/µJ for copper drilling [1], 4.8 µm^3/µJ for copper milling [A3] and 4.1 µm^3/µJ for steel milling [68]. For more information about the processing parameters utilised in other studies and typical efficiency values see Table 3.

Table 3. Typical ablation efficiency values reported in the literature. f_P – intra-burst repetition rate, N – number of pulses per burst, λ – laser wavelength, τ_p – pulse duration, w_0 – beam radius, f – pulse or burst repetition rate, v – beam scanning speed, Δy – hatch distance.

	Copper				Stainless steel	
	Drilling (µm³/µJ)	$f_P, N, \lambda, \tau_p, w_0, f$	Milling (µm³/µJ)	$f_P, N, \lambda, \tau_p, w_0, f, v, \Delta y$	Milling (µm³/µJ)	$f_B, N, \lambda, \tau_p, w_0, f, v, \Delta y$
Burst	7.6 [1]	3.456 GHz, 800 ppb, 1035 nm, 1 ps, 12 µm, 1 kHz	2.6 [37]	83 MHz, 3 ppb, 1064 nm, 10 ps, 16 µm, 200 kHz, 1.6 m/s, 8 µm	2.3 [37]	83 MHz, 3 ppb, 1064 nm, 10 ps, 16 µm, 200 kHz, 1.6 m/s, 8 µm
	6.5 [178]	1.6 GHz, 400 ppb, 1050 nm, 300 fs, 11.5 µm, 200 kHz	4.2 [68]	148 MHz, 28 ppb, 1040 nm, 380 fs, 9 µm, 100 kHz, 750 mm/s, 7.5 µm	2.5 [68]	148 MHz, 28 ppb, 1040 nm, 380 fs, 9 µm, 100 kHz, 750 mm/s, 7.5 µm
	8.8 [A1]	64.68 MHz, 3 ppb, 1030 nm, 210 fs, 23 µm, 100 kHz	**5.6 [A1]**	64.68 MHz, 3 ppb, 1030 nm, 210 fs, 21.7 µm, 100 kHz, 300 mm/s, 10 µm	**5.0 [A1]**	64.68 MHz, 7 ppb, 1030 nm, 210 fs, 24.8 µm, 100 kHz. 300 mm/s, 10 µm
Single-pulse	0.7 [179]	-, -, 1064 nm, 10 ps, 10 µm, 100 kHz	2.22 [37]	-, -, 1064 nm, 10 ps, 16 µm, 200 kHz – 1.6 MHz, 8 µm	2.25 [37]	-, -, 1064 nm, 10 ps, 16 µm, 200 kHz – 1.6 MHz, 8 µm
	1.9 [185]	-, -, 1064 nm, 10 ps, 31.45 µm, 50 Hz	3.1 [68]	-, -, 1040 nm, 380 fs, 9 µm, 100 kHz, 750 mm/s, 7.5 µm	4.1 [68]	-, -, 1040 nm, 380 fs, 9 µm, 100 kHz, 750 mm/s, 7.5 µm
	7.7 [A1]	-, -, 1030 nm, 210 fs, 23 µm, 100 kHz	**5.2 [A1]**	-, -, 1030 nm, 210 fs, 31.8 µm, 100 kHz, 300 mm/s, 10 µm	**6.9 [A1]**	-, -, 1030 nm, 210 fs, 76 µm, 100 kHz, 300 mm/s, 10 µm

4.3 Summary

Ablation efficiency of copper milling by ultrashort pulses of 10 ps pulse duration and 120 µJ pulse energy was increased by 50% using the beam size optimization technique. Ablation by bursts with 64.5 MHz intra-burst pulse repetition rate revealed that, in the best case, the ablation efficiency could be improved by 20% compared to the single-pulse for the beam-size-optimised regimes if 3-pulse burst is applied. The beam-size-optimised, 3 pulses per burst processing let us reach laser milling ablation efficiency of copper by ultrashort pulses of 4.8 $\mu m^3/\mu J$, which was the highest at the moment of publishing [A3] paper. All other numbers of pulses per burst demonstrated lower ablation efficiency. Another advantage of the burst mode compared to the single-pulse regime ablation was lower surface roughness of the bottom of the ablated cavities. The lowest surface roughness achieved by the single-pulse regime was several times higher than that measured for the burst mode. In the range of pulse duration between 210 fs and 10 ps, the ablation efficiency increased by 32% for longer pulses, and micro-machining quality improved.

The in-depth study of maximum ultrafast laser ablation efficiency for processing of copper and steel by single-pulses, MHz-, GHz- and biburst was performed. In the case of copper MHz burst milling and drilling the ablation efficiency was highly dependent on the odd and even number of pulses per burst. The MHz burst drilling of copper was up to two times more efficient than milling process with the same triangle-type-wave dependence on a number of pulses per burst. This type of dependence was material dependent. Steel MHz burst milling had a completely different tendency with no evidence of odd and even number of pulses per burst influence on the ablation efficiency. The GHz processing was revealed to be highly inefficient for both milling and drilling and both copper and steel compared to single-pulse processing. The biburst milling of copper and steel did not improve the ablation efficiency compared to the single-pulse milling. The biburst drilling efficiency of copper had a higher ablation efficiency than the single-pulse drilling. Three high ablation efficiency values for ultrashort pulse laser processing at ~1 µm wavelength were measured: 8.8 $\mu m^3/\mu J$ for copper drilling, 5.6 $\mu m^3/\mu J$ for copper milling, and 6.9 $\mu m^3/\mu J$ for steel milling.

In conclusion, the usage of bursts of pulses for laser micro processing of copper is advantageous only when 3 pulses per burst are used – the ablation efficiency and quality are increased compared to the single-pulse regime. In addition, the laser processing resolution is enhanced when using bursts due to the smaller spot size required to reach the optimum fluence.

5. LASER FABRICATION OF BIO-INSPIRED SURFACES

5.1 3D laser micro-machining by single-pulse and burst modes

The results published in paper [A3, A5, A7] are presented in this section. The method of 3D subtractive micro-machining by layer-by-layer processing was introduced in paper [A5] and continued with burst mode in [A3]. Examples of bio-inspired surfaces like fish scale [A3] and shark-skin riblets [A7] were fabricated.

5.1.1   Ablation rate and surface roughness

Picosecond laser (Atlantic, Ekspla) with the average optical power of $P = 40$ W and tuneable pulse repetition rate in the range of 404 kHz – 1138 kHz was used for 3D fabrication. The average power of the laser remained approximately constant while the repetition rate was varied. It was found that optimum fluence for the highest ablation efficiency should be about $F_0 = 3$ J/cm^2 (Fig. 21). To reach this value while using all laser power the maximum pulse repetition rate had to be set to lower the pulse energy. Also, an F-theta lens with the focal distance of + 100 mm was used to obtain a larger spot size of approximately $2w_0 = 50$ μm.

The optimisation was dedicated to finding an optimum scanned line distance (hatch) for the highest ablation rate and lowest surface roughness. The lowest surface roughness was at the same two parameters window as the highest ablation rate (Fig. 40 a, b). This relation confirmed that with the highest ablation efficiency the best surface quality is reached. Due to fast beam scanning and sufficient distance between scanned lines the target sample did not reach melting or boiling temperature, therefore good bottom morphology was observed (Fig. 40 c). For the highest ablation rate the optimal hatch and the optimal scanning speed was related (Fig. 40 b). If one was increased, another had to be lowered. The parameters work window, which combines the highest ablation rate and lowest surface roughness, was found.
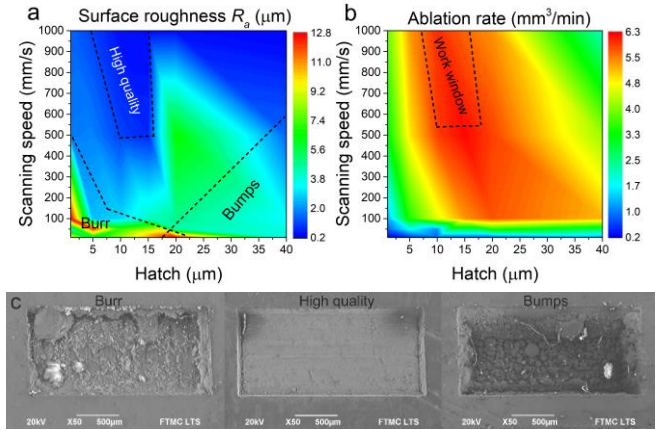
Fig. 40 Influence of beam scanning speed v and hatch Δy to laser ablation process combining both highest ablation rate and lowest surface roughness. (a) Surface roughness after one scan versus v and Δy with quality regions. (b) Ablation rate dependence on v and Δy calculated from multiple scans needed to reach measurable depth. (c) SEM images of quality's regions. *Burr*: $v = 10$ mm/s, $\Delta y = 1$ μm, scans $N = 1$, *High quality*: $v = 1000$ mm/s, $\Delta y = 10$ μm, $N = 10$, *Bumps*: $v = 50$ mm/s, $\Delta y = 20$ μm, $N = 10$. Peak fluence $F_0 = 3.5$ J/cm^2, pulse repetition rate $f = 1138$ kHz, pulse duration $\tau = 10$ ps, laser wavelength $\lambda = 1064$ nm, laser power $P = 40$ W.

5.1.2   3D fabrication examples

Fast 3D micro-machining was realised utilising stereolithographic standard triangle language (STL) files. The subtractive processing is opposite to additive manufacturing technology, where an object is fused from many layers. Laser processing software (DMC, Direct Machining Control) was used to invert and slice 3D drawings into many layers along the *z*-axis. By scanning the laser beam layer-by-layer, the unwanted material was removed starting from the top of the sample. After each slice, beam focal point was shifted down by the corresponding ablation depth per one scan layer. For the example of deep engraving Albert Einstein's bust was engraved into the copper plate (Fig. 41 a, b). The material removal rate of 6 mm^3/min was reached with the average optical power of 40 W. The surface roughness of the flat part was 0.2 μm. The both-sided bust was fabricated by dividing the stereolithographic file into two parts. Further, the front part file was sliced into a certain number of layers to reach desirable depth. After the front part was fabricated, the copper plate was flipped over, and the procedure was repeated to fabricate the back part. For precise positioning of the sample after flipping operation, visual μ-camera (UI-614xSE, uEye) was used. The possibility to fabricate 3D objects by combining a rotary axis with the sample mounted on it, and the galvanometric scanner is also possible. The hexagonal tilted structure mimicking fish scales was created for fluidic drag reduction applications (Fig.

41 c). The laser milling technology allows to fabricate complex parts, however it is limited to fabrication of positively inclined side walls (positive taper angle) [186], similarly to conventional milling technology. However, the tool width, which determines the resolution of the process, for laser milling technology can be significantly reduced compared to computer numerical control (CNC) milling and is restricted to the laser wavelength.
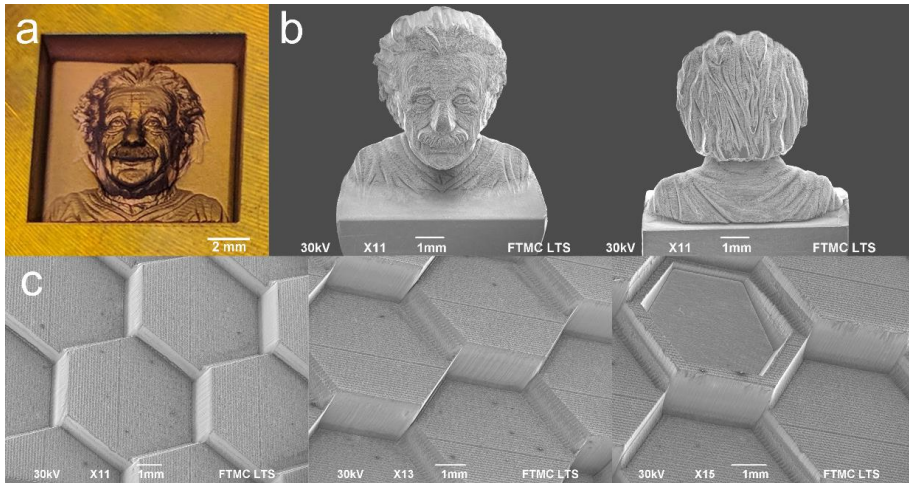
Fig. 41 Examples of 3D laser fabrication. (a) Photo of front part of Albert Einstein's bust engraved into copper dimensions $10 \times 10 \times 2$ mm^3. (b) SEM images of both-sided laser sculptured bust, dimensions $8 \times 8 \times 5$ mm^3 (without pedestal). (c) SEM photographs of fish scale-like structure for fluidic drag reduction applications. The height of scale 2.2 mm, period 6 mm. Ablation rate 6 mm^3/min, peak fluence $F_0 = 3.5$ J/cm^2, pulse repetition rate $f = 1138$ kHz, pulse duration $\tau = 10$ ps, laser wavelength $\lambda = 1064$ nm, laser power $P = 40$ W.

The MHz burst mode micro-machining quality was tested by milling complex 3D cavities, coat of arms of Lithuania was milled in copper plate (Fig. 42 a). The 3D micro-machining was realised using a high-power MHz burst laser (Carbide, Light Conversion) and layer-by-layer removal technique starting from the top of the sample. The most efficient 3 pulses per burst regime was selected, and the pulse duration was set to 10 ps. High-quality complex 3D cavities were laser milled with the ablation rate of 10.5 mm^3/min and surface roughness of $R_a = 0.4$ µm. No side effects or melting was seen for 10 ps pulses. The bottoms of the cavities were smooth, with no bumps or unwanted parasitic structure formation, which could ruin the aesthetic appearance of the cavities (Fig. 42 b, c).
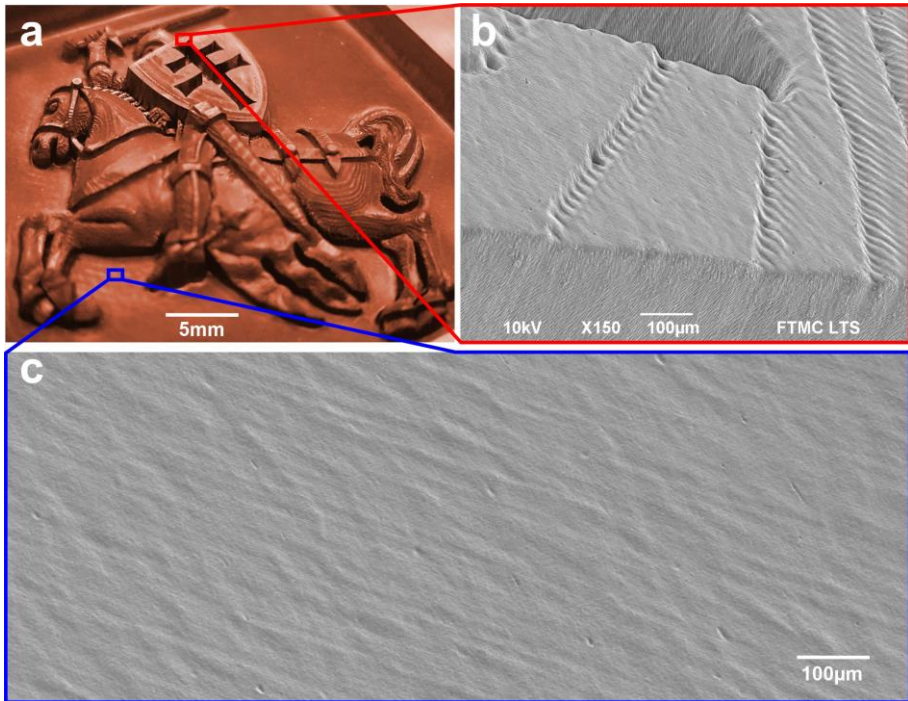
Fig. 42 Example of efficient laser milling. (a) Optical image of the coat of arms of Lithuania milled in copper plate. (b) SEM image of laser milled surface illustrating layer-by-layer removal. (c) SEM image of the bottom surface of the laser-milled cavity. Laser parameters: 3 pulses per burst, laser wavelength $\lambda = 1030$ nm, burst repetition rate $f_B = 300$ kHz, intra-burst repetition rate $f_P = 64.5$ MHz, beam scanning speed $v = 1$ m/s, copper removal rate of 10.5 mm^3/min.

2.5D structure formation and replication of bio-inspired structure in copper at high speed was demonstrated by ultrashort pulse laser (Atlantic, Ekspla) with pulse duration of $\tau = 10$ ps and average power of 13 W. For creation of simple riblets, 2.5D processing (all layers are the same) is sufficient. The examples of deep laser engraving and 2.5D structuring are given in Fig. 43. The laser ablated cavity with the removal rate of 330 μm^3/pulse has been performed by using 130 μJ laser pulse energy. The set of processing parameters for efficient ablation has been used to create a rectangular cavity (Fig. 43 a), the logo of Center for Physical Sciences and Technology (FTMC) (Fig. 43 b), a bio-inspired shark-skin structure (Fig. 43 c) and a drag reducing blade-riblet structure (Fig. 43 d) in the copper sample. The ablation rate of 2.0 mm^3/min has been achieved with an average laser power of 13.0 W.
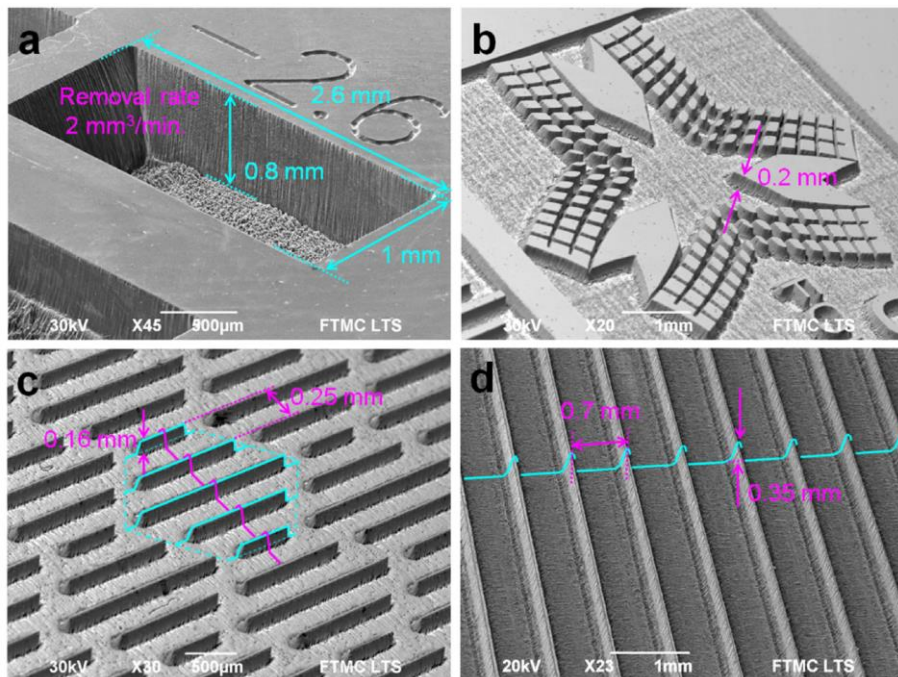
Fig. 43 Examples of efficient surface structuring by laser. SEM images of structures ablated in copper by using a picosecond laser: (a) rectangular cavity with dimensions 2.6 mm × 1.0 mm × 0.8 mm processed in 1 min time; (b) logo of Center for Physical Sciences and Technology, engraving depth 0.2 mm; (c) bio-inspired shark-skin-like structure, period 0.25 mm, blade height 0.16 mm; (d) drag reducing blade-riblet structure: period 0.7 mm; blade height 0.35 mm. Laser processing parameters: wavelength of irradiation 1064 nm; laser power 13.0 W; pulse repetition rate 100 kHz; pulse duration 10 ps; scanning speed 200 mm/s; spot radius $w_0 = 62.4$ μm, peak laser fluence $F_0 = 2.13$ J/cm^2, copper removal rate of 2.0 mm^3/min.

5.2 Fabrication of riblets on cylindrical surface

The results published in paper [A4] are presented in this section. The fabrication of shark-skin-like riblet structures on 3D cylindrical copper surface was realised by 5-axes laser machining system.

5.2.1 Laser processing setup

A solid-state laser (Atlantic, Ekspla) with an average optical power of 50 W at the wavelength of 1064 nm, pulse duration of 10 ps and maximum pulse repetition rate of 1138 kHz was used for the experiments. The beam was focused using a 160 mm focal distance F-theta lens and the beam position in the *x* and *y* directions on the target's surface was controlled by a galvanometric scanner (Intelliscan 14, Scanlab). The cylindrical copper sample was placed in the rotary stage of the 5-axess positioning system (Duo MASTER, Elas)

(Fig. 44 a). Sample positioning in the *X*, *Y* directions was realised by linear stages, rotation in *YZ* and tilt in *XZ* planes by the rotary stages, the focusing of the beam was controlled by *Z* stage on which the galvanometer scanner equipped with the F-theta lens was mounted. From a certain point on the sample, 0.1 mm length lines were scanned forward and backward in *x* direction using the galvanometer scanner while the sample was rotated in the *YZ* plane by the rotary stage – so-called laser turning (Fig. 44 c). Multiple rotations of copper sample while it was ablated were performed in order to receive the desired depth. The number of rotations depended on fluence and pulse repetition rate. At the highest fluences the number of rotations was 10 and increased to 15 as fluence was gradually dropped until around 80% of the maximum fluence value. For the lowest fluences the number of rotations was between 40 and 125 to achieve a similar ablated depth. Laser peak fluence was varied by internal laser attenuator changing the pulse energy, which was done by lowering the average laser power from 50 W to 6 W (step 4 W). The experiment was repeated at different pulse repetition rates of 404 kHz, 602 kHz, 808 kHz and 1138 kHz. The chosen frequencies were restricted by the laser irradiation source. At all of the pulse repetition rates the maximum average power was constant of 50 W. This resulted in different maximum pulse energies and fluences at different frequencies. The pitch on the surface of the target was kept constant (1.8 µm) by proportionally increasing the beam scanning speed at higher pulse repetition rates. For highest pulse repetition rate of 1138 kHz beam scanning speed of 2050 mm/s was used, which was near to the limit of the galvanometer scanner speed. The sample was rotated at a speed of 422 deg/s.
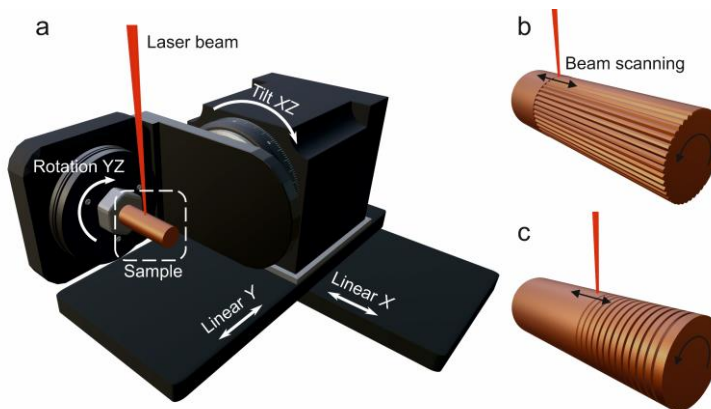

Fig. 44 (a) Laser processing of cylindrical sample and scheme of rotary axes mounted on *XY* linear translational stages for sample positioning. Laser beam was scanned by galvanometric scanner. (b) Laser texturing by longitudinal blade-riblets and (c) laser turning procedures.

For the laser texturing of the cylindrical copper sample by longitudinal blade-riblet structures, numerous adjacent 15 mm length lines were scanned by the galvanometer scanner in x direction on the target's surface, then sample was rotated and procedure repeated multiple times until all cylinder was textured (Fig. 44 b).

5.2.2   Laser texturing

The highest ablation efficiency was in the fluence interval of $4 - 7$ J/cm^2 (Fig. 45 a). Experimental data correlated well with the theoretical model Eq. (15) at low $1 - 10$ J/cm^2 fluences. However, at high $10 - 25$ J/cm^2 fluences experimental data deviated from the Eq. (15) approximation. The drop of the ablation efficiency started earlier for the higher pulse repetition rates. Therefore, the deviation could be explained by the ablated particle shielding, which absorbs, reflects and scatters laser emission [187]. For the higher pulse repetition rate, the time interval between two pulses is shorter and the pulse coming towards the target interact with the particle plume generated by the previous pulse. Also, since the sample is being affected by high power laser emission, its temperature increases and the surface becomes uneven, which also adds to the emission scattering [41]. The highest ablation efficiency range also resulted in the best surface quality in the terms of relative surface roughness. This is very important because efficiency and quality are optimised together. Relative surface roughness was evaluated from the depth profiles and calculated as follows: $R_r = R_a / D_a \times 100\%$, where R_r – is relative roughness, R_a – surface roughness, D_a – cavity depth (Fig. 45 b). The average cavity depth was around 260 μm and the average surface roughness was around 3.6 μm, however in the optimal fluence region it was around 1.1 μm.
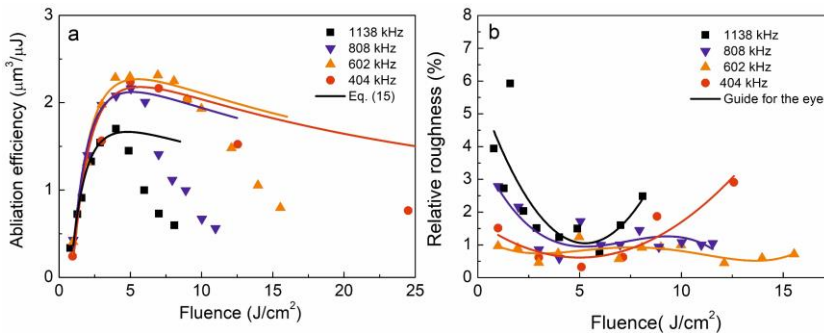
Fig. 45 (a) Ablation efficiency and (b) relative roughness versus fluence for different pulse repetition rates. Laser processing parameters: wavelength 1064 nm, pulse duration 10 ps, beam radius $w_0 = 18$ μm.

Any increase of the laser power (pulse energy) should result in higher ablation rate, which is suggested by Eq. (16). However, a sharp decrease was seen at higher fluences due to the aforementioned particle shielding. The critical fluence, where increase of pulse energy lowers the ablation rate was dependent on pulse repetition rates. For the pulse repetition rate of 1138 kHz the critical fluence was about 5 J/cm^2, for 602 kHz – 10 J/cm^2 and for 404 kHz – 15 J/cm^2. The machined cavity at optimal parameters is shown in Fig. 46 b.
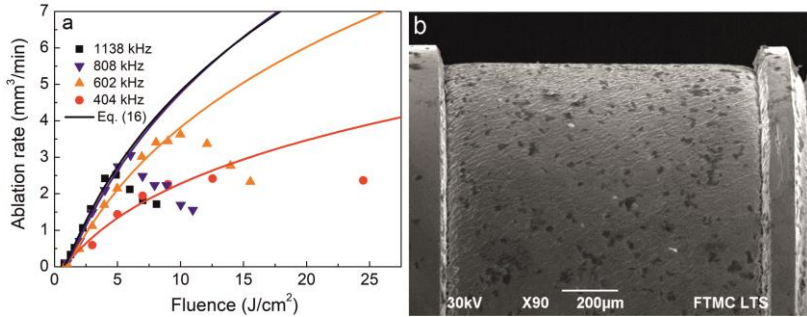
Fig. 46 (a) Ablation rate versus fluence for different pulse repetition rates. (b) SEM photograph of laser machined cavity. Laser processing parameters: wavelength 1064 nm, pulse duration 10 ps, beam radius $w_0 = 18$ μm, average laser power 22 W, pulse repetition rate 602 kHz, scanning speed 1080 mm/s, fluence 7 J/cm^2, ablation rate 3.5 mm^3/min, ablation efficiency 2.3 μm^3/μJ.

Efficient laser ablation was used for cylindrical sample texturing. High quality blade-riblet structures were made. The machined cylindrical copper samples are shown in Fig. 47.
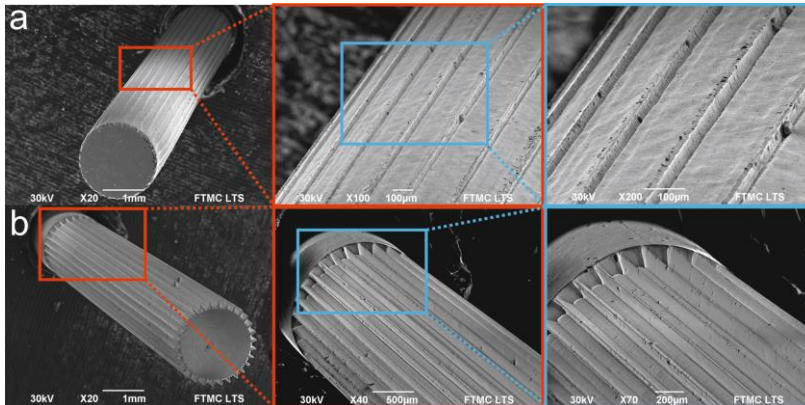
Fig. 47 SEM images of efficient laser machining on cylindrical surfaces. Average power 22 W, pulse repetition rate 602 kHz, scanning speed 1080 mm/s, fluence 7 J/cm^2, ablation rate 3.5 mm^3/min, ablation efficiency 2.3 μm^3/μJ. (a) width of the groove – 200 μm, thickness of the wall – 10 μm, height of the wall – 100 μm, surface roughness 1.2 μm. (b) width of the groove – 100 μm, thickness of the wall – 20 μm, height of the wall – 100 μm, surface roughness 0.8 μm.

5.3 Fabrication of drag-reducing riblet surface

The results published in paper [A6] are presented in this section. The fabrication of shark-skin-like trapezoidal riblet structures on PTFE was demonstrated. Drag reduction measurement setup was created and behaviour of riblet structures interaction with flowing air was investigated. PTFE with ablation efficiency one order of magnitude higher than one measured for copper was used for a substrate material in the drag reduction measurement experiments.

5.3.1 Laser processing and drag reduction measurement

The industrial-grade laser (Atlantic, Ekspla) was used in the experiments: pulse duration of 10 ps; wavelength of 355 nm; pulse energy of 45 μJ; repetition rate of 100 kHz; average laser power of 4.5 W. The galvanometer scanner (SCANcube 10, Scanlab) was used to control the beam position on the sample with the scanning speed up to 2 m/s. The beam was focused on the surface of the target material by a F-theta objective with the focal length of 176 mm. The beam diameter on the PTFE sample was 20.4 μm measured by a Liu technique described in [26]. The PTFE (Virgin PTFE, Heliopolis) target with the thickness of 0.5 mm was used in the ablation tests. The simplified geometry of the shark-skin-like structures consisting of periodically arranged riblets was formed on the surface of PTFE (Fig. 48). The height of the riblet was set to half of the period as $s/h = 2$ for optimal drag reduction suggested in [116,188–191]. For implementation of riblet structures, the periodical one-dimensional array of riblets with the periods form 50 μm to 250 μm and related heights from 25 μm to 125 μm were formed. The focused laser beam was scanned on the PTFE sample. The patterns consisting of scanned parallel lines with controlled distance between them were machined. The trapezoidal cavities were ablated and riblet structures were formed on PTFE as shown in Fig. 48 a. The temperature of PTFE sample was controlled by the hot plate (TK23, Technokartell) from 20 °C to 300 °C. The ablation rates were measured from the profiles at different parameters, laser beam scanning speeds and temperatures of the preheated sample.

The experimental setup of the drag measurement stage is given in Fig. 48 b. The air compressor (MK113-200-4, Fini) with an air receiver capacity of 0.2 m³ and max air pressure of 1.0 MPa was used for pressured air supply. The air source treatment unit (XMAL4000-04, XCPC) was used to control the air pressure in the range from 0.05 MPa to 0.85 MPa. The inline flow control valve (CPFC250, Pneumadyne) was used to control the air flow. The air flow sensor (PF2A751-F04-67, SMC) was used to measure the flow rate of air on

the investigated surfaces from 0.83 dm^3/s to 8.3 dm^3/s. The precision digital force gauge (FMI-S30A5, Alluris) was used to measure the drag force from 0 N to 5 N with the accuracy of 0.15% and a resolution of 0.001 N. The lever was used to control the force value on the tip by adjusting the ratio between the lever arms. The flat unstructured PTFE surface was used as the reference.
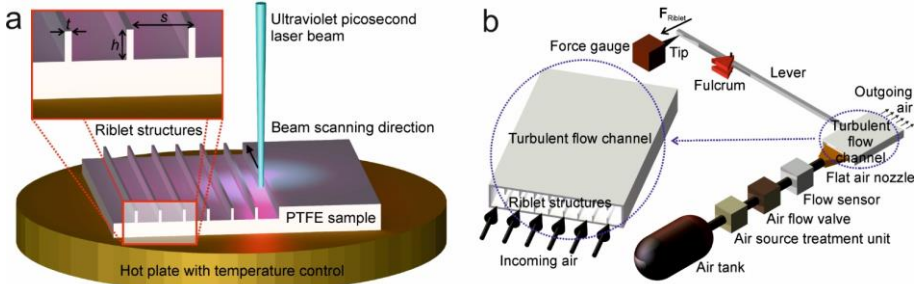
Fig. 48 (a) Schematic representation of the riblet structure formation by using ultraviolet picosecond laser ablation on preheated PTFE sample. The laser beam coming from the top is scanned on the PTFE sheet and riblet structures are formed. The initial temperature of the PTFE target material is controlled by the hot plate. The three basic spatial characteristics of the blade riblets (height *h,* thickness *t,* and spacing *s)* are shown in the enlarged fragment of the riblet structures marked with the red line. (b) Experimental setup of the drag measurement stage. Compressed air is supplied from an air tank. The air pressure is controlled by an air source treatment unit. The air flow rate is controlled by a flow valve. The air rate is measured by a flow sensor, and the air stream is homogenized by a flat air nozzle. The turbulent flow channel is constructed from the two PTFE plates with riblet structures on the interior sides (see enlarged scheme indicated by a blue dotted line). The lever with an adjustable fulcrum was used to control the force F_{Riblet} measured by using a force gauge and tip.

5.3.2   Ablation of preheated substrate

The ablation rate of the pre-heated PTFE dependence on the scanning speed is given in Fig. 49. The ablation rate was always higher for the higher temperature of pre-heated PTFE. The highest ablation rate was achieved at the temperature of 300 °C and at the beam scanning speed in the range from 1.4 m/s to 2.0 m/s. This effect of ablation rate enhancement by increasing initial sample temperature is related to the reduction of energy required to evaporate the PTFE. The melting point for the PTFE tape is 327 °C and the thermal decomposition temperature of PTFE tape is 589 °C and 614 °C [192], therefore, preheating to 300 °C makes significant difference. Consequently, less laser energy is required to reach the thermal decomposition of the hot sample, compared to the sample at room temperature. A similar effect has been observed in the increase of the critical scanning speed for smooth ablation by increasing an offset temperature of stainless steel with a picosecond laser [41]. The 30% enhancement in ablation efficiency from

30.0 $\mu m^3/\mu J$ at 20 °C temperature to 38.9 $\mu m^3/\mu J$ at 300 °C has been achieved in this work. The processing parameter set of maximal ablation efficiency has been used for laser machining of drag reducing riblet structures on preheated PTFE. The maximal removal rate of preheated Teflon was 10.5 mm^3/min ($\tau_p = 10$ ps, $\lambda = 355$ nm, $E_p = 45$ μJ, $f_p = 100$ kHz, $P = 4.5$ W). This laser processing is five times faster when compared with the removal rate for copper 2.0 mm^3/min achieved with the same laser's fundamental harmonic ($\tau_p = 10$ ps, $\lambda = 1064$ nm, $E_p = 130$ μJ, $f_p = 100$ kHz, $P = 13$ W). Therefore, Teflon substrate was selected for fabrication of numerous samples for investigation of drag-reducing properties of riblets.
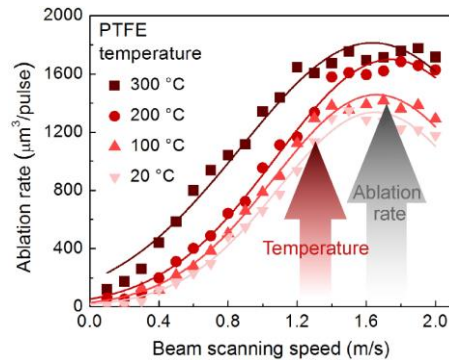
Fig. 49 Laser ablation rate of pre-heated PTFE dependence on the beam scanning speed at different temperatures. Laser processing parameters: pulse duration $\tau_p = 10$ ps; irradiation wavelength $\lambda = 355$ nm; pulse energy $E_p = 45$ μJ; pulse repetition rate $f_p = 100$ kHz; average laser power $P = 4.5$ W; peak laser fluence $F_0 = 27.5$ J/cm^2.

The simplified version of shark-skin-like structures consisting of periodically arranged riblet has been fabricated on the PTFE surface. The riblet structures were formed by ablating periodically arranged grooves as shown in Fig. 48 a. The SEM images and height profiles of the riblet structures formed by the laser on the PTFE are given in Fig. 50.

The riblet height profiles provided in Fig. 50 b have an asymmetrical form. This is due to the measurement limitation occurring due to the stylus tip shape described in [193,194]. The riblet height to spacing ratio and thickness to spacing ratio dependence on the physical riblet spacing measured from the depth profiles are plotted in Fig. 51.
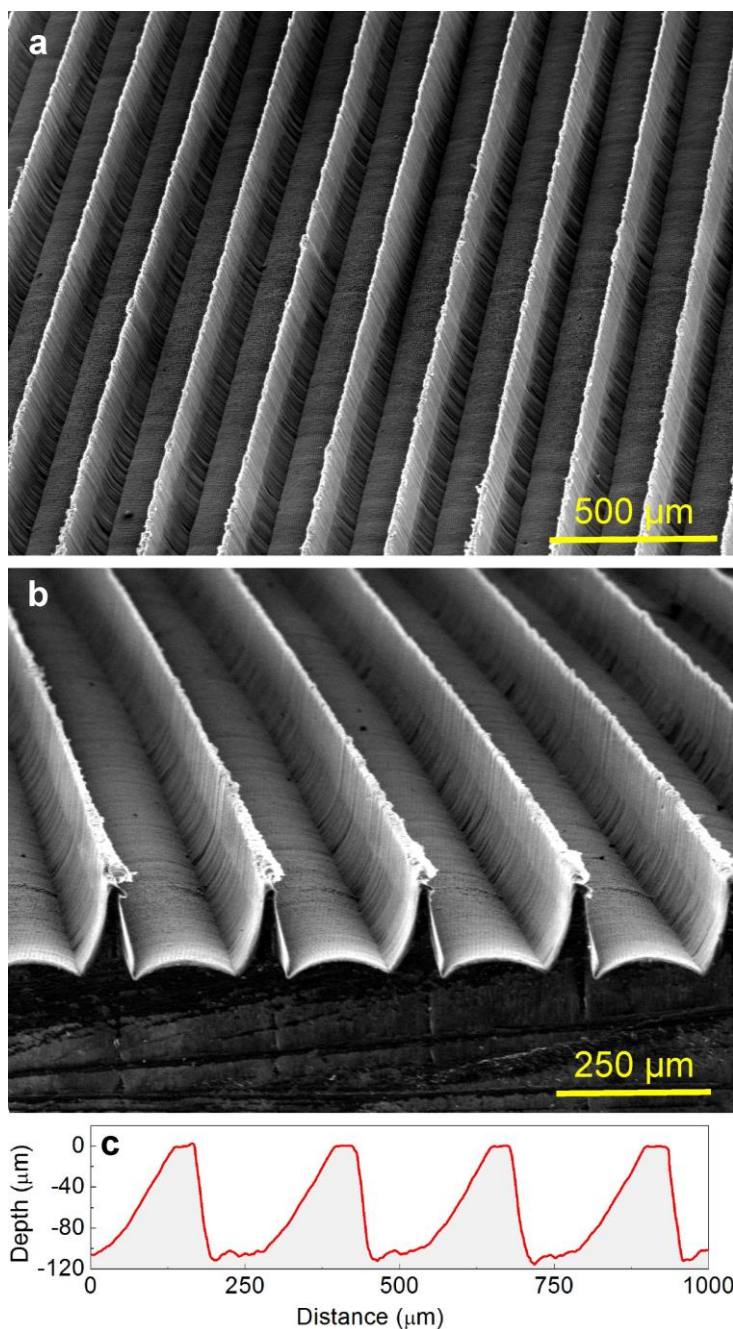
Fig. 50 (a), (b) SEM images and (c) cross section profile of laser ablated riblet structures on PTFE. Spatial characteristics of transverse riblet profile: physical spacing $s = 250 \pm 5$ μm; height $h = 127 \pm 3$ μm; thickness $t = 25 \pm 1$ μm. Laser processing parameters: offset temperature 300 °C; ablation rate $10.5 =$ mm^3/min, scanning speed $v = 1.5$ m/s; pulse duration $\tau_p = 10$ ps; irradiation wavelength $\lambda = 355$ nm; pulse energy $E_p = 45$ μJ; pulse repetition rate $f_p = 100$ kHz; average laser power $P = 4.5$ W; peak laser fluence $F_0 = 27.5$ J/cm^2.
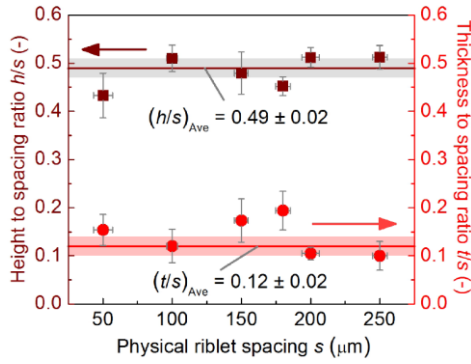
Fig. 51 Height to spacing ratio *h/s* and thickness to spacing ratio *t/s* of the laser ablated riblet dependence on the physical riblet spacing *s*. Error bars indicate standard deviation of height, thickness and spacing taken form 10 different position points of profiles.

The riblet height to spacing ratio achieved by the laser structuring stays constant around the average value of $(h/s)_{Ave} = 0.49 \pm 0.02$ for all riblet spacing's produced. The height to spacing ratio of the laser machined PTFE blade riblet structures was chosen to be close to 0.5 because of the largest drag reduction percentage reported in [116,188–191]. The riblet thickness to spacing ratio for the best drag reduction theoretically goes as small as 0.02 [116,191]. However, we have chosen a higher value of thickness to height ratio of $(t/s)_{Ave} = 0.12 \pm 0.02$ because of mechanical rigidity reasons [195–197].

5.3.3 Drag reduction

Drag reduction of the laser structured PTFE samples have been evaluated using a friction measurement setup shown in Fig. 48 b. The riblet period has been converted to the non-dimensional period, also called dimensionless spacing, by using the following expression $s^+ = su_\tau/v$, where *s* is the physical riblet spacing, u_τ is (skin) friction velocity, *v* is kinematic viscosity [185,186,190]. In this way, the results of the drag reduction were compared with data found in the scientific literature [140,190,193]. First, the non-textured PTFE surface was tested by measuring the friction force F_0 with air at different airflow values. Subsequently, the non-textured sample was replaced by a laser-textured PTFE and again the friction force F_{Riblet} with air was measured at different airflow values. Later, the force difference $\Delta F = F_{Riblet} - F_0$ of non-structured flat surface and laser-structured shark-skin-like surface was calculated at different air flow rates. The drag reduction rate has been calculated according to the ratio of the forces $\Delta F/F_0 = (F_{Riblet}/F_0 - 1) \times 100\%$ [136,187]. The drag reduction dependence on non-dimensional period s^+ is given in Fig. 52.
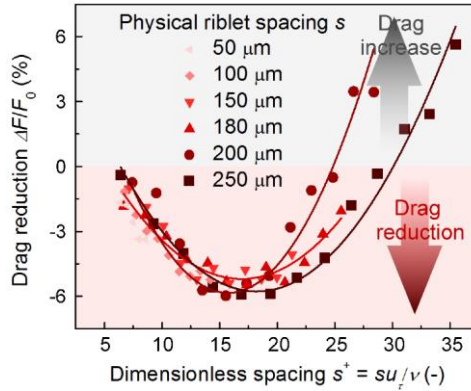
Fig. 52 The drag reduction of laser-textured PTFE surfaces dependence on non-dimensional riblet period s^+ at different physical riblet periods.

The calculation of the dimensionless spacing includes both the actual groove period and air flowing over the surface. Since the period of PTFE surface grooves was changed from 50 μm to 250 μm and air flow rate was changed from 0.83 dm³/s to 8.3 dm³/s, the dimensionless period values ranged from 7 to 35. It can be seen from Fig. 52 that the maximum drag reduction was achieved when the non-dimensional period s^+ is approximately between 14 and 20. At these values the decrease of the air friction on the shark-skin compared to the flat non-textured surface reaches 6%. Our results of the drag reduction are in good agreement with the literature values of trapezoidal riblets. The results presented in this work show that with the help of direct laser ablation it is possible to mimic drag reducing shark-skin-like riblet structures on Teflon at high speeds.

5.4 Wettability control of steel by ripples and nanospikes

The results published in paper [A2] are presented in this section. Bio-inspired functional surface on stainless steel was created by a simple, single-step procedure via femtosecond laser structuring. To the best of our knowledge, there was no research work found in scientific literature exploring a single-step technique with the ability of tuning wetting state of stainless steel from highly-hydrophilic to superhydrophobic. In this work self-organisation phenomena due to impact of laser irradiation were used to alter the wetting properties.

5.4.1   Formation of ripples

Ultrashort pulse laser (Pharos, Light Conversion) was utilised to produce pulses of $\tau = 170$ fs duration, $f = 100$ kHz repetition rate, and $\lambda = 1026$ nm central wavelength. For the first experiment, horizontal lines separated by a

fixed hatch distance of $\Delta h = 5\,\mu m$ were scanned at $v = 1\,m/s$ speed and average laser power was varied from 0.1 W to 3.3 W (15 tests). For the second experiment, the laser power of $P = 3.3$ W and scanning speed of $v = 50\,mm/s$ were used while the hatch distance Δh was changed from $10\,\mu m$ to $110\,\mu m$ (11 tests). Also, the grid scanning strategy was used, which consisted of vertical and horizontal lines with Δh separation. The accumulated fluence was calculated by $F_{ACC} = 2P/v\Delta h$.

Ripples on stainless steel surface were generated by a raster scanning the femtosecond laser beam at high speed of $v = 1\,m/s$ and hatch distance of $\Delta h = 5\,\mu m$ resulting in the fabrication rate of 5 mm^2/s. The average power P was varied from 0.1 W to 3.3 W, corresponding to the peak laser fluence F_0 range from 0.03 J/cm^2 to 0.84 J/cm^2. The average number of pulses per spot area was $N = 157$ in this processing case. The formation of LIPSS on the steel started at a laser fluence of $F_0 = 0.08$ J/cm^2 with low areal density and the spatial period around $\Lambda = 0.75 \pm 0.4\,\mu m$ (Fig. 53). The high spatial period error was the consequence of irregular LIPSS distribution. Steel irradiated by laser fluences lower than $F_0 = 0.08$ J/cm^2 was visually the same as untreated one. The boundaries between grains were clearly visible with a grain size from ~5 µm to ~20 µm. After the laser fluence was further increased, the error of the spatial period stabilised down to a minimum value of $\Delta\Lambda = 0.1\,\mu m$ due to more regular ripples. With a low laser fluence, LIPSS were formed on top of the grains. With increasing the fluence, the boundaries have gradually vanished, and at the fluence of $F_0 = 0.25$ J/cm^2, the grain boundaries were entirely hidden by ripples. The average periodicity of LIPSS was around $\Lambda = 0.75\,\mu m$ for the fluence F_0 interval ranging from 0.08 J/cm^2 to 0.84 J/cm^2.
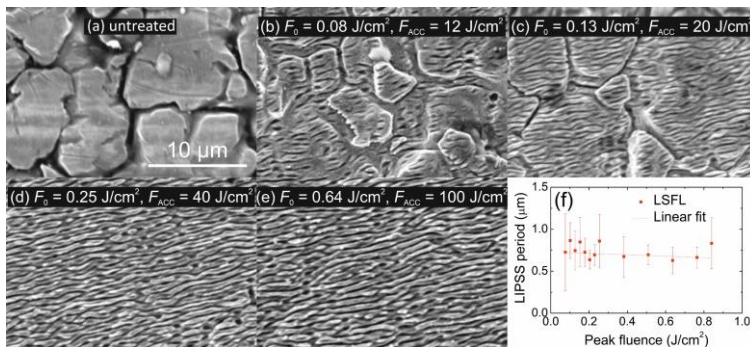
Fig. 53 Evolution of laser-induced ripple formation with increased peak fluence. (a-e) The grainy surface of stainless steel is being covered by LIPSS until the boundaries of grains have vanished. Scale bar in (a) is for all SEM images. (f) Periodicity of LIPSS measured by 2D-FFT of SEM images shows period of LSFL at $\Lambda = 0.75\,\mu m$. The pulse repetition rate $f = 100$ kHz, beam scanning speed $v = 1\,m/s$, hatch distance $\Delta h = 5\,\mu m$, pulse duration $\tau = 170$ fs, laser wavelength $\lambda = 1026$ nm.

In order to apply a higher number of pulses per spot, the beam scanning speed was lowered to $v = 50$ mm/s. The laser fluence was kept at $F_0 = 0.84$ J/cm^2 and hatch distance was varied from 10 µm to 110 µm, corresponding to pulses per spot from 3141 to 285, respectively. For the lowest hatch distance, an intense material ablation and the formation of lotus-leaf-like nanospikes on the irradiated area were obtained instead of ripples. When the hatch distance was increased, the formation of ripples started to appear (Fig. 54). For the hatch distance of 30 µm, the periodical surface structures were covered by nanospikes, while for 40 µm, the ripples were dominant, and only a hint of nanospikes was visible. When the hatch distance exceeded 90 µm, individual scan lines were distinguishable.
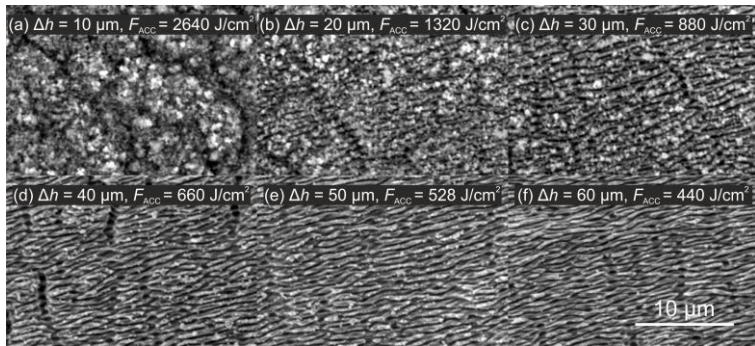
Fig. 54 SEM images of laser-induced nanospikes and ripples after laser irradiation with various hatch distance Δh ranging from 10 µm to 60 µm, step 10 µm. (a, b) The surface of stainless steel textured by nanospikes; (c) surface textured by ripples and nanospikes; (d-f) surface textured by ripples. Scale bar in (f) is for all SEM images. The laser fluence $F_0 = 0.84$ J/cm^2, pulse repetition rate $f = 100$ kHz, beam scanning speed $v = 50$ mm/s, pulse duration $\tau = 170$ fs, laser wavelength $\lambda = 1026$ nm.

5.4.2   Wettability

The untreated steel surface was hydrophilic and had a contact angle (CA) of 4°. The grains, present on the stainless steel surface, induced the roughness which was responsible for the Wenzel wetting state and the hydrophilicity [202]. In this wetting state water filled the grooves of the grain boundaries. The depth of these grooves was in the range of ~1 – 2 µm resulting in $R_a = 0.3$ µm. The similar CA was measured for the laser-irradiated surfaces by laser fluence smaller than the LIPSS generation threshold. While the peak fluence was increased, the transition from the hydrophilic to the hydrophobic surface was observed (Fig. 55). The increase of contact angle correlated well with the laser-induced ripples formation, which smoothly covered the grains present at the native surface forming the Cassie-Baxter wetting state [203]. In this state, water rests on top of the ripples with air

trapped beneath. The typical depth of ripples was about $\sim 0.1 - 0.4\,\mu$m with surface roughness of $R_a = 0.2\,\mu$m measured by AFM. The generation of ripples in nano-scale and smoothing the grooves in micro-scale resulted in increased surface repellence to water. In the case of rapid 5 mm^2/s (scanning speed $v = 1$ m/s and hatch distance $\Delta h = 5\,\mu$m) processing, the highest CA was 135°. In order to obtain superhydrophobic surface, the beam scanning speed was reduced to $v = 50$ mm/s to generate a higher accumulated fluence on the sample surface. In this case, the accumulated fluence was varied by changing the hatch distance between the scanned lines. The lowest hatch distance corresponded to the highest accumulated fluence and vice versa. For example, at the hatch distance of $\Delta h = 10\,\mu$m, the accumulated fluence was 2640 J/cm^2 and for $\Delta h = 110\,\mu$m – 240 J/cm^2. For the higher accumulated fluence, the superhydrophobic surface was fabricated. It was impossible to measure the contact angle for the superhydrophobic surfaces due to their high water repellent properties. For the cases where it was impossible to stick the droplet on the laser processed area, the contact angle was assumed to be 150°. The lowest accumulated fluence for which the superhydrophobic state was observed was 264 J/cm^2. The full contact angle range, from the initial hydrophilic to superhydrophobic surface, was fabricated by the femtosecond laser texturing. We can assume that the key parameter responsible for the surface wetting was the accumulated fluence.
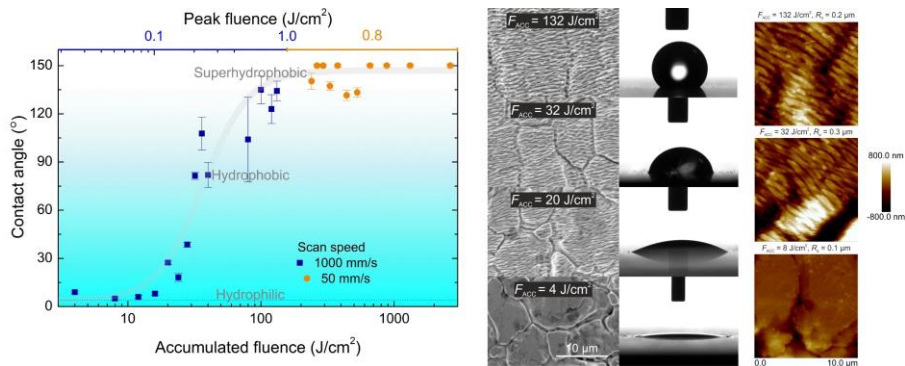
Fig. 55 Water droplet contact angle with laser-textured stainless steel surface versus the accumulated fluence. The blue squares represent the contact angle measurement results when the pulse energy was varied, keeping the scanning speed $v = 1$ m/s, hatch distance $\Delta h = 5\,\mu$m; orange circles – the hatch distance variation, with fixed scanning speed $v = 50$ mm/s, and peak fluence $F_0 = 0.84$ J/cm^2. On the right – SEM, CCD camera and AFM pictures showing the evolution of ripples formation with increased accumulated fluence and corresponding water droplet with ascending contact angle from bottom to top. Images of 3 µL water droplets on laser-textured steel surfaces show the transition from the highly-hydrophilic (bottom) to hydrophobic (top) surface. The pulse repetition rate $f = 100$ kHz, pulse duration $\tau = 170$ fs, laser wavelength $\lambda = 1026$ nm.

5.4.3   Chemical analysis

In addition to the surface structure, hydrophobic and hydrophilic properties of the material are strongly influenced by its chemical composition. Usually, the surface of metals and their alloys are covered by oxide films of those metals, resulting in high surface energy and hydrophilic properties. However, the situation changes when the surface is exposed to laser irradiation or other aggressive conditions that initiate adsorption, chemisorption and chemical interactions of gases or moisture presented in ambient air with the surface. It is well known that hydrophilic surfaces with the high surface energy are rich in polar functional groups (-CO, -OH, -NH$_2$, -COOH), while hydrophobic non-polar (alkyl, fluoralkyl groups, -SH). All these statements suggest (assuming that the morphology of all surfaces is the same) that as the oxygen content increases, the surface hydrophilicity should increase as well while increasing carbon content (for example chemisorption of non-polar hydrocarbons presented in an air atmosphere) leads to hydrophobic properties. The corresponding dependence has been described in many scientific articles [131,204,205]. However, the EDS analysis of our experiments showed completely opposite results coinciding with other works [206,207]. The carbon content was highest for the laser fluence below the ripple formation threshold and dropped down about four times when the ripple generation started. The oxygen content was significantly increased at the high accumulated fluence values. Such behaviour could be explained by decomposition of CO$_2$ (present in ambient air) following by the reaction with a non-stoichiometric oxygen-deficient active magnetite Fe$_3$O$_{4-\delta}$ ($0 < \delta < 1$) created during the laser irradiation process [131]. The decomposition reaction of one CO$_2$ molecule generates one C atom settling on the surface of the alloy, and two O^{2-} ions which are transferring to oxygen vacancies in Fe$_3$O$_{4-\delta}$ resulting in the formation of stoichiometric Fe$_3$O$_4$ [208]. As a result, oxygen-to-carbon (O/C) atomic percentage ratio increases together with the increase of the accumulated laser fluence (Fig. 56 inset). Similar results of O/C ratio increase with an increase of the number of laser pulses per spot for stainless steel textured by LIPSS using femtosecond laser was reported by Razi *et al* [209]. In contradiction, almost constant O/C ratio with the increase of the irradiation dose has been observed in ref [7]. However, the irradiation dose has been varied just up to 30 J/cm^2. The contact angle dependence on the oxygen-to-carbon ratio is depicted in Fig. 56. The static CA of ~7° was observed for the O/C ratio smaller than 0.35. The steep rise of static CA from ~7° up to ~150° was observed for the O/C ratios from 0.35 to 0.45. The superhydrophobic state with a non-changing static CA > 150° for the O/C

ratios ranging from 0.45 to 2.2 was registered. The O/C ratio clearly is responsible for the wetting state change of stainless steel surface, treated by femtosecond pulses. Similar results of static CA rise from 136° to 173° with the increase of O/C percentage per weight ratio from 1.23 to 3.6 on stainless steel textured by LIPSS using a picosecond laser was observed by Faas *et al* [207]. It is essential to mention that both stoichiometric and non-stoichiometric magnetite are metal oxides and, independent of the presence or absence of oxygen vacancies, are polar. They both have high surface energy and exhibit strong hydrophilic properties. On the other hand, elemental carbon and carbon derivatives show hydrophobic properties [210–212]. Therefore, the attachment of two oxygen ions does not significantly affect the increase in hydrophilic properties. Contrary, the deposition of one carbon atom strongly induces the surface hydrophobicity and the percentage increase in oxygen leading to a percentage decrease in carbon as observed in EDS analysis. The real increase in both, carbon and oxygen elements amount, is confirmed by the decreasing of the other elements' joint percentage amount.
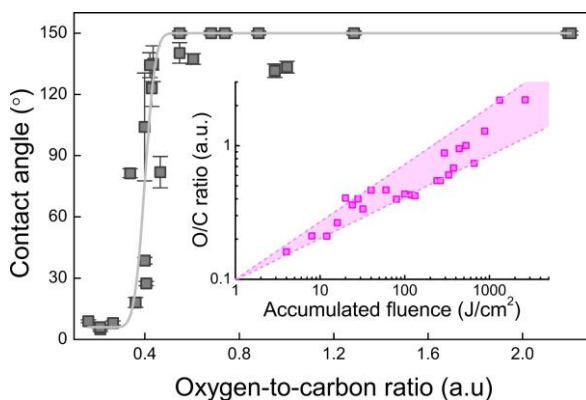
Fig. 56 Contact angle dependence on the oxygen-to-carbon (O/C) ratio in the laser-textured stainless steel. Inset: O/C ratio versus accumulated laser fluence. The pulse repetition rate $f = 100$ kHz, pulse duration $\tau = 170$ fs, laser wavelength $\lambda = 1026$ nm.

This phenomenon was also confirmed by the significant increase in oxygen content when nanospikes were formed (at the high accumulated fluence values of ~ 1 kJ/cm^2). The smaller the particle size was, the larger the oxygen-deficient degree was, resulting in the higher activity of the CO_2 decomposition [208]. Furthermore, materials made up of nanospikes have a relatively larger surface area when compared to the same volume of material made up of bigger particles, therefore the interaction area increases. Nevertheless, all these considerations are assumptions and a more thorough chemical analysis should be performed to explain the role of surface chemistry for the hydrophobicity.

5.5 Summary

The process window of the highest ablation rate of 6 mm^3/min with an average laser power of 40 W was defined and used for fast 3D micro-machining. While using the most efficient 3-pulse MHz burst processing mode 10.5 mm^3/min ablation rate was achieved with the average optical power of 36 W. Surface roughness of the cavities were $R_a = 0.4$ µm.

Laser micro-machining of the cylindrical sample was optimised The highest ablation efficiency was reached for a pulse repetition rate of 602 kHz. The fluence region, where the highest ablation efficiency was achieved, coincidence well with the best machining quality in terms of relative surface roughness. The critical fluence, where ablation rate dropped, dependent on pulse repetition rate. For higher pulse repetition rates, critical fluence was lower. Surface texturing was demonstrated on a cylindrical surface and blade-riblets were fabricated using optimal processing parameters. Ablation rate of 3.5 mm^3/min and ablation efficiency of 2.3 µm^3/µJ were reached using 22 W.

The shark-skin-like structures were formed on the pre-heated PTFE surface by using picosecond ultraviolet laser irradiation. The ablation rate of the pre-heated PTFE sample at 300 °C temperature was 30% higher compared to the ablation rate with the sample at room temperature. With the optimal laser processing parameters for the highest ablation rate, the arrays of periodic grooves with a period varying from 50 µm to 250 µm were formed on the PTFE surface. The periodical riblet structures were tested and friction with air force dropped up to 6% compared to flat unstructured PTFE, for the non-dimensional riblet period of 14 – 20.

By varying the accumulated laser fluence from 4 J/cm^2 to 2.6 kJ/cm^2, the wide range of contact angles ranging from 4° to 150° on the irradiated stainless steel surface was measured. The initial highly-hydrophilic surface was gradually changed into a superhydrophobic one by laser-induced ripples and at the high accumulated fluences – nanospikes. The wetting state transition started together with the generation of ripples proving that surface structuring by ripples was responsible for surface wetting. The possible mechanism of surface chemistry change due to the decomposition of CO_2 molecules present in ambient air and followed by reaction with a $Fe_3O_{4-\delta}$ $(0 < \delta < 1)$ created in the irradiation process was discussed. The variation of steel wetting state was altered by laser processing and following change of surface chemistry.

The possibility to mimic the bio-inspired functional surfaces at a high processing rate has been demonstrated. The results of laser application contribute to technological conclusions, that controlled laser irradiation is a reliable tool to mimic functional surfaces found in nature.

MAIN RESULTS AND CONCLUSIONS

1. Quality of laser ablated surface was the best at the optimum processing parameters measured for the highest ablation efficiency.
2. Theoretical model of laser ablation of rectangular cavity incorporating the ablation threshold decrease and the saturation of ablation depth, if many pulses are applied to a single spot, was presented.
3. Ablation efficiency of copper milling by ultrashort pulses with $120\ \mu J$ pulse energy was increased by 50% using the beam size optimization technique. Ablation by bursts with 64.5 MHz intra-burst pulse repetition rate revealed that, in the best case, the ablation efficiency could be improved by 20% compared to the single-pulse for the beam-size-optimised regimes if 3-pulse burst is applied.
4. In the case of copper milling and drilling by 64.7 MHz bursts the ablation efficiency was highly depended on odd and even number of pulses per burst.
5. Laser drilling of copper by 4.88 GHz bursts with pulses per burst up to $P = 25$ did not improve the ablation efficiency compared to the conventional single-pulse drilling. Nevertheless, the utilisation of 64.7 MHz- and bi- bursts in drilling increased the efficiency up to 14%.
6. The possibility to mimic the bio-inspired functional surfaces at high processing rates has been demonstrated by conventional and 3D layer-by-layer laser machining.
7. Laser fabrication of riblets was demonstrated on flat and cylindrical surfaces.
8. Riblet-shaped functional surface reduced air drag by 6% compared with flat non-textured sample.
9. The initial highly hydrophilic steel surface was gradually changed into superhydrophobic by laser-induced ripples and for high accumulated fluences – nanospikes.
10. In conclusion, in this dissertation developed efficient laser milling technology with optimised ultrashort pulsed laser irradiation for the highest material removal and lowest surface roughness is a perfect tool for rapid micro-machining and fabrication of 3D bio-inspired functional surfaces.

BIBLIOGRAPHY

1.   C. Kerse, H. Kalaycıoğlu, P. Elahi, B. Çetin, D. K. Kesim, Ö. Akçaalan, S. Yavaş, M. D. Aşık, Ö. Bülent, H. Heinar, H. Ronald, and F. Ö. Ilday, "Ablation-cooled material removal with ultrafast bursts of pulses," Nature **537**, 84–88 (2016).
2.   J. Schille and U. Loeschner, "Ultrashort pulse lasers in high-rate laser micro processing – Quo vadis?," Adv. Opt. Technol. **10**, 233–237 (2021).
3.   R. Weber and T. Graf, "The challenges of productive materials processing with ultrafast lasers," Adv. Opt. Technol. **10**, 239–245 (2021).
4.   E. J. Y. Ling, J. Saïd, N. Brodusch, R. Gauvin, P. Servio, and A. M. Kietzig, "Investigating and understanding the effects of multiple femtosecond laser scans on the surface topography of stainless steel 304 and titanium," Appl. Surf. Sci. **353**, 512–521 (2015).
5.   N. Ackerl, G. Fisch, J. Auerswald, and K. Wegener, "Evolution of microstructures on stainless steel induced by ultra-short pulsed laser ablation," SN Appl. Sci. **2**, 1–10 (2020).
6.   C. Florian, E. Skoulas, D. Puerto, A. Mimidis, E. Stratakis, J. Solis, and J. Siegel, "Controlling the Wettability of Steel Surfaces Processed with Femtosecond Laser Pulses," ACS Appl. Mater. Interfaces **10**, 36564–36571 (2018).
7.   P. Gečys, A. Vinčiunas, M. Gedvilas, A. Kasparaitis, R. Lazdinas, and G. Račiukaitis, "Ripple formation by femtosecond laser pulses for enhanced absorptance of stainless steel," J. Laser Micro Nanoeng. **10**, 129–133 (2015).
8.   E. I. Ageev, V. P. Veiko, E. A. Vlasova, Y. Y. Karlagina, A. Krivonosov, M. K. Moskvin, G. V Odintsova, V. E. Pshenichnov, V. V Romanov, and R. M. Yatsuk, "Controlled nanostructures formation on stainless steel by short laser pulses for products protection against falsification," Opt. Express **26**, 2117–2122 (2018).
9.   Z. Wang, C.-W. Wang, M. Wang, and Q.-Z. Zhao, "Manipulation of tribological properties of stainless steel by picosecond laser texturing and quenching," Tribol. Int. **99**, 14–22 (2016).
10.   J. Bonse, S. V Kirner, M. Griepentrog, D. Spaltmann, and J. Krüger, "Femtosecond Laser Texturing of Surfaces for Tribological Applications," Materials (Basel). **11**, 801 (2018).
11.   D. Bäuerle, *Laser Processing and Chemistry* (Springer, 2011).
12.   M. Stafe, A. Marcu, and N. N. Puscas, *Pulsed Laser Ablation of Solids* (Springer Berlin Heidelberg, 2014).
13.   S. I. Anisimov, B. L. Kapeliovich, and T. L. Perl'man, "Electron emission from metal surfaces exposed to ultrashort laser pulses," Zh. Eksp. Teor. Fiz. **66**, 776–781 (1975).
14.   P. Balling, "Laser Coupling and Relaxation of the Absorbed Energy:

Metals, Semiconductors, and Dielectrics BT - Handbook of Laser Micro- and Nano-Engineering," in K. Sugioka, ed. (Springer International Publishing, 2020).

15. S. E. Black, *Laser Ablation: Effects and Applications* (Nova Science Publishers, 2011).

16. J. Winter, S. Rapp, M. Schmidt, and H. P. Huber, "Ultrafast laser processing of copper: A comparative study of experimental and simulated transient optical properties," Appl. Surf. Sci. **417**, 2–15 (2017).

17. L. Fengping, D. Ye, Y. Lijun, X. Yao, and M. Hong, "Surface Hybrid Structuring by Laser Removal and Subtractive Processing BT - Handbook of Laser Micro- and Nano-Engineering," in K. Sugioka, ed. (Springer International Publishing, 2020).

18. F. Ran-Ran, Z. Duan-Ming, W. Hua, L. Zhi-Hua, Y. Feng-Xia, and T. Xin-Yu, "Effect of Pulse Width and Fluence of Femtosecond Laser on Electron—Phonon Relaxation Time," Chinese Phys. Lett. **25**, 3716–3719 (2008).

19. J. Dowden and W. Schulz, *The Theory of Laser Materials Processing* (Springer, Cham, 2017).

20. G. Paltauf and P. E. Dyer, "Photomechanical Processes and Effects in Ablation," Chem. Rev. **103**, 487–518 (2003).

21. C. Wu and L. V Zhigilei, "Microscopic mechanisms of laser spallation and ablation of metal targets from large-scale molecular dynamics simulations," Appl. Phys. A Mater. Sci. Process. **114**, 11–32 (2014).

22. M. V Shugaev, M. He, Y. Levy, A. Mazzi, A. Miotello, N. M. Bulgakova, and L. V Zhigilei, "Laser-Induced Thermal Processes: Heat Transfer, Generation of Stresses, Melting and Solidification, Vaporization, and Phase Explosion BT - Handbook of Laser Micro- and Nano-Engineering," in K. Sugioka, ed. (Springer International Publishing, 2020).

23. M. M. Martynyuk, "Phase explosion of a metastable fluid," Combust. Explos. Shock Waves **13**, 178–191 (1977).

24. L. V Zhigilei, P. B. S. Kodali, and B. J. Garrison, "Molecular Dynamics Model for Laser Ablation and Desorption of Organic Solids," J. Phys. Chem. B **101**, 2028–2037 (1997).

25. N. M. Bulgakova and A. V. Bulgakov, "Pulsed laser ablation of solids: transition from normal vaporization to phase explosion," Appl. Phys. A Mater. Sci. Process. **73**, 199–208 (2001).

26. J. M. Liu, "Simple technique for measurements of pulsed Gaussian-beam spot sizes," Opt. Lett. **7**, 196–198 (1982).

27. Y. Jee, F. M. Becker, and M. R. Walser, "Laser-induced damage on single-crystal metal surfaces," J. Opt. Soc. Am. B **5**, 648–659 (1988).

28. O. Armbruster, A. Naghilou, M. Kitzler, and W. Kautek, "Spot size and pulse number dependence of femtosecond laser ablation thresholds of silicon and stainless steel," Appl. Surf. Sci. **396**, 1736–1740 (2017).

29.   A. Naghilou, O. Armbruster, and W. Kautek, "Femto- and nanosecond pulse laser ablation dependence on irradiation area: The role of defects in metals and semiconductors," Appl. Surf. Sci. **418**, 487–490 (2017).

30.   W. Kautek and J. Krueger, "Femtosecond pulse laser ablation of metallic, semiconducting, ceramic, and biological materials," Proc. SPIE **2207**, 600–611 (1994).

31.   S. Preuss, A. Demchuk, and M. Stuke, "Sub-picosecond UV laser ablation of metals," Appl. Phys. A **61**, 33–37 (1995).

32.   B. N. Chichkov, C. Momma, S. Nolte, F. von Alvensleben, and A. Tünnermann, "Femtosecond, picosecond and nanosecond laser ablation of solids," Appl. Phys. A **63**, 109–115 (1996).

33.   J. Furmanski, A. M. Rubenchik, M. D. Shirk, and B. C. Stuart, "Deterministic processing of alumina with ultrashort laser pulses," J. Appl. Phys. **102**, 073112 (2007).

34.   G. Račiukaitis, M. Brikas, P. Gečys, B. Voisiat, and M. Gedvilas, "Use of High Repetition Rate and High Power Lasers in Microfabrication: How to Keep the Efficiency High?," J. Laser Micro Nanoen. **4**, 186–191 (2009).

35.   B. Lauer, B. Jäggi, and B. Neuenschwander, "Influence of the pulse duration onto the material removal rate and machining quality for different types of steel," Phys. Procedia **56**, 963–972 (2014).

36.   B. Neuenschwander, G. F. Bucher, C. Nussbaum, B. Joss, M. Muralt, U. W. Hunziker, and P. Schuetz, "Processing of metals and dielectric materials with ps-laserpulses: results, strategies, limitations and needs," Laser Appl. Microelectron. Optoelectron. Manuf. **7584**, 75840R (2010).

37.   T. Kramer, Y. Zhang, S. Remund, B. Jaeggi, A. Michalowski, L. Grad, and B. Neuenschwander, "Increasing the Specific Removal Rate for Ultra Short Pulsed Laser-Micromachining by Using Pulse Bursts," J. Laser Micro Nanoen. **12**, 107–114 (2017).

38.   B. Jaeggi, S. Remund, R. Streubel, B. Goekce, S. Barcikowski, and B. Neuenschwander, "Laser Micromachining of Metals with Ultra-Short Pulses: Factors Limiting the Scale-Up Process," J. Laser Micro Nanoen. **12**, 267–273 (2017).

39.   B. Jaeggi, S. Remund, Y. Zhang, T. Kramer, and B. Neuenschwander, "Optimizing the Specific Removal Rate with the Burst Mode Under Varying Conditions," J. Laser Micro Nanoen. **12**, 258–266 (2017).

40.   B. Neuenschwander, B. Jaeggi, D. J. Foerster, T. Kramer, and S. Remund, "Influence of the burst mode onto the specific removal rate for metals and semiconductors," J. Laser Appl. **31**, 22203 (2019).

41.   F. Bauer, A. Michalowski, T. Kiedrowski, and S. Nolte, "Heat accumulation in ultra-short pulsed scanning laser ablation of metals," Opt. Express **23**, 1035–1043 (2015).

42.   A. Ancona, F. Röser, K. Rademaker, J. Limpert, S. Nolte, and A. Tünnermann, "High speed laser drilling of metals using a high

repetition rate, high average power ultrafast fiber CPA system," Opt. Express **16**, 8958–8968 (2008).

43. J. Byskov-Nielsen, J. M. Savolainen, M. S. Christensen, and P. Balling, "Ultra-short pulse laser ablation of metals: Threshold fluence, incubation coefficient and ablation rates," Appl. Phys. A Mater. Sci. Process. **101**, 97–101 (2010).

44. R. Weber, T. Graf, P. Berger, V. Onuseit, M. Wiedenmann, C. Freitag, and A. Feuer, "Heat accumulation during pulsed laser materials processing," Opt. Express **22**, 11312–11324 (2014).

45. R. N. Oosterbeek, S. Ashforth, O. Bodley, and M. C. Simpson, "Ablation threshold dependence on incident wavelength during ultrashort pulsed laser ablation," Int. J. Nanotechnol. **14**, 313–322 (2017).

46. M. Hashida, A. F. Semerok, O. Gobert, G. Petite, Y. Izawa, and J. .-Wagner, "Ablation threshold dependence on pulse duration for copper," Appl. Surf. Sci. **197**–**198**, 862–867 (2002).

47. G. Raciukaitis, M. Brikas, P. Gecys, and M. Gedvilas, "Accumulation effects in laser ablation of metals with high-repetition-rate lasers," Proc. SPIE **7005**, 70052L-1–11 (2008).

48. Z. Sun, M. Lenzner, and W. Rudolph, "Generic incubation law for laser damage and ablation thresholds," J. Appl. Phys. **117**, 073102-1–6 (2015).

49. C. Mauclair, D. Pietroy, Y. Di Maïo, E. Baubeau, J.-P. Colombier, R. Stoian, and F. Pigeon, "Ultrafast laser micro-cutting of stainless steel and PZT using a modulated line of multiple foci formed by spatial beam shaping," Opt. Lasers Eng. **67**, 212–217 (2015).

50. A. Gillner, J. Finger, P. Gretzki, M. Niessen, T. Bartels, and M. Reininghaus, "High power laser processing with ultrafast and multi-parallel beams," J. Laser Micro Nanoeng. **14**, 129–137 (2019).

51. O. Hofmann, J. Stollenwerk, and P. Loosen, "Design of multi-beam optics for high throughput parallel processing," J. Laser Appl. **32**, 12005 (2019).

52. F. Siegel, V. Schütz, U. Stute, and R. Kling, "Large-scale Riblet surfaces using multi-spot micro machining," Int. Congr. Appl. Lasers Electro-Optics **2010**, 753–761 (2010).

53. J. Schille, L. Schneider, P. Lickschat, U. Loeschner, R. Ebert, and H. Exner, "High-pulse repetition frequency ultrashort pulse laser processing of copper," J. Laser Appl. **27**, S28007 (2015).

54. B. Neuenschwander, B. Jaeggi, M. Schmid, and G. Hennig, "Surface structuring with ultra-short laser pulses: Basics, limitations and needs for high throughput," Phys. Procedia **56**, 1047–1058 (2014).

55. B. Wu, L. Deng, P. Liu, F. Zhang, J. Duan, and X. Zeng, "Effects of picosecond laser repetition rate on ablation of Cr12MoV cold work mold steel," Appl. Surf. Sci. **409**, 403–412 (2017).

56. "Carbide from Light Conversion specifications,"

https://lightcon.com/product/carbide-femtosecond-lasers/#specifications, accessed 01/04/2022.

57.   B. Neuenschwander, B. Jaeggi, M. Zimmermannn, V. Markovic, B. Resan, K. Weingarten, R. de Loor, and L. Penning, "Laser surface structuring with 100 W of average power and sub-ps pulses," J. Laser Appl. **28**, 022506 (2016).

58.   J. Schille, L. Schneider, and U. Loeschner, "Process optimization in high-average-power ultrashort pulse laser microfabrication: how laser process parameters influence efficiency, throughput and quality," Appl. Phys. A Mater. Sci. Process. **120**, 847–855 (2015).

59.   B. Neuenschwander, T. Kramer, B. Lauer, and B. Jaeggi, "Burst mode with ps- and fs-pulses: Influence on the removal rate, surface quality and heat accumulation," Proc. SPIE **9350**, 93500U-1–14 (2015).

60.   F. Di Niso, C. Gaudiuso, T. Sibillano, F. P. Mezzapesa, A. Ancona, and P. M. Lugarà, "Role of heat accumulation on the incubation effect in multi-shot laser ablation of stainless steel at high repetition rates," Opt. Express **22**, 12200–12210 (2014).

61.   R. Weber, T. Graf, C. Freitag, A. Feuer, T. Kononenko, and V. I. Konov, "Processing constraints resulting from heat accumulation during pulsed and repetitive laser materials processing," Opt. Express **25**, 3966–3979 (2017).

62.   J. Schille, L. Schneider, A. Streek, S. Kloetzer, and U. Loeschner, "High-throughput machining using a high-average power ultrashort pulse laser and high-speed polygon scanner," Opt. Eng. **55**, 1–10 (2016).

63.   R. Knappe, H. Haloui, A. Seifert, A. Weis, and A. Nebel, "Scaling ablation rates for picosecond lasers using burst micromachining," Proc. SPIE **7585**, 75850H-1–6 (2010).

64.   G. Bonamis, E. Audouard, C. Hönninger, J. Lopez, K. Mishchik, E. Mottay, and I. Manek-Hönninger, "Systematic study of laser ablation with GHz bursts of femtosecond pulses," Opt. Express **28**, 27702–27714 (2020).

65.   K. Sugioka, "Will GHz burst mode create a new path to femtosecond laser processing?," Int. J. Extrem. Manuf. **3**, 043001 (2021).

66.   T. Hirsiger, M. Gafner, S. Remund, M. V Chaja, A. Urniezius, S. Butkus, and B. Neuenschwander, "Machining metals and silicon with GHz bursts: Surprising tremendous reduction of the specific removal rate for surface texturing applications," Proc. SPIE **11267**, 112670T-1–12 (2020).

67.   D. Metzner, P. Lickschat, and S. Weißmantel, "High-quality surface treatment using GHz burst mode with tunable ultrashort pulses," Appl. Surf. Sci. **531**, 147270 (2020).

68.   M. Domke, V. Matylitsky, and S. Stroj, "Surface ablation efficiency and quality of fs lasers in single-pulse mode, fs lasers in burst mode, and ns lasers," Appl. Surf. Sci. **505**, 144594 (2020).

69. F. Nyenhuis, A. Michalowski, and J. L'huillier, "Surface treatment with GHz bursts," Proc. SPIE **11268**, 112680B-1–8 (2020).

70. P. Lickschat, D. Metzner, and S. Weißmantel, "Manufacturing of high quality 3D microstructures in stainless steel with ultrashort laser pulses using different burst modes," J. Laser Appl. **33**, 42002 (2021).

71. G. Bonamis, K. Mishchick, E. Audouard, C. Hönninger, E. Mottay, J. Lopez, and I. Manek-Hönninger, "High efficiency femtosecond laser ablation with gigahertz level bursts," J. Laser Appl. **31**, 22205 (2019).

72. K. Mishchik, G. Bonamis, J. Qiao, J. Lopez, E. Audouard, E. Mottay, C. Hönninger, and I. Manek-Hönninger, "High-efficiency femtosecond ablation of silicon with GHz repetition rate laser source," Opt. Lett. **44**, 2193–2196 (2019).

73. H. Matsumoto, Z. Lin, and J. Kleinert, "Ultrafast laser ablation of copper with ~GHz bursts," Proc. SPIE **10519**, 1051902-1–11 (2018).

74. D. J. Förster, S. Faas, S. Gröninger, F. Bauer, A. Michalowski, R. Weber, and T. Graf, "Shielding effects and re-deposition of material during processing of metals with bursts of ultra-short laser pulses," Appl. Surf. Sci. **440**, 926–931 (2018).

75. J. König, S. Nolte, and A. Tünnermann, "Plasma evolution during metal ablation with ultrashort laser pulses.," Opt. Express **13**, 10597–10607 (2005).

76. A. A. Foumani, D. J. Förster, H. Ghorbanfekr, R. Weber, T. Graf, and A. R. Niknam, "Atomistic simulation of ultra-short pulsed laser ablation of metals with single and double pulses: An investigation of the re-deposition phenomenon," Appl. Surf. Sci. **537**, 147775 (2021).

77. D. J. Förster, S. Faas, R. Weber, and T. Graf, "Thrust enhancement and propellant conservation for laser propulsion using ultra-short double pulses," Appl. Surf. Sci. **510**, 145391 (2020).

78. B. Jäggi, D. J. Förster, R. Weber, and B. Neuenschwander, "Residual heat during laser ablation of metals with bursts of ultra-short pulses," Adv. Opt. Technol. **7**, 175–182 (2018).

79. N. Hodgson, A. Steinkopff, S. Heming, H. Allegre, H. Haloui, T. S. Lee, M. Laha, and J. VanNunen, "Ultrafast laser machining: process optimization and applications," Proc. SPIE **11673**, 1167308-1–21 (2021).

80. C. Florian, S. V Kirner, J. Krüger, and J. Bonse, "Surface functionalization by laser-induced periodic surface structures," J. Laser Appl. **32**, 22063 (2020).

81. E. Stratakis, J. Bonse, J. Heitz, J. Siegel, G. D. Tsibidis, E. Skoulas, A. Papadopoulos, A. Mimidis, A. C. Joel, P. Comanns, J. Krüger, C. Florian, Y. Fuentes-Edfuf, J. Solis, and W. Baumgartner, "Laser engineering of biomimetic surfaces," Mater. Sci. Eng. R **141**, 100562 (2020).

82. M. Birnbaum, "Semiconductor Surface Damage Produced by Ruby Lasers," J. Appl. Phys. **36**, 3688–3689 (1965).

83.   J. Bonse, J. Krüger, S. Höhm, and A. Rosenfeld, "Femtosecond laser-induced periodic surface structures," J. Laser Appl. **24**, 42006 (2012).

84.   J. Bonse, S. Höhm, S. V Kirner, A. Rosenfeld, and J. Krüger, "Laser-Induced Periodic Surface Structures— A Scientific Evergreen," IEEE J. Sel. Top. Quantum Electron. **23**, 1 (2017).

85.   R. J. Nemanich, D. K. Biegelsen, and W. G. Hawkins, "Aligned, coexisting liquid and solid regions in laser-annealed Si," Phys. Rev. B **27**, 7817–7819 (1983).

86.   J. Bonse, S. Baudach, J. Krüger, W. Kautek, and M. Lenzner, "Femtosecond laser ablation of silicon–modification thresholds and morphology," Appl. Phys. A **74**, 19–25 (2002).

87.   A. Siegman and P. Fauchet, "Stimulated Wood's anomalies on laser-illuminated surfaces," IEEE J. Quantum Electron. **22**, 1384–1403 (1986).

88.   J. E. Sipe, J. F. Young, J. S. Preston, and H. M. van Driel, "Laser-induced periodic surface structure. I. Theory," Phys. Rev. B **27**, 1141–1154 (1983).

89.   G. Miyaji and K. Miyazaki, "Origin of periodicity in nanostructuring on thin film surfaces ablated with femtosecond laser pulses," Opt. Express **16**, 16265–16271 (2008).

90.   A. D. Boardman, *Electromagnetic Surface Modes* (Wiley, 1982).

91.   F. Garrelie, J. P. Colombier, F. Pigeon, S. Tonchev, N. Faure, M. Bounhalli, S. Reynaud, and O. Parriaux, "Evidence of surface plasmon resonance in ultrafast laser-induced ripples," Opt. Express **19**, 9035–9043 (2011).

92.   M. Huang, F. Zhao, Y. Cheng, N. Xu, and Z. Xu, "Origin of Laser-Induced Near-Subwavelength Ripples: Interference between Surface Plasmons and Incident Laser," ACS Nano **3**, 4062–4070 (2009).

93.   A. Borowiec and H. K. Haugen, "Subwavelength ripple formation on the surfaces of compound semiconductors irradiated with femtosecond laser pulses," Appl. Phys. Lett. **82**, 4462–4464 (2003).

94.   D. Dufft, A. Rosenfeld, S. K. Das, R. Grunwald, and J. Bonse, "Femtosecond laser-induced periodic surface structures revisited: A comparative study on ZnO," J. Appl. Phys. **105**, 34908 (2009).

95.   R. Buividas, L. Rosa, R. Šliupas, T. Kudrius, G. Šlekys, V. Datsyuk, and S. Juodkazis, "Mechanism of fine ripple formation on surfaces of (semi)transparent materials via a half-wavelength cavity feedback," Nanotechnology **22**, 55304 (2010).

96.   J. Bonse and S. Gräf, "Ten Open Questions about Laser-Induced Periodic Surface Structures," Nanomaterials **11**, 1–21 (2021).

97.   S. V Kirner, T. Wirth, H. Sturm, J. Krüger, and J. Bonse, "Nanometer-resolved chemical analyses of femtosecond laser-induced periodic surface structures on titanium," J. Appl. Phys. **122**, 104901 (2017).

98.   A. du Plessis, C. Broeckhoven, I. Yadroitsava, I. Yadroitsev, C. H. Hands, R. Kunju, and D. Bhate, "Beautiful and Functional: A Review

of Biomimetic Design in Additive Manufacturing," Addit. Manuf. **27**, 408–427 (2019).

99.   D. Wang, D. Chen, and Z. Chen, "Recent Progress in 3D Printing of Bioinspired Structures," Front. Mater. **7**, 1–10 (2020).

100.   C. Yan, P. Jiang, X. Jia, and X. Wang, "3D printing of bioinspired textured surfaces with superamphiphobicity," Nanoscale **12**, 2924–2938 (2020).

101.   R. Raman and R. Bashir, "Stereolithographic 3D Bioprinting for Biomedical Applications," in *Essentials of 3D Biofabrication and Translation*, A. Atala and J. Yoo, eds. (Elsevier, 2015).

102.   X. Liu, H. Gu, M. Wang, X. Du, B. Gao, A. Elbaz, L. Sun, J. Liao, P. Xiao, and Z. Gu, "3D Printing of Bioinspired Liquid Superrepellent Structures," Adv. Mater. **30**, 1800103 (2018).

103.   Y. Li, H. Mao, P. Hu, M. Hermes, H. Lim, J. Yoon, M. Luhar, Y. Chen, and W. Wu, "Bioinspired Functional Surfaces Enabled by Multiscale Stereolithography," Adv. Mater. Technol. **4**, 1800638 (2019).

104.   G. Merkininkaitė, D. Gailevičius, S. Šakirzanovas, and L. Jonušauskas, "Polymers for Regenerative Medicine Structures Made via Multiphoton 3D Lithography," Int. J. Polym. Sci. **2019**, 3403548 (2019).

105.   L. Qin, M. Hafezi, H. Yang, G. Dong, and Y. Zhang, "Constructing a Dual-Function Surface by Microcasting and Nanospraying for Efficient Drag Reduction and Potential Antifouling Capabilities," Micromachines **10**, 1–15 (2019).

106.   T. Yanagishita, M. Yoshida, and H. Masuda, "Renewable Superhydrophobic Surfaces Prepared by Nanoimprinting Using Anodic Porous Alumina Molds," Langmuir **37**, 10573–10578 (2021).

107.   H. Lv, S. Liu, P. Zhang, and Z. Tang, "Fabrication of biomimetic gecko setae by direct photolithography and micromolding processes," in *2011 6th IEEE International Conference on Nano/Micro Engineered and Molecular Systems* (2011), pp. 503–506.

108.   K. M. Tanvir Ahmmed and A.-M. Kietzig, "Drag reduction on laser-patterned hierarchical superhydrophobic surfaces," Soft Matter **12**, 4912–4922 (2016).

109.   Y. Wang, Z. Zhang, J. Xu, and H. Yu, "One-step method using laser for large-scale preparation of bionic superhydrophobic & drag-reducing fish-scale surface," Surf. Coatings Technol. **409**, 126801 (2021).

110.   C. Barbier, E. Jenner, and B. D'Urso, "Drag Reduction With Superhydrophobic Riblets," ASME 2012 Int. Mech. Eng. Congr. Expo. 199–205 (2012).

111.   E. Liu, L. Li, G. Wang, Z. Zeng, W. Zhao, and Q. Xue, "Drag reduction through self-texturing compliant bionic materials," Sci. Rep. **7**, 40038 (2017).

112. X. Wang, J. Xu, C. Wang, A. J. Sánchez Egea, J. Li, C. Liu, Z. Wang, T. Zhang, B. Guo, and J. Cao, "Bio-Inspired Functional Surface Fabricated by Electrically Assisted Micro-Embossing of AZ31 Magnesium Alloy," Materials (Basel). **13**, 412 (2020).

113. M. T. K. Ahmmed, C. Grambow, and A.-M. Kietzig, "Fabrication of Micro/Nano Structures on Metals by Femtosecond Laser Micromachining," Micromachines **5**, 1219–1253 (2014).

114. F. A. Müller, C. Kunz, and S. Gräf, "Bio-Inspired Functional Surfaces Based on Laser-Induced Periodic Surface Structures," Materials (Basel). **9**, 476 (2016).

115. W. Barthlott and C. Neinhuis, "Purity of the sacred lotus, or escape from contamination in biological surfaces," Planta **202**, 1–8 (1997).

116. B. Dean and B. Bhushan, "Shark-skin surfaces for fluid-drag reduction in turbulent flow: A review," Philos. Trans. R. Soc. A Math. Phys. Eng. Sci. **368**, 4775–4806 (2010).

117. W. Barthlott and C. Neinhuis, "Purity of the sacred lotus, or escape from contamination in biological surfaces," Planta **202**, 1–8 (1997).

118. R. Hensel, R. Helbig, S. Aland, A. Voigt, C. Neinhuis, and C. Werner, "Tunable nano-replication to explore the omniphobic characteristics of springtail skin," Npg Asia Mater. **5**, e37 (2013).

119. K. Koch, B. Bhushan, and W. Barthlott, "Multifunctional surface structures of plants: An inspiration for biomimetics," Prog. Mater. Sci. **54**, 137–178 (2009).

120. A. R. Parker and C. R. Lawrence, "Water capture by a desert beetle," Nature **414**, 33–34 (2001).

121. B. Bhushan, "Biomimetics: lessons from nature - an overview," Philos. Trans. R. Soc. A Math. Phys. Eng. Sci. **367**, 1445–1486 (2009).

122. J. Gray, "Studies in Animal Locomotion : VI. The Propulsive Powers of the Dolphin," J. Exp. Biol. **13**, 192–199 (1936).

123. D. W. Bechert, M. Bruse, W. Hage, J. G. T. Van der Hoeven, and G. Hopper, "Experiments on drag-reducing surfaces and their optimization with an adjustable geometry," J. Fluid Mech. **338**, 59–87 (1997).

124. G. Tian, D. Fan, X. Feng, and H. Zhou, "Thriving artificial underwater drag-reduction materials inspired from aquatic animals: progresses and challenges," RSC Adv. **11**, 3399–3428 (2021).

125. X. Pu, G. Li, and H. Huang, "Preparation, anti-biofouling and drag-reduction properties of a biomimetic shark skin surface," Biol. Open **5**, 389–396 (2016).

126. L. Y. L. Wu, S. K. Ngian, Z. Chen, and D. T. T. Xuan, "Quantitative test method for evaluation of anti-fingerprint property of coated surfaces," Appl. Surf. Sci. **257**, 2965–2969 (2011).

127. K. Liu and L. Jiang, "Metallic surfaces with special wettability," Nanoscale **3**, 825–838 (2011).

128. J. Zimmermann, F. A. Reifler, G. Fortunato, L.-C. Gerhardt, and S.

Seeger, "A Simple, One-Step Approach to Durable and Robust Superhydrophobic Textiles," Adv. Funct. Mater. **18**, 3662–3669 (2008).

129.   A. H. A. Lutey, L. Gemini, L. Romoli, G. Lazzini, F. Fuso, M. Faucon, and R. Kling, "Towards Laser-Textured Antibacterial Surfaces," Sci. Rep. **8**, 10112 (2018).

130.   K.-C. Park, S. S. Chhatre, S. Srinivasan, R. E. Cohen, and G. H. McKinley, "Optimal Design of Permeable Fiber Network Structures for Fog Harvesting," Langmuir **29**, 13269–13277 (2013).

131.   A.-M. Kietzig, S. G. Hatzikiriakos, and P. Englezos, "Patterned Superhydrophobic Metallic Surfaces," Langmuir **25**, 4821–4827 (2009).

132.   G. Giannuzzi, C. Gaudiuso, R. Di Mundo, L. Mirenghi, F. Fraggelakis, R. Kling, P. M. Lugarà, and A. Ancona, "Short and long term surface chemistry and wetting behaviour of stainless steel with 1D and 2D periodic structures induced by bursts of femtosecond laser pulses," Appl. Surf. Sci. **494**, 1055–1065 (2019).

133.   M. J. Wood, P. Servio, and A.-M. Kietzig, "The Tuning of LIPSS Wettability during Laser Machining and through Post-Processing," Nanomaterials **11**, 1–15 (2021).

134.   A.-M. Kietzig, M. Negar Mirvakili, S. Kamal, P. Englezos, and S. G. Hatzikiriakos, "Laser-Patterned Super-Hydrophobic Pure Metallic Substrates: Cassie to Wenzel Wetting Transitions," J. Adhes. Sci. Technol. **25**, 2789–2809 (2011).

135.   M. Martínez-Calderon, A. Rodríguez, A. Dias-Ponte, M. C. Morant-Miñana, M. Gómez-Aranzadi, and S. M. Olaizola, "Femtosecond laser fabrication of highly hydrophobic stainless steel surface with hierarchical structures fabricated by combining ordered microstructures and LIPSS," Appl. Surf. Sci. **374**, 81–89 (2016).

136.   S. V Kirner, U. Hermens, A. Mimidis, E. Skoulas, C. Florian, F. Hischen, C. Plamadeala, W. Baumgartner, K. Winands, H. Mescheder, J. Krüger, J. Solis, J. Siegel, E. Stratakis, and J. Bonse, "Mimicking bug-like surface structures and their fluid transport produced by ultrashort laser pulse irradiation of steel," Appl. Phys. A **123**, 754 (2017).

137.   U. Hermens, S. V Kirner, C. Emonts, P. Comanns, E. Skoulas, A. Mimidis, H. Mescheder, K. Winands, J. Krüger, E. Stratakis, and J. Bonse, "Mimicking lizard-like surface structures upon ultrashort laser pulse irradiation of inorganic materials," Appl. Surf. Sci. **418**, 499–507 (2017).

138.   T. Kim, R. Shin, M. Jung, J. Lee, C. Park, and S. Kang, "Drag reduction using metallic engineered surfaces with highly ordered hierarchical topographies: nanostructures on micro-riblets," Appl. Surf. Sci. **367**, 147–152 (2016).

139.   M. Pfeiffer, A. Engel, H. Gruettner, K. Guenther, F. Marquardt, G.

Reisse, and S. Weissmantel, "Ripple formation in various metals and super-hard tetrahedral amorphous carbon films in consequence of femtosecond laser irradiation," Appl. Phys. A **110**, 655–659 (2013).

140.   C. Lietmeyer, B. Denkena, T. Krawczyk, R. Kling, L. Overmeyer, B. Wojakowski, E. Reithmeier, R. Scheuer, T. Vynnyk, and J. R. Seume, "Recent Advances in Manufacturing of Riblets on Compressor Blades and Their Aerodynamic Impact," J. Turbomach. **135**, 1–12 (2013).

141.   P. Heyl, T. Olschewski, and R. W. Wijnaendts, "Manufacturing of 3D structures for micro-tools using laser ablation," Microelectron. Eng. **58**, 775–780 (2001).

142.   A. Žemaitis, M. Gaidys, M. Brikas, P. Gečys, G. Račiukaitis, and M. Gedvilas, "Advanced laser scanning for highly- efficient ablation and ultrafast surface structuring: experiment and model," Sci. Rep. **8**, 17376 (2018).

143.   G. D. Bixler and B. Bhushan, "Shark skin inspired low-drag microstructured surfaces in closed channel flow," J. Colloid Interface Sci. **393**, 384–396 (2013).

144.   E. Li, X. Hu, and P. Yao, "Drag reduction of rectangular riblets in a positive pressure gradients duct flow," UPB Sci. Bull. Ser. D Mech. Eng. **81**, 191–206 (2019).

145.   X. C. Wang and Y. C. Wan, "Picosecond laser fabrication of the riblet-array surface texture on Ti64 alloy substrate," J. Laser Micro Nanoeng. **14**, 206–213 (2019).

146.   A. Sareen, R. W. Deters, S. P. Henry, and M. S. Selig, "Drag Reduction Using Riblet Film Applied to Airfoils for Wind Turbines," J. Sol. Energy Eng. **136**, 1–8 (2013).

147.   P. R. Viswanath, "Aircraft viscous drag reduction using riblets," Prog. Aerosp. Sci. **38**, 571–600 (2002).

148.   E. L. Houghton, P. W. Carpenter, S. H. Collicott, and D. T. Valentine, "Chapter 10 - Flow Control and Wing Design," in *Aerodynamics for Engineering Students (Seventh Edition)* (Butterworth-Heinemann, 2017).

149.   P. Jackson Peacock, Lindsay T., Munson, Kenneth., Taylor, John W. R., *Jane's All the World's Aircraft, 1997-98* (Jane's Information Group, 1997).

150.   V. Lang, T. Roch, and A. F. Lasagni, "World record in high speed laser surface microstructuring of polymer and steel using direct laser interference patterning," Proc. SPIE **9736**, 97360Z-1–8 (2016).

151.   "Lasers Produce Shark Skins on Aircraft," https://www.4jet.de/en/news/lasers-produce-shark-skins-on-aircraft, accessed 09/04/2022.

152.   "Nature as a role model: Lufthansa Group and BASF roll out sharkskin technology," https://www.lufthansagroup.com/en/newsroom/releases/innovation-technology/nature-as-a-role-model-lufthansa-group-and-basf-roll-out-

sharkskin-technology.html, accessed 09/04/2022.

153. "AeroSHARK Cutting emissions with sharkskin technology," https://www.lufthansa-technik.com/aeroshark, accessed 09/04/2022.

154. W. Rong, H. Zhang, Z. Mao, L. Chen, and X. Liu, "Stable drag reduction of anisotropic superhydrophobic/hydrophilic surfaces containing bioinspired micro/nanostructured arrays by laser ablation," Colloids Surfaces A Physicochem. Eng. Asp. **622**, 126712 (2021).

155. H. Sun, "Thin lens equation for a real laser beam with weak lens aperture truncation," Opt. Eng. **37**, 2906–2913 (1998).

156. P. Parandoush and A. Hossain, "A review of modeling and simulation of laser beam machining," Int. J. Mach. Tools Manuf. **85**, 135–145 (2014).

157. M. Domke, B. Egle, G. Piredda, G. Fasching, M. Bodea, and E. Schwarz, "Controlling depth and distance of the hole formations at the bottom of laser-scribed trenches in silicon using fs-pulses," Proc. SPIE **9350**, 93501J-1–6 (2015).

158. N. Lukac, T. Suhovršnik, M. Lukac, and M. Jezeršek, "Ablation characteristics of quantum square pulse mode dental erbium laser," J. Biomed. Opt. **21**, 015012 (2016).

159. L. T. Cangueiro, R. Vilar, A. M. Botelho do Rego, and V. S. F. Muralha, "Femtosecond laser ablation of bovine cortical bone," J. Biomed. Opt. **17**, 125005 (2012).

160. L. Ji, L. Li, H. Devlin, Z. Liu, J. Jiao, and D. Whitehead, "Ti: Sapphire femtosecond laser ablation of dental enamel, dentine, and cementum," Lasers Med. Sci. **27**, 197–204 (2012).

161. C. Dugas, Y. Bengio, F. Belisle, C. Nadeau, and R. Garcia, "Incorporating Second-Order Functional Knowledge for Better Option Pricing," Proc. NIPS 472–478 (2001).

162. W. Kautek and O. Armbruster, "Non-Thermal Material Response to Laser Energy Deposition," in *Lasers in Materials Science*, M. Castillejo, P. M. Ossi, and L. Zhigilei, eds. (Springer, Cham, 2014).

163. W. Kautek, J. Krüger, M. Lenzner, S. Sartania, C. Spielmann, and F. Krausz, "Laser ablation of dielectrics with pulse durations between 20 fs and 3 ps," Appl. Phys. Lett. **3146**, 18–21 (1996).

164. R. Delmdahl and R. Paetzel, "Laser Drilling of High-Density Through Glass Vias (TGVs) for 2.5D and 3D Packaging," J. Microelectron. Packag. Soc. **21**, 53–57 (2014).

165. C. Daengngam, I. Kandas, I. Ashry, A. Wang, R. James, and Y. Xu, "Fabrication and characterization of periodically patterned silica fiber structures for enhanced second-order nonlinearity," Opt. Express **23**, 8113 (2015).

166. C. Dorronsoro, J. Siegel, L. Remon, and S. Marcos, "Suitability of Filofocon A and PMMA for experimental models in excimer laser ablation refractive surgery," Opt. Express **16**, 20955–20967 (2008).

167. S. A. Ashforth, M. C. Simpson, O. Bodley, and R. Oosterbeek,

"Ultrashort pulse laser interactions with cortical bone tissue for applications in orthopaedic surgery," Proc. SPIE **9355**, 935508-1–9 (2015).

168. F. Li, X. Chen, W. Lin, H. Pan, X. Jin, and X. Hua, "Technology Nanosecond laser ablation of Al-Si coating on boron steel," Surf. Coat. Technol. **319**, 129–135 (2017).

169. S. Brattgård, "Microscopical determinations of the thickness of histological sections," J. R. Microsc. Soc. **74**, 113–122 (1954).

170. R. M. Harris, "Light microscopic depth measurements of thick sections," J. Neurosci. Methods **14**, 97–100 (1985).

171. W. Schulz and U. Eppelt, "Basic Concepts of Laser Drilling," in *The Theory of Laser Materials Processing: Heat and Mass Transfer in Modern Technology*, J. Dowden and W. Schulz, eds. (Springer International Publishing, 2009), pp. 129–166.

172. K. C. Yung, H. H. Zhu, and T. M. Yue, "Theoretical and experimental study on the kerf profile of the laser micro-cutting NiTi shape memory alloy using 355 nm Nd:YAG," Smart Mater. Struct. **14**, 337–342 (2005).

173. J. Pocorni, D. Petring, J. Powell, E. Deichsel, and A. F. H. Kaplan, "The Effect of Laser Type and Power on the Efficiency of Industrial Cutting of Mild and Stainless Steels," J. Manuf. Sci. Eng. **138**, 031012 (2015).

174. H. Ki, P. S. Mohanty, and J. Mazumder, "Multiple reflection and its influence on keyhole evolution," J. Laser Appl. **14**, 39–45 (2002).

175. J. H. Cho and S. J. Na, "Implementation of real-time multiple reflection and Fresnel absorption of laser beam in keyhole," J. Phys. D. Appl. Phys. **39**, 5372–5378 (2006).

176. M. Courtois, M. Carin, P. Le Masson, S. Gaied, and M. Balabane, "A complete model of keyhole and melt pool dynamics to analyze instabilities and collapse during laser welding," J. Laser Appl. **26**, 042001 (2014).

177. S. Döring, S. Richter, S. Nolte, and A. Tünnermann, "In situ imaging of hole shape evolution in ultrashort pulse laser drilling," Opt. Express **18**, 20395–20400 (2010).

178. P. Elahi, Ö. Akçaalan, C. Ertek, K. Eken, F. Ö. Ilday, and H. Kalaycoglu, "High-power Yb-based all-fiber laser delivering 300 fs pulses for high-speed ablation-cooled material removal," Opt. Lett. **43**, 535–538 (2018).

179. W. Hu, Y. C. Shin, and G. King, "Modeling of multi-burst mode picosecond laser ablation for improved material removal rate," Appl. Phys. A **98**, 407–415 (2010).

180. S. Amoruso, R. Bruzzese, C. Pagano, and X. Wang, "Features of plasma plume evolution and material removal efficiency during femtosecond laser ablation of nickel in high vacuum," Appl. Phys. A **89**, 1017–1024 (2007).

181.   M. E. Povarnitsyn, T. E. Itina, K. V Khishchenko, and P. R. Levashov, "Suppression of Ablation in Femtosecond Double-Pulse Experiments," Phys. Rev. Lett. **103**, 195002 (2009).

182.   M. E. Povarnitsyn, V. B. Fokin, P. R. Levashov, and T. E. Itina, "Molecular dynamics simulation of subpicosecond double-pulse laser ablation of metals," Phys. Rev. B **92**, 174104 (2015).

183.   J. Schille, L. Schneider, S. Kraft, L. Hartwig, and U. Loeschner, "Experimental study on double-pulse laser ablation of steel upon multiple parallel-polarized ultrashort-pulse irradiations," Appl. Phys. A **122**, 644 (2016).

184.   A. Brenner, M. Zecherle, S. Verpoort, K. Schuster, C. Schnitzler, M. Kogel-Hollacher, M. Reisacher, and B. Nohn, "Efficient production of design textures on large-format 3D mold tools," J. Laser Appl. **32**, 12018 (2020).

185.   B. Lauer, B. Jaeggi, Y. Zhang, and B. Neuenschwander, "Measurement of the Maximum Specific Removal Rate: Unexpected Influence of the Experimental Method and the Spot Size (M701)," Int. Congr. Appl. Lasers Electro-Optics 146–154 (2015).

186.   T. Wuttisarn, V. Tangwarodomnukun, and C. Dumkum, "Laser micro-milling under a thin and flowing water layer: A new concept of liquid-assisted laser machining process," Proc. Inst. Mech. Eng. Part B J. Eng. Manuf. **230**, 376–380 (2015).

187.   B. Neuenschwander, B. Jaeggi, and M. Schmid, "From fs to sub-ns: Dependence of the material removal rate on the pulse duration for metals," Phys. Procedia **41**, 794–801 (2013).

188.   B. Denkena, J. Köhler, and B. Wang, "Manufacturing of functional riblet structures by profile grinding," CIRP J. Manuf. Sci. Technol. **3**, 14–26 (2010).

189.   S. Martin and B. Bhushan, "Modeling and optimization of shark-inspired riblet geometries for low drag applications," J. Colloid Interface Sci. **474**, 206–215 (2016).

190.   R. Grüneberger and W. Hage, "Drag characteristics of longitudinal and transverse riblets at low dimensionless spacings," Exp. Fluids **50**, 363–373 (2011).

191.   D. W. Bechert and W. Hage, "Drag reduction with riblets in nature and engineering," WIT Trans. State Art Sci. Eng. **4**, 457–504 (2006).

192.   Y. W. Ma, Y. H. Lu, J. B. Yi, Y. P. Feng, T. S. Herng, X. Liu, D. Q. Gao, D. S. Xue, J. M. Xue, J. Y. Ouyang, and J. Ding, "Room temperature ferromagnetism in Teflon due to carbon dangling bonds," Nat. Commun. **3**, 727 (2012).

193.   K. Oehlert and J. R. Seume, "Exploratory experiments on machined riblets on compressor blades," Proc. ASME **1**, 25–39 (2007).

194.   F. Torner, G. Stelzer, F. Ströer, and J. Seewig, "Development of a Sensor Prototype and Geometry Based Parameters for the Characterization of Riblets Using Angle-resolved Measurement

Techniques," Procedia CIRP **63**, 8–13 (2017).

195. F. Klocke, B. Feldhaus, and S. Mader, "Development of an incremental rolling process for the production of defined riblet surface structures," Prod. Eng. **1**, 233–237 (2007).

196. L. A. Mähler, T. Willeke, and J. R. Seume, "Numerical Prediction of the Notch Effect of Riblets on Axial Compressor Blades," Proc. GPPS 1–12 (2018).

197. T. Romans and G. Hirt, "Rolling of Drag Reducing Riblet-Surfaces," 51st AIAA/ASME/ASCE/AHS/ASC Struct. Struct. Dyn. Mater. Conf. 1–10 (2010).

198. C. C. Büttner and U. Schulz, "Shark skin inspired riblet coatings for aerodynamically optimized high temperature applications in aeroengines," Adv. Eng. Mater. **13**, 288–295 (2011).

199. F. Afroz, A. Lang, M. Laura, B. Nottebrock, S. Große, W. Schröder, S. Tanzi, P. F. Østergaard, and M. Matteucci, "Shark skin inspired riblet structures as aerodynamically optimized high temperature coatings for blades of aeroengines," Smart Mater. Struct. **20**, 094016 (2011).

200. X. Zheng and Y. Yan, "A Biomimetic Smart Control of Viscous Drag Reduction," Adv. Nat. Sci. **3**, 139–151 (2010).

201. H. Chen, F. Rao, X. Shang, D. Zhang, and I. Hagiwara, "Flow over bio-inspired 3D herringbone wall riblets," Exp. Fluids **55**, 1–7 (2014).

202. R. N. Wenzel, "Resistance of solid surfaces to wetting by water," Ind. Eng. Chem. **28**, 988–994 (1936).

203. A. B. D. Cassie and S. Baxter, "Wettability of porous surfaces," Trans. Faraday Soc. **40**, 546–551 (1944).

204. J. T. Cardoso, A. Garcia-Girón, J. M. Romano, D. Huerta-Murillo, R. Jagdheesh, M. Walker, S. S. Dimov, and J. L. Ocaña, "Influence of ambient conditions on the evolution of wettability properties of an IR-, ns-laser textured aluminium alloy," RSC Adv. **7**, 39617–39627 (2017).

205. Z. Yang, X. Liu, and Y. Tian, "Insights into the wettability transition of nanosecond laser ablated surface under ambient air exposure," J. Colloid Interface Sci. **533**, 268–277 (2019).

206. P. Bizi-bandoki, S. Valette, E. Audouard, and S. Benayoun, "Time dependency of the hydrophilicity and hydrophobicity of metallic alloys subjected to femtosecond laser irradiations," Appl. Surf. Sci. **273**, 399–407 (2013).

207. S. Faas, U. Bielke, R. Weber, and T. Graf, "Scaling the productivity of laser structuring processes using picosecond laser pulses at average powers of up to 420 W to produce superhydrophobic surfaces on stainless steel AISI 316L," Sci. Rep. **9**, 1933 (2019).

208. C. Zhang, S. Li, L. Wang, T. Wu, and S. Peng, "Studies on the decomposition of carbon dioxide into carbon with oxygen-deficient magnetite: I. Preparation, characterization of magnetite, and its activity

of decomposing carbon dioxide," Mater. Chem. Phys. **62**, 44–51 (2000).

209.   S. Razi and F. Ghasemi, "Laser-assisted generation of periodic structures on a steel surface: A method for increasing microhardness," Eur. Phys. J. Plus **133**, 49 (2018).

210.   K. K. S. Lau, J. Bico, K. B. K. Teo, M. Chhowalla, G. A. J. Amaratunga, W. I. Milne, G. H. McKinley, and K. K. Gleason, "Superhydrophobic Carbon Nanotube Forests," Nano Lett. **3**, 1701–1705 (2003).

211.   M. Gonçalves, M. Molina-Sabio, and F. Rodriguez-Reinoso, "Modification of activated carbon hydrophobicity by pyrolysis of propene," J. Anal. Appl. Pyrolysis **89**, 17–21 (2010).

212.   H. Yang, Y. Liu, Z. Guo, B. Lei, J. Zhuang, X. Zhang, Z. Liu, and C. Hu, "Hydrophobic carbon dots with blue dispersed emission and red aggregation-induced emission," Nat. Commun. **10**, 1789 (2019).

SANTRAUKA

Įvadas

Pastaraisiais metais ultratrumpųjų impulsų lazeriai tapo populiariu aukštos kokybės įvairių medžiagų mikroapdirbimo įrankiu mokslo, technologijų ir medicinos srityse. Gamybos įmonėms proceso efektyvumas kartu su gamybos sparta (išeiga) yra esminiai parametrai norint įdiegti lazerinę sistemą į produkcijos liniją. Kad lazerinė technologija būtų konkurencinga pramonėje, didelis tikslumas ir aukšta kokybė, pasiekiama naudojant ultratrumpuosius impulsus, turi derėti su dideliu efektyvumu ir išeiga. Šiuolaikiniai femtosekundiniai lazeriai vis dar yra brangūs prietaisai, nes jų kaina siekia šimtus tūkstančių eurų, ir prieš įdiegiant tokį brangų įrankį gamybos linijoje reikia įvertinti produkcijos gamybos spartą bei įrangos atsiperkamumą. Naudojant lazerinės abliacijos procesą, pavyzdžiui, gręžimą, pjovimą ar frezavimą, proceso našumą galima apibrėžti abliacijos efektyvumu, kaip pašalintos medžiagos tūrį, tenkantį lazerio impulso energijai, o išeigą – pagal abliacijos spartą – pašalintos medžiagos tūrį per laiko vienetą.

Viena iš populiarėjančių mokslo ir technologijos sričių, kurioje naudojamas lazerinis apdirbimas, yra gamtos (bio) įkvėptų (arba biomimetinių) funkcinių paviršių gamyba. Funkciniai paviršiai gamtoje vystėsi ir evoliucionavo milijonus metų, tam, kad padėtų rūšims išlikti, todėl dirbtinai pagaminti ir imituoti šiuos paviršius yra labai svarbus iššūkis. Gamtoje funkcinių paviršių galima rasti ant įvairių gyvūnų, vabzdžių ir augalų. Paprastai tokie paviršiai susideda sudėtingų raštų mikro ar nanoskalėse, kurie suteikia tokias naudingas savybes kaip atsparumas vandeniui, trinties mažinimas, sukibimo didinimas, skaidrumas, struktūrinės spalvos ir kitos. Lazerinis apdirbimas yra puikus įrankis kuriant funkcinius paviršius, nes jis gali būti naudojamas tiek mikro, tiek nanometrinėse skalėse. Lazerinis paviršiaus struktūrinimas mikrometrų skalėje gali būti pasiektas naudojant tiesioginio lazerinio rašymo technologiją, naudojant medžiagos abliaciją. Šios technologijos skiriamąją gebą riboja lazerio šviesos difrakcijos riba. Lazerinis struktūrinimas, viršijantis difrakcinę ribą, nanoskalėje, realizuojamas per savaime susiorganizavusius darinius tokius kaip lazeriu inicijuoti periodiniai paviršiaus dariniai arba raibuliai (angl. *ripples* arba *LIPSS*). Lazerine spinduliuote sukurti nano ir mikrodariniai gali būti panaudoti formuojant funkcinius paviršius su pakeistomis drėkinimo, optinėmis ar tribologinėmis savybėmis.

Ši disertacija buvo skirta ultratrumpųjų impulsų lazerinės abliacijos efektyvumo, medžiagos pašalinimo spartos, apdirbimo kokybės ir panaudojimo mikroapdirbimui bei bioinspiruotų funkcinių paviršių kūrimo tyrimams. Disertaciją sudaro keturi pagrindiniai skyriai: literatūros apžvalga, eksperimentų schemos ir tyrimo metodika, tyrimų rezultatai ir diskusija, pagrindiniai rezultatai ir išvados. Literatūros apžvalgoje trumpai aprašoma ultratrumpųjų lazerio impulsų ir medžiagos sąveikos teorija, efektyvi lazerinė abliacija, impulsų papliūpos, lazeriu inicijuoti periodiniai paviršiaus dariniai ir gamtos įkvėpti funkciniai paviršiai bei jų gamybos technologijos.

Tikslas ir uždaviniai

Šios disertacijos tikslas buvo tirti ultratrumpųjų impulsų lazerinę abliaciją efektyviam energijos panaudojimui preciziškam ir sparčiam aukštos kokybės mikroapdirbimui. Tikslui įgyvendinti buvo išsikelti šie uždaviniai:

1. Išvystyti lazerinės abliacijos optimizavimo metodologiją eksperimentiškai ir teoriškai.
2. Nustatyti optimalias sąlygas didelės galios MHz dažnio papliūpų panaudojimui našiai abliacijai.
3. Ištirti ir palyginti tradicinį apdirbimą pavieniais impulsais su apdirbimu MHz, GHz ir bi papliūpomis gręžiant ir frezuojant.
4. Panaudojant našią lazerinę abliaciją pagaminti gamtos įkvėptus funkcinius paviršius.

Mokslinis naujumas

Šioje disertacijoje buvo pristatytas pluošto dydžio optimizavimo metodas stačiakampės duobutės abliacijai. Taip pat pristatytas, skaitinis lazerinės abliacijos modelis, kuris įskaito abliacijos slenksčio mažėjimą ir abliacijos gylio sotį, kai daugelis impulsų krenta į tašką. Šis modelis nuspėjo pluošto dydžio ir pluošto poslinkio tarp impulsų įtaką abliacijos spartai. Pluošto dydžio optimizavimo metodas buvo panaudotas charakterizuoti ir palyginti gręžimą ir frezavimą MHz, GHz ir bi papliūpomis. Buvo užfiksuoti rekordiniai abliacijos efektyvumai pasiekti ultratrumpaisiais impulsais. Pirmą kartą, pademonstruota abipusių trimačių objektų gamyba panaudojant sluoksnis po sluoksnio apdirbimo techniką. Panaudojant vieno žingsnio femtosekundinio lazerio struktūrinimą plieno paviršiuje buvo sukurtas bioinspiruotas funkcinis paviršius su pilna drėkinimo kontrole. Kiek mums buvo žinoma, mokslinėje literatūroje tokios technologijos, galinčios keisti

vilgumo savybes nuo stipriai hidrofilinio paviršiaus iki superhidrofobinio, iki šiol nebuvo publikuota.

Praktinė vertė

Pristatytas pluošto dydžio optimizavimo metodas stačiakampės duobutės abliacijai yra patikimas įrankis industrinių lazerių įvertinimui ir palyginimui su kitais. Inžineriniu požiūriu pateiktas abliacijos modelis yra esminis teorinis įrankis, padedantis rasti efektyviausią abliacijos tašką. Nuodugnus tyrimas ir surinkta daugybė duomenų apie MHz, GHz ir bi papliūpų ir medžiagos sąveiką padeda teoriškai modeliuoti ir suprasti abliaciją papliūpomis. Funkcinių paviršių (pasipriešinimą mažinančių ir superhidrofobinių) gamyba lazeriu yra tiesiogiai nukreipta į taikymus, kai norima taupyti energiją ir užtikrinti savaiminio nusivalymo savybes.

Ginamieji teiginiai

1. Abliuojant stačiakampę duobutę ultratrumpaisiais lazerio impulsais abliacijos efektyvumas priklauso nuo pluošto žingsnio tarp impulsų ir atstumo tarp skenuojamų linijų. Optimalios sąlygos (pluošto spindulys ir pluošto žingsnis) gali būti nuspėjami skaitiniu modeliu, kuris įtraukia abliacijos slenksčio ir skverbties gylio kritimą didėjant impulsų skaičiui į tašką.

2. Abliacijos efektyvumas frezuojant varį 10 ps trukmės, 120 µJ energijos impulsais gali būti padidintas 50% panaudojant pluošto optimizavimo metodą. Papildomai, 20% padidėjimas gali būti pasiektas jei naudojama 3 impulsų papliupa, su 64,5 MHz vidiniu impulsų pasikartojimo dažniu vietoj apdirbimo pavieniais impulsais.

3. Vario ir nerūdijančio plieno pluošto dydžiu optimizuotas gręžimas papliūpomis, kurių vidinis impulsų pasikartojimo dažnis 4,88 GHz ir impulsų skaičius iki 25, o impulso trukmė 210 fs, nepadidina abliacijos efektyvumo lyginant su pavieniais impulsais. Tačiau panaudojus 64,7 MHz impulsų pasikartojimo dažnio papliūpas ir bipapliūpas (4,88 GHz ir 64,7 MHz) abliacijos našumas gali būti padidintas iki 14%.

4. Ultratrumpieji lazerio impulsai (210 fs – 10 ps) yra universalus įrankis sparčiai aukštos kokybės funkcinių paviršių gamybai panaudojant frezavimą ir tekstūravimą. Lazeriu išfrezuoti griovelių tipo dariniai trintį su oru sumažina iki 6%, o lazeriu tekstūruoto nerūdijančio plieno paviršiaus vilgumas gali būti valdomas nuo stipriai hidrofilinio iki superhidrofobinio.

Eksperimentų įranga ir metodologija

Eksperimentų metu buvo naudojami įvairūs industriniai ultratrumpųjų impulsų lazeriai (1 lentelė). Tipinę optinę schemą sudarė lazerinis šaltinis, veidrodėliai pluošto nuvedimui, pluošto plėstuvas, galvanometrinis skeneris, *XYZ* linijiniai stalai ir cilindrinių bandinių apdirbimui – dvi rotacinės ašys. Kiekvieno eksperimento detalus techninės dalies aprašymas pateikiamas straipsniuose [A1-A7].

1 lentelė. Lazerinio mikroapdirbimo metu naudota įranga.

Lazeris, gamintojas	Atlantic, Ekspla		Atlantic, Ekspla	Carbide, Light Conversion	Pharos, Light Conversion	Pharos, Light Conversion
Impulso trukmė	10 ps		10 ps	210 fs – 10 ps	210 fs	170 fs
Bangos ilgis	1064 nm	355 nm	1064 nm	1030 nm	1030 nm	1026 nm
Vidutinė galia	13 W	4.5 W	40 W	36 W	7,3 W	3,3 W
Pasikartojimo dažnis	100 – 500 kHz		1138 kHz	300 kHz	100 kHz	100 kHz
Veika	Impulsinė		Impulsinė	Papliūpų, 64,5 MHz	Bipapliūpų, 64,7 MHz, 4,9 GHz	Impulsinė
Galvanometrinis skeneris	Scangine 14, Scanlab	Scancube 10, Scanlab	Intelliscan 14, Scanlab	Intelliscan 14, Scanlab	Intelliscan 14, Scanlab	Nenurodyta
F-teta lęšis	+80 mm	+176 mm	+100 mm, +160 mm	+100 mm	+100 mm	+290 mm
Eksperimentas	Naši abliacija	Trintį mažinantys grioveliai	3D mikro-apdribimas, cilindrų apdirbimas	Didelės galios MHz papliūpos	GHz, Bipapliūpos	Vilgumo valdymas
Straipsnis	[A5, A7]	[A6]	[A4, A5]	[A3]	[A1]	[A2]

Šioje disertacijoje buvo sukurta tikslaus abliacijos efektyvumo matavimo metodologija, kuri rėmėsi išabliuotos duobutės tūrio matavimu adatiniu ir optiniu profilometrais.

Rezultatai ir diskusija

Tyrimų rezultatų ir diskusijos skyrius yra paremtas septyniais moksliniais straipsniais užsienyje leidžiamuose periodiniuose mokslo leidiniuose turinčiuose cituojamumo rodiklį (angl. *impact factor*) *Clarivate* duomenų bazėje *Web of Science* ir dviem straipsniais tarptautinių konferencijų darbuose. Pirmojoje tyrimų rezultatų dalyje pateikiami abliacijos efektyvumo optimizavimo eksperimentai, kartu tiriama pluošto skenavimo greičio ir impulsų pasikartojimo dažnio įtaka. Buvo parodyta, kad optimalų energijos

įtėkio tašką didžiausiam lazerio abliacijos efektyvumui galima rasti dvejais metodais. Energijos įtėkio optimizavimas keičiant impulsų energiją parodė, kad lazerio vidutinė galia turi būti apribota, jei norima didžiausio abliacijos efektyvumo. Norint apeiti lazerio galios ribojimą, reikėjo optimizuoti pluošto dydį išlaikant maksimalią galią. Šiuo atveju abliacijos sparta ir efektyvumas buvo optimizuojami vienu metu. Taip pat, nustatyta, kad optimalus energijos įtėkio taškas priklausė nuo pluošto skenavimo greičio ir impulsų pasikartojimo dažnio. Buvo parodyta, kad abliacijos efektyvumo optimizavimas automatiškai pagerina apdirbamo paviršiaus kokybę. Tai labai svarbus rezultatas, nes abi pagrindinės technologinės charakteristikos pagerinamos kartu panaudojant vieną optimizavimo metodiką. Didžiausias abliacijos efektyvumas skenuojant stačiakampius, sudarytus iš lygiagrečių linijų, atskirtų 10 µm atstumu, buvo esant pluošto poslinkiui tarp lazerio impulsų skenavimo kryptimi (pluošto žingsnio) $\Delta x = 0,1$ µm. Eksperimentų metu nustatyta, kad abliacijos efektyvumas priklauso nuo pluošto žingsnio, tačiau teorinis modelis, galintis paaiškinti tokius rezultatus mokslinėje literatūroje neegzistavo. Todėl antroje tyrimų rezultatų dalyje buvo sukurtas pusiau empirinis stačiakampės duobės abliacijos modelis, kuris apjungė ir abliacijos slenksčio kritimo didėjant impulsų skaičiui į vieną tašką ir duobutės gylio įsisotinimo įtaką abliacijos efektyvumui. Eksperimento rezultatai puikiai atitiko naują abliacijos modelį, kuris leido teoriškai numatyti optimalų lazerio pluošto dydį ir optimalų skenuojamo pluošto žingsnį, reikalingus maksimaliam efektyvumui pasiekti. Didelis susidomėjimas medžiagų apdirbimu papliūpomis (lazerio impulsų seka su dideliu impulsų pasikartojimo dažniu) ir galimybė laike padalinti didelės energijos impulsą į keletą mažesnės energijos impulsų nulėmė trečio tyrimų rezultatų dalies atsiradimą, kurioje buvo tiriamas didelės vidutinės optinės galios lazeris, generuojantis papliūpas, sudarytas iš MHz impulsų pasikartojimo dažnio impulsų. Siekiant objektyviai ištirti papliūpų naudą abliacijai, buvo naudojamas pluošto dydžio optimizavimo metodas ir tiriamas abliacijos efektyvumas skirtingam impulsų skaičiui papliūpoje. Vario lazerinės abliacijos papliūpomis tyrimas atskleidė, kad, geriausiu atveju, abliacijos efektyvumas gali būti pagerintas 20% naudojant trijų impulsų papliūpas, lyginant su apdirbimu pavieniais impulsais. Visi kiti impulsų skaičiai per papliūpą parodė mažesnį abliacijos efektyvumą. Tyrimų publikavimo metu buvo pasiektas lazerinio frezavimo ultratrumpaisiais impulsais variui rekordas – 4,8 µm³/µJ. Kitas papliūpų pranašumas lyginant su pavieniais impulsais buvo mažesnis išabliuotų duobučių dugno šiurkštumas, kuris buvo keletą kartų mažesnis. Taip pat, buvo ištirta lazerio impulso trukmės įtaka mikroapdirbimui – nustatyta, kad impulso trukmės intervale nuo 210 fs iki

10 ps abliacijos efektyvumas padidėjo 32% ilgesniems impulsams. Apibendrinant galima teigti, kad MHz papliūpų panaudojimas vario mikroapdirbimui lazeriu yra naudingas tik tada, kai naudojamos trijų impulsų papliūpos – padidėja abliacijos efektyvumas ir kokybė, lyginant su apdirbimu pavieniais impulsais. Be to, apdirbimo lazerine spinduliuote skiriamoji geba padidinama naudojant papliūpas dėl mažesnio pluošto dydžio, reikalingo optimaliam energijos įtėkiui pasiekti. Didelio impulsų pasikartojimo dažnio papliūpos, siekiančios GHz, susilaukė didelio dėmesio dėl galimo didelio medžiagos pašalinimo efektyvumo. Didelis efektyvumas atsiranda dėl šilumos, sugeneruotos pirmo impulso pašalinimo, bei jos išnaudojimo medžiagos pašalinimui antru impulsu sekoje, greičiu, didesniu nei šilumos difuzija gilyn į bandinį. Ketvirtojoje tyrimų rezultatų dalyje buvo panaudotas naujausias femtosekundinis lazeris iš įmonės „Light Conversion", generuojantis MHz ir GHz papliūpas vienu metu (bipapliūpas). Pirmą kartą buvo pademonstruotas bipapliūpų panaudojimas efektyviam vario ir plieno gręžimui ir frezavimui ištirti atliekant pluošto dydžio optimizavimą. Vario frezavimo ir gręžimo MHz papliūpomis atveju abliacijos efektyvumas labai priklausė nuo to, ar impulsų skaičiaus papliūpoje buvo lyginis ar nelyginis. Plieno frezavimo atveju tokia priklausomybė abliacijos efektyvumui nenustatyta. Ištirta, kad apdirbimas GHz papliūpomis yra labai neefektyvus tiek variui, tiek plienui ir frezuojant ir gręžiant lyginant su apdirbimu pavieniais impulsais. Vario ir plieno frezavimas bipapliūpomis nepagerino abliacijos efektyvumo lyginant su frezavimu pavieniais impulsais, tačiau vario gręžimo efektyvumas bipapliūpomis buvo didesnis nei gręžimo pavieniais impulsais. Išmatuotos trys aukšto abliacijos efektyvumo vertės panaudojant ultratrumpųjų impulsų lazerį, kurio bangos ilgis buvo apie ~1 µm: 8,8 $\mu m^3/\mu J$ vario gręžimui, 5,6 $\mu m^3/\mu J$ vario frezavimui ir 6,9 $\mu m^3/\mu J$ plieno frezavimui. Našiam lazeriniam frezavimui bei didžiausiai apdirbimo kokybei optimizuota lazerinė spinduliuotė buvo panaudota trimačių objektų ir bioinspiruotų funkcinių paviršių kūrimui. Penktojoje tyrimų rezultatų dalyje pateikiami trimačio subtraktyvaus mikroapdirbimo pavyzdžiai, kuomet norima trimatė forma gaunama frezuojant medžiagą sluoksnis po sluoksnio panaudojant pavienius impulsus ir papliūpas. Vario paviršiuje naudojant lazerinę spinduliuotę buvo pagaminti gamtos įkvėpti paviršiai: žuvies žvynai ir ryklio odos raštas. Tai pat, buvo pademonstruota trimačio abipusio objekto gamyba, kuomet bandinys buvo apdirbamas sluoksnis po sluoksnio iš priekinės pusės, tuomet bandinys apverčiamas ir toliau apdirbimas tęsiamas iš galinės pusės. Buvo pademonstruota galimybė imituoti gamtos įkvėptus funkcinius paviršius dideliu apdribimo greičiu. Šeštoje tyrimų rezultatų dalyje pateikiami rezultatai apie pademonstruotą galimybę lazeriu apdirbti sudėtingos formos cilindrinius

bandinius panaudojant penkių valdomų koordinačių ašių lazerinio apdribimo stakles. Lazerinis mikroapdirbimas buvo optimizuotas abliacijos efektyvumo ir santykinio paviršiaus šiurkštumo atžvilgiu, kurių energijos įtėkių optimalios vertės sutapo. Optimizavimas buvo atliktas lazerinio tekinimo principu – lazerio pluoštas judėjo skersai besisukančio aplink savo ašį bandinio, taip formuojant kontroliuojamo pločio skersines įpjovas. Ištirta abliacijos efektyvumo priklausomybė nuo impulsų pasikartojimo dažnio parodė, kad esant energijos įtėkiams, didesniems už tam tikrą kritinę vertę, abliacijos sparta krinta, o šis kritimas pasireiškia anksčiau esant didesniems impulsų pasikartojimo dažniams. Toks abliacijos spartos kritimas buvo paaiškintas lazerinės spinduliuotės ekranavimu abliacijos produktais ir susiformavusia plazma. Optimalūs lazerinio apdirbimo parametrai buvo panaudoti suformuojant išilginius griovelius ant cilindro formos bandinio, kurie priminė supaprastintą ryklio odos raštą, pasižymintį trinties mažinimo savybėmis. Septintoje tyrimų rezultatų dalyje aprašytas lazeriu suformuotų ryklio odos paviršių trinties su oru charakterizavimas. Tam buvo sukonstruotas trinties tarp oro srauto ir lazerine spinduliuote tekstūruoto bandinio paviršiaus matavimo stendas ir pasinaudojus juo išmatuotas ryklio odos rašto trinties mažinimo efektyvumas. Teflono paviršiuje pikosekundinio lazerio spinduliuote buvo suformuotas supaprastintas ryklio odos raštas sudarytas iš įvairaus periodo lygiagrečių griovelių. Griovelių gylis buvo lygus pusei periodo tam, kad būtų pasiektas didžiausias teoriškai galimas trinties sumažėjimas. Eksperimentiškai išmatuotas maksimalus trinties sumažėjimas siekė 6% lyginant su netekstūruotu, plokščiu bandiniu. Siekiant sukurti funkcinį plieno paviršių su pakeistomis vilgumo savybėmis, buvo išnaudoti po lazerinės ekspozicijos savaime susiorganizuojantys dariniai – raibuliai ir nanospygliai. Šie eksperimentai aprašyti aštuntoje tyrimų rezultatų dalyje. Kontroliuojant suminį energijos įtėkį nuo 4 J/cm^2 iki 2,6 kJ/cm^2, nerūdijančio plieno paviršius buvo pakeistas nuo stipriai hidrofilinio iki superhidrofobinio su kontaktiniais kampais tarp vandens lašo ir bandinio paviršiaus nuo 4° iki 150°, atitinkamai. Pradinis stipriai hidrofilinis paviršius buvo palaipsniui pakeistas į superhidrofobinį dėl lazeriu indukuotų raibulių ir esant dideliam suminiam energijos įtėkiui – dėl nanospyglių. Vilgumo būsenos kitimas priklausomai nuo suminio energijos įtėkio prasidėjo kartu su raibulių formavimusi, taip įrodant, kad plieno tekstūravimas lazeriu inicijuotais raibuliais buvo atsakingas dėl paviršiaus drėkinimo savybių. Tačiau paviršiaus morfologija buvo ne vienintelė priežastis, dėl kurios pakito plieno vilgumas. Ištyrus paviršiaus cheminę sudėtį Rentgeno spindulių energijos dispersijos spektrometru buvo nustatyta, kad kontaktinis kampas priklausė nuo deguonies santykio su anglimi (O/C), kai tuo tarpu, O/C santykis stipriai teigiamai

koreliavo su suminiu energijos įtėkiu. Buvo pristatytas galimas paviršiaus chemijos kitimo mechanizmas po lazerinio apdirbimo dėl CO_2 molekulių, esančių ore, skilimo ir reakcijos su nestechiometriniu deguonimi nuskurdinto aktyvaus magnetito $Fe_3O_{4-\delta}$.

Pagrindiniai rezultatai ir išvados

1. Lazerine spinduliuote išabliuoto paviršiaus kokybė buvo geriausia panaudojus optimalius apdirbimo parametrus, nustatytus didžiausiam efektyvumui.
2. Pristatytas teorinis stačiakampės duobutės lazerinės abliacijos modelis, apimantis abliacijos slenksčio mažėjimą ir abliacijos gylio įsisotinimą didėjant impulsų skaičiui į tašką.
3. Panaudojus pluošto dydžio optimizavimo metodą vario frezavimo efektyvumas ultratrumpaisiais impulsais (impulso energija 120 µJ) buvo padidintas 50%. Lazerinės abliacijos papliūpomis su vidiniu dažniu 64,5 MHz tyrimas atskleidė, kad geriausiu atveju, abliacijos efektyvumas gali būti pagerintas 20% naudojant trijų impulsų papliūpas, lyginant su apdirbimu pavieniais impulsais.
4. Frezuojant ir grežiant varį 64,7 MHz papliūpomis abliacijos efektyvumas stipriai priklausė nuo nelyginių ir lyginių impulsų skaičiaus papliūpoje.
5. Vario grežimas 4,88 GHz papliūpomis, kurias sudaro iki 25 impulsų, nepagerino abliacijos efektyvumo lyginant su pavieniais impulsais. Tačiau, naudojant 64,7 MHz arba bipapliūpas grežimo efektyvumas buvo pagerintas iki 14%.
6. Buvo pademonstruota galimybė dideliu apdirbimo greičiu imituoti gamtos įkvėptus funkcinius paviršius naudojant įprastinį ir trimatį sluoksnis po sluoksnio lazerinį apdirbimą.
7. Supaprastinto ryklio odos rašto – griovelių gamyba lazerine spinduliuote buvo pademonstruota ant plokščio ir cilindro formos paviršių.
8. Grioveliais tekstūruotas funkcinis paviršius 6% sumažino oro trintį lyginant su plokščiu, netekstūruotu bandiniu.
9. Pradinis stipriai hidrofilinis paviršius buvo palaipsniui pakeistas į superhidrofobinį dėl lazeriu indukuotų raibulių ir esant dideliam suminiam energijos įtėkiui – dėl nanospyglių.
10. Apibendrinant disertaciją, galima daryti pagrindinę išvadą, kad doktorantūros studijų metu išvystyta našaus lazerinio frezavimo technologija su optimizuota ultratrumpųjų impulsų lazerine spinduliuote maksimaliam medžiagos pašalinimui bei minimaliam paviršiaus

šiurkštumui yra puikus įrankis sparčiam medžiagų mikroapdirbimui ir trimačių gamtos įkvėptų funkcinių paviršių kūrimui.

PADĖKA

Nuoširdžiai dėkoju savo doktorantūros vadovui jaunajam akademikui dr. Mindaugui Gedvilui, kurio pasirinktas vadovavimo stilius puikiai suveikė ir privedė prie įspūdingų rezultatų. Ačiū jam už tai, kad visada skatino siekti daugiau ir aukščiau nei man pačiam atrodė, kad reikia. Ačiū už tai, kad nei vienas mokslinis rezultatas nebuvo sumenkintas, o atvirkščiai – išaukštintas.

Dėkoju Lazerinio mikroapdirbimo technologijų vadovui dr. Pauliui Gečiui už tai, kad pakvietė būti mokslininku ir už tai, kad visada sutinka padėti. Dėkoju Lazerinių technologijų skyriaus vadovui dr. Gediminui Račiukaičiui už rūpinimąsi ir studentų palaikymą.

Ačiū kolegoms už gerą laiką: Juozui, Gretai, Simui, Edgarui, Evaldui, Romualdui, Laimiui, Miglei, Mantui, Vytautui. Ačiū studentėms Saulei ir Ugnei už teisingus pasirinkimus.

I am grateful to colleagues from FORTH in Crete for accepting us in their lab and willingness to collaborate: Dr. Emmanuel Stratakis, Dr. Evangelos Skoulas, Alexandros Mimidis, Antonis Papadopoulos, Andreas Lemonis.

Taip pat esu dėkingas savo tėvams ir sesei už palaikymą ir pagalbą per visą mokslo laikotarpį. Didžiausias AČIŪ žmonai Gretai už begalinę meilę.

CURRICULUM VITAE

Andrius Žemaitis born in 1991-12-22, Penevėžys, Lithuania.

e-mail: andrius.zemaitis@ftmc.lt

Education

2017 – 2021 PhD studies in Materials Engineering at the Center for Physical Sciences and Technology and Vilnius University.

2015 – 2017 Master's Degree in Materials Technology (Magna Cum Laude diploma), Vilnius University, Faculty of Physics, study programme Laser Technology.

2016 half a year Eramus+ studies at the University of Padova.

2015 Bachelor's Degree in Physics, Vilnius University, Faculty of Physics, study programme Modern Technologies of Physics and Management.

2014 half a year Erasmus studies at Czech Technical University in Prague.

2007 – 2011 Panevėžys Juozas Balčikonis gymnasium, High school education.

Work experience

Since 2018 junior researcher, 2015 – 2017 engineer, 2014 – 2015 technician, 2014 summer intern at the Laser Microfabrication Laboratory, Department of Laser Technologies, Center for Physical Sciences and Technology (LTS-FTMC).

2019 and 2020 (total 4 months) Internship in Institute of Electronic Structure and Laser, Foundation for Research and Technology (IESL-FORTH), Crete, Greece. Dr. E. Stratakis' Ultrafast Laser Micro and Nano Processing Laboratory.

2016 March – July Laser FEMTO laboratory in Department of Information Engineering, University of Padova, Italy.

PUBLICATIONS

1. A. Žemaitis, M. Gaidys, P. Gečys, M. Barkauskas, M. Gedvilas, "Femtosecond laser ablation by bibursts in the MHz and GHz pulse repetition rates," Opt. Express 29, 7641–7653 (2021). DOI: 10.1364/OE.417883

2. A. Žemaitis, A. Mimidis, A. Papadopoulos, P. Gečys, G. Račiukaitis, E. Stratakis, M. Gedvilas, "Controlling the wettability of stainless steel from highly-hydrophilic to super-hydrophobic by femtosecond laser-induced ripples and nanospikes," RSC Adv. 10, 37956-37961 (2020). DOI: 10.1039/D0RA05665K

3. A. Žemaitis, P. Gečys, M. Barkauskas, G. Račiukaitis, M. Gedvilas, "Highly-efficient laser ablation of copper by bursts of ultrashort tuneable (fs-ps) pulses,", Sci. Rep. 9, 12280 (2019). DOI: 10.1038/s41598-019-48779-w

4. M. Gaidys, A. Žemaitis, P. Gečys, M. Gedvilas, "Efficient picosecond laser ablation of copper cylinders," Appl. Sur. Sci. 483, 962-966 (2019). DOI: 10.1016/j.apsusc.2019.04.002

5. A. Žemaitis, M. Gaidys, P. Gečys, G. Račiukaitis, M. Gedvilas, "Rapid high-quality 3D micro-machining by optimised efficient ultrashort laser ablation," Opt. Lasers Eng. 114, 83-89 (2019). DOI: 10.1016/j.optlaseng.2018.11.001

6. A. Žemaitis, J. Mikšys, M. Gaidys, P. Gečys, M. Gedvilas, "High-efficiency laser fabrication of drag reducing riblet surfaces on pre-heated Teflon," Mater. Res. Express 6, 065309 (2019). DOI: 10.1088/2053-1591/ab0b12

7. A. Žemaitis, M. Gaidys, M. Brikas, P. Gečys, G. Račiukaitis, M. Gedvilas, "Advanced laser scanning for highly-efficient ablation and ultrafast surface structuring: experiment and model," Sci. Rep. 8, 17376 (2018). DOI: 10.1038/s41598-018-35604-z

8. A. Žemaitis, P. Gečys, G. Račiukaitis, and M. Gedvilas, "Efficient ablation by ultra-short pulse lasers," Procedia CIRP 94, 962–965 (2020). DOI: 10.1016/j.procir.2020.09.083

9. A. Žemaitis, M. Gaidys, J. Mikšys, P. Gečys, M. Gedvilas, "Functional surface formation by efficient laser ablation using single-pulse and burst-modes," Proc. SPIE 11673, 116730S (2021). DOI: 10.1117/12.2574840

NOTES

NOTES